

University of Illinois at Urbana-Champaign



Air Conditioning and Refrigeration Center A National Science Foundation/University Cooperative Research Center

Improving the Accuracy and Scope of Control-Oriented Vapor Compression Cycle System Models

B. D. Eldredge and A. G. Alleyne

ACRC TR-246

August 2006

For additional information:

Air Conditioning and Refrigeration Center
University of Illinois
Mechanical & Industrial Engineering Dept.
1206 West Green Street
Urbana, IL 61801

(217) 333-3115

*Prepared as part of ACRC Project #175
Dynamic Grey Box Modeling for Vapor Compression Cycle Systems
A. G. Alleyne, Principal Investigator*

The Air Conditioning and Refrigeration Center was founded in 1988 with a grant from the estate of Richard W. Kritzer, the founder of Peerless of America Inc. A State of Illinois Technology Challenge Grant helped build the laboratory facilities. The ACRC receives continuing support from the Richard W. Kritzer Endowment and the National Science Foundation. The following organizations have also become sponsors of the Center.

Arçelik A. S.
Behr GmbH and Co.
Carrier Corporation
Cerro Flow Products, Inc.
Copeland Corporation
Daikin Industries, Ltd.
Danfoss A/S
Delphi Thermal and Interior
Embraco S. A.
General Motors Corporation
Hill PHOENIX
Honeywell, Inc.
Hydro Aluminum Precision Tubing
Ingersoll-Rand/Climate Control
Lennox International, Inc.
LG Electronics, Inc.
Manitowoc Ice, Inc.
Matsushita Electric Industrial Co., Ltd.
Modine Manufacturing Co.
Novelis Global Technology Centre
Parker Hannifin Corporation
Peerless of America, Inc.
Samsung Electronics Co., Ltd.
Sanden Corporation
Sanyo Electric Co., Ltd.
Tecumseh Products Company
Trane
Visteon Automotive Systems
Wieland-Werke, AG

For additional information:

*Air Conditioning & Refrigeration Center
Mechanical & Industrial Engineering Dept.
University of Illinois
1206 West Green Street
Urbana, IL 61801*

217 333 3115

Abstract

The benefits of applying advanced control techniques to vapor compression cycle systems are well known. The main advantages are improved performance and efficiency, the achievement of which brings both economic and environmental gains. One of the most significant hurdles to the practical application of advanced control techniques is the development of a dynamic system level model that is both accurate and mathematically tractable. Previous efforts in control-oriented modeling have produced a class of heat exchanger models known as moving-boundary models. When combined with mass flow device models, these moving-boundary models provide an excellent framework for both dynamic analysis and control design. This thesis contains the results of research carried out to increase both the accuracy and scope of these system level models.

The improvements to the existing vapor compression cycle models are carried out through the application of various modeling techniques, some static and some dynamic, some data-based and some physics-based. Semi-empirical static modeling techniques are used to increase the accuracy of both heat exchangers and mass flow devices over a wide range of operating conditions. Dynamic modeling techniques are used both to derive new component models that are essential to the simulation of very common vapor compression cycle systems and to improve the accuracy of the existing compressor model. A new heat exchanger model that accounts for the effects of moisture in the air is presented. All of these model improvements and additions are unified to create a simple but accurate system level model with a wide range of application. Extensive model validation results are presented, providing both qualitative and quantitative evaluation of the new models and model improvements.

Table of Contents

	Page
Abstract.....	iii
List of Figures	vii
List of Tables	x
List of Abbreviations.....	xi
Chapter 1. Introduction.....	1
1.1 Motivation.....	1
1.1.1 Vapor Compression Cycle Systems	1
1.1.2 Efficiency	2
1.1.3 Advantages of Feedback Control	2
1.1.4 Model-based Control	2
1.1.5 Industry Need	3
1.2 Objectives.....	3
1.3 Literature Review.....	3
1.3.1 Finite Difference Models.....	3
1.3.2 Moving-boundary Models	3
1.3.3 Model Validation.....	4
1.4 Organization.....	4
Chapter 2. Previous VCC Modeling	6
2.1 Moving-boundary Heat Exchanger Modeling	6
2.2 Static Valve Modeling.....	8
2.3 Static Compressor Modeling.....	8
2.4 Modeling Challenges.....	9
2.4.1 Accurate Model Parameters	9
2.4.2 Atmospheric Conditions.....	10
2.4.3 Expanding Operating Conditions	10
2.4.4 Dynamic Compressor Shell Model.....	10
2.4.5 Large Transient Simulation	10
Chapter 3. Semi-empirical Models	11
3.1 External Heat Transfer Coefficients	11
3.1.1 Empirical Heat Transfer Model.....	11
3.1.2 Sources of Empirical Heat Transfer Data	11
3.1.3 Implementation in Thermosys	13
3.2 Performance Mapping.....	15
3.2.1 Valves.....	17
3.2.2 Compressor.....	24
3.2.3 Implementation in Thermosys	26
Chapter 4. Atmospheric Conditions Modeling	30
4.1 Air Temperature Condensation Method.....	30

4.1.1 Modified Energy Balances	31
4.1.2 Heat Transfer Rates	34
4.1.3 Implementation in Thermosys	34
4.2 Wall Temperature Condensation Method	35
4.2.1 Individual Region Mass and Energy Balances	36
4.2.2 Outlet Humidity Calculations	37
4.2.3 Mixing of Region Outputs	38
4.2.4 Implementation in Thermosys	39
Chapter 5. Dynamic Modeling	40
5.1 Motivation	40
5.1.1 Heat exchangers with Receivers/Accumulators	40
5.1.2 Compressor Shell Capacitance	40
5.1.3 Dynamic Mass Flow Correction	40
5.1.4 Compressor Cycling Simulation	40
5.2 Heat Exchangers with Receivers/Accumulators	41
5.2.1 Challenge of Receiver/Accumulator Modeling	41
5.2.2 Receiver Model	41
5.2.3 Accumulator Model	42
5.2.4 Nonlinear Condenser with Receiver	43
5.2.5 Nonlinear Evaporator with Accumulator	45
5.2.6 Pseudo-Quality and Mean Void Fraction	46
5.3 Compressor Shell Thermal Capacitance Dynamic	48
5.3.1 Implementation in Thermosys	49
5.4 Identified Compressor Mass Flow Model	51
5.4.1 Compressor Mass Flow Dynamics Isolation	51
5.4.2 Identification of Isolated Dynamics	52
5.5 Compressor Cycling Dynamics	52
5.5.1 Literature Review	52
5.5.2 Current Thermosys Model Cycling Capabilities	54
5.6 Future Work	59
5.6.1 Cycling Simulation	59
5.6.2 Start-up Simulation	59
5.6.3 Improved Compressor Mass Flow Prediction	60
Chapter 6. Experimental System	61
6.1 General Description	61
6.2 Sensors	63
6.2.1 Temperature, Pressure, Mass Flow, and Power Measurement	64
6.2.2 Humidity Measurement	65
6.3 Actuators	65
6.3.1 Compressor, Fans, and Valves	65
6.3.2 Humidifier	66
6.4 Data Acquisition	67

6.5 Components	67
6.5.1 Heat Exchangers	67
6.5.2 Auxiliary Components	67
6.6 Physical Parameters	68
Chapter 7. Model Validation	69
7.1 Single-Step Model Validation Scenario	69
7.1.1 System Inputs	69
7.1.2 System Output	71
7.1.3 Quantified Modeling Improvements	76
7.2 Drive Cycle Model Validation Scenario	77
7.2.1 System Inputs	78
7.2.2 System Outputs	79
7.3 Atmospheric Conditions Model Validation Scenario	81
7.3.1 System Inputs	82
7.3.2 System Outputs	83
7.3.3 Simulation Analysis	85
Chapter 8. Conclusions and Future Work	89
8.1 Summary of Research Contributions	89
8.1.1 Model Developments	89
8.1.2 Model Validation	89
8.2 Future Work	90
8.2.1 Model Development	90
8.2.2 Model Validation	90
8.2.3 Model Applications	90
List of References	91
Appendix A. Sample Code	94
H.1 Condenser j Factor Correlation	94
H.2 Evaporator j Factor Correlation	95
H.3 EEV Performance Map	96
H.4 AEV Performance Map	98
H.5 TEV Performance Map	99
H.6 Capillary Tube Performance Map	103
H.7 Volumetric Efficiency Performance Map	105
H.8 Adiabatic Efficiency Performance Map	106
Appendix B. Operating Conditions	109

List of Figures

	Page
Figure 1.1 Components of the basic vapor compression cycle	1
Figure 2.1 Evaporator fluid regions	7
Figure 3.1 The experimentally obtained j factor plot for surface CF-8.72 from [25]	12
Figure 3.2 Experimental system condenser j factor from correlation	12
Figure 3.3 Experimental system evaporator j factor from correlation	12
Figure 3.4 Example calculation of heat exchanger flow length	13
Figure 3.5 Plane of maximum flow constriction used in calculation of the minimum free flow area	14
Figure 3.6 Block diagram of heat transfer coefficient calculation from j factor data	15
Figure 3.7 Compressor speed and valve opening settings	16
Figure 3.8 Range of operating conditions covered by performance maps	16
Figure 3.9 Comparison of 2-input and 3-input EEV models with experimental data	18
Figure 3.10 Flow coefficient map for an EEV with black points representing experimental data	19
Figure 3.11 Schematic of an AEV [1]	19
Figure 3.12 Flow coefficient performance map and data points for an AEV	20
Figure 3.13 Schematic of a TEV and example values for superheat regulation [2]	21
Figure 3.14 TEV discharge coefficient performance map and generating data	22
Figure 3.15 TEV area map	23
Figure 3.16 Capillary tube flow coefficient data points and best fit performance map	24
Figure 3.17 A two input performance map of volumetric efficiency	25
Figure 3.18 A two-input adiabatic efficiency map with experimental data	26
Figure 3.19 2-D lookup table block and Block Parameters interface	27
Figure 3.20 3-D lookup table block and Block Parameters interface	28
Figure 3.21 Performance map portion of the 2-input EEV component GUI showing data structure field names	29
Figure 4.1 Water saturation pressure as a function of saturation temperature	30
Figure 4.2 Water saturated liquid enthalpy as a function of temperature	30
Figure 4.3 Control volume for humid air mass and energy balances under non-condensing conditions	31
Figure 4.4 Control volume for humid air mass and energy balances under condensing conditions	33
Figure 4.5 Data for a condensing conditions test with the air temperature well above the dew point temperature	35
Figure 4.6 Divided air-side control volumes	36
Figure 5.1 Two possible steady-state condenser with receiver operating conditions	41
Figure 5.2 A possible transient condenser with receiver operating condition	41
Figure 5.3 Control volume for receiver model	42
Figure 5.4 Control volume for accumulator model	42
Figure 5.5 Mean void fraction for two-phase flows operating at 900 kPa (condenser) and 320 kPa (evaporator) as a function of the outlet quality	48
Figure 5.6 Compressor shell and refrigerant outlet temperature data for system shutdown from 1600 RPM	49
Figure 5.7 Block diagram of Equation 5.23	49
Figure 5.8 Compressor outlet temperature data (blue) and small time constant model output (green)	50

Figure 5.9 Compressor outlet temperature model output for various time constants	50
Figure 5.10 Compressor mass flow dynamics isolation procedure.....	51
Figure 5.11 Receiver mass inventory showing numerical instability	54
Figure 5.12 Pressures.....	55
Figure 5.13 Condenser fluid region lengths.....	55
Figure 5.14 Evaporator fluid region lengths with the superheat length vanishing.....	55
Figure 5.15 Receiver mass inventory	55
Figure 5.16 Evaporator superheat.....	56
Figure 5.17 System pressure data	56
Figure 5.18 System evaporator superheat data	57
Figure 5.19 System pressures	57
Figure 5.20 Condenser lengths	57
Figure 5.21 Evaporator lengths.....	58
Figure 5.22 Evaporator superheat.....	58
Figure 5.23 System pressure data	58
Figure 5.24 System evaporator superheat data	59
Figure 6.1 Experimental system schematic	62
Figure 6.2 Photograph of the relative humidity sensor at the evaporator inlet	65
Figure 6.3 Humidifier and tubing bringing moist air output to the evaporator inlet.....	66
Figure 7.1 Valve input signal.....	70
Figure 7.2 Compressor input signal.....	70
Figure 7.3 Condenser air mass flow rate input signal.....	70
Figure 7.4 Evaporator mass flow rate input signal	70
Figure 7.5 Condenser with receiver pressure.....	72
Figure 7.6 Condenser with receiver outlet air temperature.....	72
Figure 7.7 Condenser with receiver refrigerant outlet temperature	72
Figure 7.8 Evaporator pressure.....	73
Figure 7.9 Evaporator superheat.....	73
Figure 7.10 Static volumetric efficiency map (surface) and volumetric efficiency generated from mass flow correction (line)	74
Figure 7.11 Condenser pressure	75
Figure 7.12 Condenser air outlet temperature.....	75
Figure 7.13 Evaporator pressure.....	75
Figure 7.14 Evaporator air outlet temperature	76
Figure 7.15 Evaporator superheat.....	76
Figure 7.16 Compressor speed	78
Figure 7.17 Condenser air mass flow rate	78
Figure 7.18 Valve opening	79
Figure 7.19 Valve mass flow data and compressor mass flow models.....	79
Figure 7.20 Condenser pressure data and models.....	79

Figure 7.21 Condenser outlet air temperature data and models.....	80
Figure 7.22 Evaporator pressure data and models.....	80
Figure 7.23 Evaporator superheat data and models.....	80
Figure 7.24 Evaporator outlet air temperature data and models.....	80
Figure 7.25 Components used in humidity model validation.....	82
Figure 7.26 Inlet relative humidity data.....	82
Figure 7.27 Photograph on the inlet and outlet evaporator pipes with condensation on the inlet (lower) pipe.....	83
Figure 7.28 Outlet relative humidity data and model.....	83
Figure 7.29 Condensate mass flow rate model.....	84
Figure 7.30 Evaporator outlet air temperature and model.....	84
Figure 7.31 Accumulated condensation measurements and model prediction.....	85
Figure 7.32 Inlet relative humidity.....	86
Figure 7.33 Dew point temperature and model wall temperatures.....	86
Figure 7.34 Outlet relative humidity model.....	86
Figure 7.35 Condensate mass flow rate model.....	87
Figure 7.36 Outlet evaporator air temperature model.....	87
Figure 7.37 Evaporator pressure model.....	88
Figure A.1 Diagram of TEV geometry.....	103

List of Tables

	Page
Table 3.1 Fields in the HX data structure	15
Table 5.1 Entries of $Z_c(x_c, u_c)$ for the condenser with receiver model	44
Table 5.2 Entries of $Z_e(x_e, u_e)$ for the evaporator with accumulator model	45
Table 6.1 Valve acronyms and descriptions	62
Table 6.2 Component name, manufacturer, model, and URL	63
Table 6.3 Sensor designations and locations	64
Table 6.4 Component physical parameters used for model validation simulations	68
Table 7.1 Summary of inputs used in the single-step validation scenario	69
Table 7.2 Cross-sectional areas based on total high-side and low-side volumes	71
Table 7.3 Comparison of model fit values	74
Table 7.4 RMS error and RMS error reduction in the condenser pressure	76
Table 7.5 Error metric scaling factors	77
Table 7.6 Error metric and error metric improvement	77
Table 7.7 Table of inputs for the drive cycle validation scenario	78
Table B.1 Model validation scenario operating conditions	109

List of Abbreviations

AEV – automatic expansion valve
EES – Engineering Equation Solver
EEV – electronic expansion valve
HVAC – heating, ventilation, and air-conditioning
ILC – iterative learning control
MIMO – multiple-input multiple-output
NREL – National Renewable Energy Laboratory
ODE – ordinary differential equation
PDE – partial differential equation
RMS – root mean square
RPM – revolutions per minute
SISO – single-input single-output
TEV – thermostatic expansion valve
VCC – vapor compression cycle
VFD – variable frequency drive

List of Symbols

<u>Variable</u>	<u>Explanation</u>
α	Heat Transfer Coefficient
η	Efficiency
γ	Void Fraction
$\bar{\gamma}$	Mean Void Fraction
\dot{m}	Mass Flow Rate
ρ	Density
$\hat{\bar{\gamma}}$	Pseudo Mean Void Fraction
ϕ	Relative Humidity
A	Area
C	Coefficient
C_p	Specific Heat
e	Error
G	Maximum Mass Velocity, Transfer Function
h	Specific Enthalpy
j	Colburn j factor
L	Length
m	Mass
P	Pressure
p	Perimeter
Pr	Prandtl Number
\dot{Q}	Heat Transfer Rate
Re	Reynold's Number
S	Slip Ratio
s	Specific Entropy
sh	Superheat

St	Stanton Number
T	Temperature
t	Time
u	Specific Internal Energy, Controllable Inputs
UA	Lumped Heat Transfer Coefficient
V	Volume, Volts
x	Quality, Dynamic States
y	Outputs
z	Spatial Coordinate
Z	Descriptor Form Matrix
Δ	Change
μ	Viscosity
ω	Angular Velocity, Absolute Humidity

<u>Subscript</u>	<u>Explanation</u>
1,2,3	1 st , 2 nd , 3 rd Region
acc	Accumulator
air, a	Air, Adiabatic
amb	Ambient
ave	Average
bulb	TEV Sensing Bulb
c	Condenser
cs	Cross-Sectional
d	Diameter
dp	Dew Point
e	Evaporator
f	Liquid
g	Vapor
h	Hydraulic
i	Inner
in	In
int	Fluid Region Interface
k	Compressor
o	Outer
out	Out
r	Refrigerant
rec	Receiver
sat	Saturation
T	Total
total	Total
v	Valve, Vapor
vol	Volumetric
w	Wall, Water

Chapter 1. Introduction

1.1 Motivation

Vapor compression cycle (VCC) systems are now an essential part of life, providing critical temperature control through air-conditioning and refrigeration machines. These complex thermo-fluid systems have increased in efficiency as they have increased in usage [15]. Great efforts have been expended in optimizing the design of individual VCC components. Most of this component-based research has focused on steady-state performance. This work, in contrast, examines the transient behavior and performance of vapor compression cycles at the system level. An understanding of the system dynamic behavior opens the door for the application of advanced feedback control techniques. Feedback control promises further improvements in efficiency, resulting in both economic and environmental benefits.

1.1.1 Vapor Compression Cycle Systems

A basic VCC system is composed of four primary components: an evaporator, a compressor, a condenser, and an expansion device, as shown in Figure 1.1. Optional but common components include receivers and accumulators. There are two basic types of vapor compression cycles. In the subcritical cycle, the refrigerant stays below its critical point, while in the transcritical cycle, the refrigerant goes above its critical point. This work will focus on the subcritical cycle, which operates as follows. Starting at the compressor inlet, superheated or saturated vapor refrigerant enters the compressor where it is compressed to a higher temperature and enthalpy through the addition of work energy. The refrigerant then enters the condenser where heat is rejected to the surroundings as the fluid condenses. From the condenser, the refrigerant flows to the receiver where any excess refrigerant charge is stored. The fluid exiting the receiver is in the saturated liquid condition. The fluid then passes through an expansion device where the pressure drops at nearly constant enthalpy. The next component in the loop is the evaporator, where the refrigerant evaporates as it absorbs heat from the surroundings. The refrigerant leaving the evaporator flows to an accumulator where any two-phase fluid is captured, thus preventing damage to the compressor. From this point the refrigerant repeats the cycle.

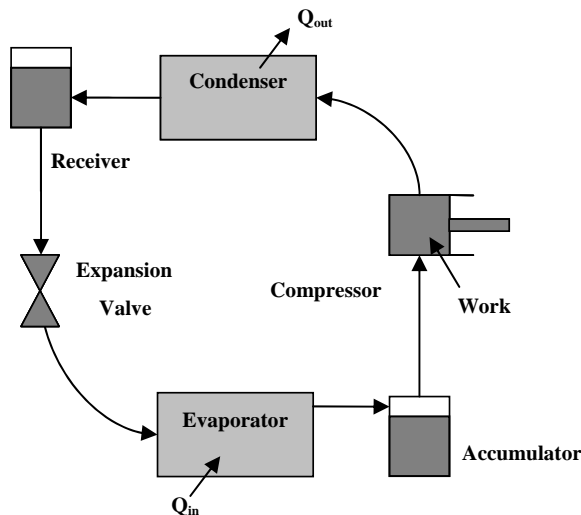


Figure 1.1 Components of the basic vapor compression cycle

1.1.2 Efficiency

A 2004 National Renewable Energy Laboratory (NREL) study found that the United States uses 7 billion gallons (26.4 billion Liters) of fuel per year for light-duty vehicle air-conditioning alone, equivalent to 5.5% of the total national light-duty vehicle fuel use. It would take 9.5% of the U.S. imported oil to produce this much gasoline [37].

Statistics compiled by the Energy Information Administration for 2001 indicate that 82.9 million US households have some type of air-conditioning system. One hundred eighty-three (183) billion kWh of home electricity were consumed to power these home air-conditioners. That energy consumption is equivalent to 15.94 billion dollars. Trends indicate that air-conditioning is being used in more homes and is being used more often [15]. Data from 1999 showed commercial energy use for cooling required energy expenditures of 72.2 billion dollars. Refrigeration energy expenditures exceeded 40 billion dollars [14]. Considering the huge expenditures associated with air-conditioning and refrigeration, even modest gains in VCC system efficiency will result in substantial reductions in energy usage on a national scale. The associated economic and environmental benefits are clear.

1.1.3 Advantages of Feedback Control

The application of advanced feedback control techniques to VCC systems is motivated by the desire to increase system efficiency. Feedback control allows the system to match its capacity to a required load without cycling the compressor on and off. Variable speed or variable displacement continuous compressor operation has been shown to be more efficient than compressor cycling [27]. Control also allows for the regulation of the level of superheat at the evaporator outlet. By maintaining a low level of superheat, the evaporator operates in its most efficient wet condition, and the compressor is not slugged with liquid refrigerant. The current industry standard for superheat control is the thermostatic expansion valve. These valves regulate superheat, but are only effective near a single operating condition. Feedback control used in conjunction with an electronic expansion valve and variable speed compressor allows for superheat and capacity regulation over the entire system operating range through techniques such as gain scheduling [41].

1.1.4 Model-based Control

Vapor compression cycles are frequently used as multiple-input multiple-output (MIMO) systems. The inputs, or actuators, could include the expansion device, the compressor, and the heat exchanger fans. The outputs to be controlled are typically superheat and capacity. Research has shown that coordinated MIMO control of these two outputs is more effective than separate single-input single-output (SISO) control loops [42, 21]. Due to the highly coupled nature of these systems, SISO control loops will fight one another, an effect that is very detrimental to performance.

In order to effectively design and evaluate MIMO control techniques, an accurate system level dynamic VCC model is required. Such a model is available in Thermosys, a MATLAB toolbox developed at the University of Illinois under the auspices of the Air-Conditioning and Refrigeration Center. Thermosys contains low-order dynamic models of heat exchangers and static models of the other basic components of VCC systems. The heat exchangers are modeled with a moving-boundary approach, which produces models of lower dynamic order than the more common finite difference approach. The individual component models are combined in Simulink to create an overall system level model. The linearized system model is a valuable tool for the control designer. The state of

Thermosys at the commencement of this research effort is described in Chapter 2, as well as model additions and improvements that will be covered in this thesis.

1.1.5 Industry Need

To the author's knowledge, no software package incorporating low-order moving-boundary dynamic heat exchanger models is commercially available. Numerous researchers have developed moving-boundary models, but the models have not been made available as software to either the industrial or the academic community. The HVAC industry stands in need of a software tool capable of simulating the dynamics of VCC cycles. Many finite difference modeling tools are on the market, but Thermosys is the only available tool containing compact, control-oriented moving-boundary heat exchanger models.

1.2 Objectives

The main objective of the research presented in this thesis is to advance the state-of-the-art of system level VCC models based on the moving-boundary paradigm. Increased simulation accuracy is achieved by incorporating improvements and additions to both static and dynamic models, including the addition of environmental effects (humid air) on heat exchanger behavior.

The secondary objective is to increase confidence in the moving-boundary models through presentation of extensive model validation results. Model validation results are one area of moving-boundary model research that has been lacking in the literature. All modeling improvements and additions presented in this work are validated with experimental data as much as time and resources permit.

1.3 Literature Review

Modeling of VCC systems can be divided into two general paradigms: finite difference (spatially dependent) models and moving-boundary models [4]. The following sections give a brief discussion of finite difference modeling and an examination of existing moving-boundary models. A more detailed examination of the deficiencies of previous moving-boundary models is found in Chapter 2.

1.3.1 Finite Difference Models

In the finite difference paradigm, the conservation equations are approximated with a finite difference technique and applied to a number of elements in the heat exchanger [33]. Each element contains its own dynamic states and is independent of fluid phase. As the number of elements increases, model accuracy increases as well. However, the increased number of elements results in a dynamically large model that may be computationally expensive and is unsuitable for model-based control design [3]. Gruhle and Isermann presented this method in 1984 [18], and it has been utilized by numerous researchers. Finite difference models are available in a number of commercial software packages.

1.3.2 Moving-boundary Models

In the moving-boundary modeling approach, the heat exchangers are divided into regions based on the fluid phase in each region. The complex heat exchanger geometry is reduced to an equivalent single pipe. Model parameters are lumped together in each region. The location of the boundary between regions is allowed to be a dynamic variable, thereby capturing the essential two-phase flow dynamics. The resulting models are of low dynamic order, making them very well suited for control design. The moving-boundary models give the model

developer and control designer physical insight into the dynamic behavior of the plant. In comparison to the finite difference models, the compact nature of the moving-boundary models is assumed to reduce accuracy, although no direct model validation comparison is available in the literature. Grald and MacArthur (1992) showed that a spatially dependent model and a moving-boundary model for an evaporator have very similar dynamic responses [17].

Moving-boundary models have been under development since 1979 [11]. A review of the literature shows that they have been applied to a variety of VCC systems with many variations in the details of the modeling approach [4]. Broersen and van der Jagt (1980) developed a moving-boundary model of an evaporator to analyze hunting behavior in thermostatic expansion valves [6]. Validation of the model is not presented. Kapadia (1984) presented very limited validation for a moving-boundary condenser model in a Rankine cycle [24]. Grald and MacArthur (1992) developed a moving-boundary model of an evaporator as part of a heat pump model. Model validation results are again limited [17]. He (1997) presented linearized moving-boundary models for both an evaporator and a condenser, with the stated purpose of designing feedback controllers. Adequate model validation results were included [20, 21]. Numerous authors have presented similar models to those discussed, but with some extensions to the modeling framework [23, 47, 38]. Rasmussen (2004) derived moving-boundary models for transcritical cycles, while previous authors have focused on sub-critical cycles [42].

1.3.3 Model Validation

The models presented in this work are applicable to both dynamic analysis and control. The intended application dictates the necessary level of accuracy. The model validation process attempts to determine if the given model meets the specified level of accuracy, where accuracy is determined by comparing model output to experimental data. A good overview of various model validation approaches is found in [12]. Strictly speaking, a model can not be validated by a finite set of data [39], only invalidated. However, each successful validation effort increases the user's confidence in the model.

The process of model validation can be used to answer two questions. The first is a qualitative question: does the model accurately describe the essential characteristics of the system? The second is a quantitative question: What is the level of agreement between the model and the real system? The qualitative question is typically addressed first in the model development process. Pursuing quantitative model validation makes little sense if the model obviously does not capture the salient dynamic behavior of the system. Once the qualitative accuracy requirement has been satisfied, quantitative model accuracy may be addressed. By quantifying accuracy, researchers can compare models, evaluate the value of changes to the model, and track progress. The quantitative validation results presented in this work use RMS error and similar metrics to compare the accuracy of various models.

1.4 Organization

Chapter 2 describes previous moving-boundary modeling work, with specific emphasis placed on the models developed within the Alleyne Research Group. In examining the existing state-of-the-art, areas for potential improvement are identified. Chapter 3 describes various semi-empirical methods for improving model accuracy, including improved static mass flow models and heat transfer models. Modeling of environmental conditions is

described in Chapter 4. New dynamic models and dynamic additions to existing static models are described in Chapter 5. Chapter 6 gives an overview of the experimental system used to generate data for model validation tests. The model validation results for the various static and dynamic modeling improvements and additions are presented in Chapter 7. The thesis concludes in Chapter 8 with a summary of the results and directions for future research.

Chapter 2. Previous VCC Modeling

Vapor compression cycle system modeling has been an ongoing research topic within the Alleyne Research Group since 2000. Industry interest in the initial modeling efforts led to the creation of the Thermosys Toolbox for MATLAB. This chapter will first review the status of Thermosys as of Fall 2004 [40, 44], with some comparisons to the moving-boundary models developed by other researchers. An overview of modeling needs addressed in this thesis is then presented.

2.1 Moving-boundary Heat Exchanger Modeling

Modeling of heat exchangers is complicated by the presence of two-phase fluid flow and complex geometry, both on the refrigerant side and the air side. The moving-boundary approach is based on the assumption of one-dimensional fluid flow through a pipe with effective diameter, flow length, and surface areas. The approach also assumes equal pressure throughout the heat exchanger. The heat exchanger is divided into regions based on the fluid phase, and effective parameters are lumped in each region. The location of the interface between fluid phase regions is allowed to be a dynamic variable.

The derivation procedure requires the integration of the governing partial differential equations (PDEs) along the length of the heat exchanger to remove spatial dependence. The PDEs for conservation of refrigerant mass and energy are given in Equation 2.1 and Equation 2.2. They are integrated using the integration rule given in Equation 2.4. The conservation of energy equation for the heat exchanger wall energy is given in Equation 2.3.

$$\frac{\partial(\rho A_{cs})}{\partial t} + \frac{\partial(\dot{m})}{\partial z} = 0 \quad (2.1)$$

$$\frac{\partial(\rho A_{cs} h - A_{cs} P)}{\partial t} + \frac{\partial(\dot{m} h)}{\partial z} = p_i \alpha_i (T_w - T_r) \quad (2.2)$$

$$(C_p \rho A)_w \frac{\partial(T_w)}{\partial t} = p_i \alpha_i (T_r - T_w) + p_o \alpha_o (T_a - T_w) \quad (2.3)$$

$$\int_{z_1(t)}^{z_2(t)} \frac{\partial f(z, t)}{\partial t} dz = \frac{d}{dt} \left[\int_{z_1(t)}^{z_2(t)} f(z, t) dz \right] - f(z_2(t), t) \frac{d(z_2(t))}{dt} + f(z_1(t), t) \frac{d(z_1(t))}{dt} \quad (2.4)$$

An evaporator will be considered as an example of the application of the moving-boundary modeling approach. The fluid entering the evaporator is assumed to be two-phase, while the fluid exiting the evaporator is superheated vapor. Thus the evaporator is modeled with two regions as shown in Figure 2.1. The lumped air temperature across the evaporator is assumed to be a weighted average of the inlet and outlet air temperatures. The fluid properties in the first (two-phase) region are characterized using the mean void fraction, e.g.

$\rho_1 = \rho_f (1 - \bar{\gamma}) + \rho_g (\bar{\gamma})$, while properties in the second (superheat) region are averaged based on the inlet and outlet properties, e.g. $h_2 = (h_g + h_{out}) / 2$.

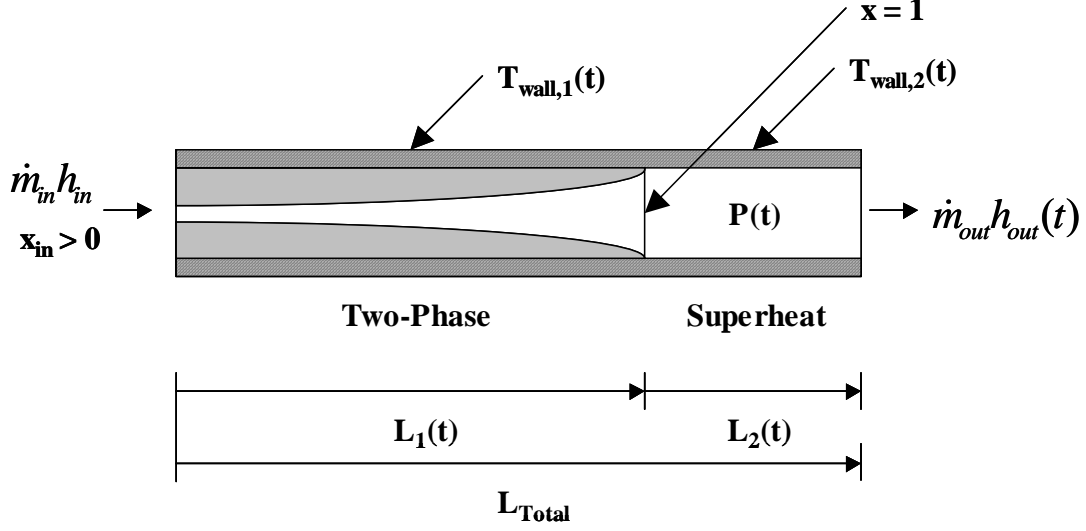


Figure 2.1 Evaporator fluid regions

Integration of the three conservation equations for each region results in six equations that can be simplified into a nonlinear state space form, $Z(x,u) \cdot \dot{x} = f(x,u)$, where the elements of $Z(x,u)$ and $f(x,u)$ are nontrivial and presented in detail in [40]. The states of the evaporator model, which are a result of the derivation procedure, are the length of two-phase flow, the evaporation pressure, the outlet enthalpy, and the two lumped wall temperatures, shown symbolically in Equation 2.5. The inputs to each of the component models are generally outputs of other component models. The inputs to the evaporator model are the inlet and outlet refrigerant mass flow rates (outputs of the valve and compressor models), the inlet enthalpy (output of the valve model), and the temperature and mass flow rate of air (inputs to the overall system), given symbolically in Equation 2.6

$$x_e = [L_{e1} \quad P_e \quad h_{e,out} \quad T_{ew1} \quad T_{ew2}]^T \quad (2.5)$$

$$u_e = [\dot{m}_{e,in} \quad \dot{m}_{e,out} \quad h_{e,in} \quad T_{e,air,in} \quad \dot{m}_{e,air}]^T \quad (2.6)$$

Industry interest in the moving-boundary models developed within the Alleyne Research Group led to the creation of Thermosys, a MATLAB Toolbox. Thermosys contains linear and nonlinear Simulink models of the basic components of VCC systems, including heat exchangers, compressors, and expansion devices. Individual Thermosys component models are connected in Simulink to create a complete system. The component models are added to the system model using Simulink's drag-and-drop functionality. Model users set physical parameters and initial conditions through component graphical user interfaces.

When the research presented in this thesis was initiated, Thermosys contained moving-boundary heat exchanger models of an evaporator, a condenser, and a gas cooler. Both linear and nonlinear versions of these models were available. In addition, a lumped-parameter internal counter-flow heat exchanger was included in the model library. This collection of heat exchanger models was fairly comprehensive when compared to the models produced by other researchers (see Chapter 1 literature review). The heat exchangers could be used in subcritical, transcritical, and multi-evaporator cycles. Notably absent from the Thermosys model library were receivers and

accumulators. At least one of these two components has also typically been absent from many other moving-boundary modeling efforts as well [20, 47, 23, 17, 11, 9].

An inherent feature of moving-boundary models is the connection between the number of dynamic states and the number of fluid regions in the heat exchanger model. If system transients cause a fluid region to appear or disappear, then the number of states in the model changes. Handling the mathematical effects of adding and removing states is challenging. Some researchers [11, 47] have proposed a modeling-switching scheme whereby multiple modeling frameworks are used in a single simulation. At the commencement of this research, the Thermosys models did not have the ability to simulate heat exchangers with a changing number of fluid regions. This situation occurs frequently in heat exchangers connected with receivers or accumulators and always occurs during system start-up and shut-down.

2.2 Static Valve Modeling

The only expansion device available in Thermosys was an electronic expansion valve. Since the models were originally developed as a control design tool, including a valve suited to electronic control made sense. The valve model required some restrictive assumptions. The mass flow rate model is given in Equation 2.7.

$$\dot{m}_v = A_v C_v [\rho_v (P_{in} - P_{out})]^{1/2} \quad (2.7)$$

The valve area, A_v , was assumed to be linearly related to the control input, u_v , as shown in Equation 2.8.

$$A_v = \beta_1 + \beta_2 u_v \quad (2.8)$$

The discharge coefficient, C_v , was assumed to be a function of the Reynolds number in Equation 2.9.

$$C_v = \beta_3 \left(1 + \frac{\beta_4}{\text{Re}} \right) \quad (2.9)$$

The framework described above is somewhat restrictive to the model user. If an industrial user had an alternate theoretical valve modeling framework or an empirical modeling framework, that framework would be excluded from use in Thermosys. All model users were required to identify the three parameters in Equation 2.8 and Equation 2.9 for their valves. Other moving-boundary model developers have generally not included valve modeling details, such as calculation of the discharge coefficient, in their publications.

2.3 Static Compressor Modeling

Like the valve, the variable speed compressor was modeled as a static component based on empirical parameters. Some researchers have attempted to model compressor dynamics [11, 47], while others [20, 23] assume a static model. The mass flow equation for the compressor model is given in Equation 2.10.

$$\dot{m}_k = \omega_k V_k \rho_k \eta_{vol} \quad (2.10)$$

The volumetric efficiency was calculated from the assumed function of pressure ratio shown in Equation 2.11.

$$\eta_{vol} = 1 + C_k - D_k \left(\frac{P_{out}}{P_{in}} \right)^{1/n} \quad (2.11)$$

The compressor outlet enthalpy was calculated from Equation 2.12.

$$h_{out} = \frac{1}{\eta_a} [h_{out, isentropic} + h_{in}(\eta_a - 1)] \quad (2.12)$$

The adiabatic efficiency was also assumed to be a function of pressure ratio, as given in Equation 2.13.

$$\eta_a = A_k \left(\frac{P_{out}}{P_{in}} \right) + B_k \quad (2.13)$$

In similarity to the valve models, the volumetric and adiabatic efficiencies were based on equations whose structure was predetermined by the model developers. A user's existing compressor modeling framework was precluded from application in Thermosys.

2.4 Modeling Challenges

During the course of the research, the following areas were identified as modeling challenges, or areas where the existing Thermosys models could be expanded or improved. Some of the modeling challenges are specific to Thermosys, while others are challenges that have faced numerous moving-boundary model developers. The incorporation of semi-empirical techniques for describing model parameters is an improvement to the existing Thermosys models that has been used frequently by other model developers. Modeling humidity effects is common practice in steady-state VCC modeling, but, to the author's knowledge, this work demonstrates the first application of humidity effects to moving-boundary models. The incorporation of receiver/accumulator models is not new to moving-boundary modeling. This work, however, presents a unique approach that does not require switching model structures during simulation. The compressor shell dynamic has been included in other models; it is considered to be a necessary improvement to the Thermosys Toolbox. Finally, the simulation of very large transients is a challenge to all moving-boundary models. Most researchers use a switching scheme when simulating large transients. This work evaluates the approaches of other model developers as well as the current capabilities of Thermosys for large transient simulation.

2.4.1 Accurate Model Parameters

Potential improvements in model parameter estimation were identified in both the heat exchangers and the mass flow devices. In the existing heat exchanger models, the initial air-side heat transfer coefficients were either assumed by the user or calculated from other initial conditions (with necessary assumptions). During simulation, the air-side heat transfer coefficient was found by simply scaling the initial value with changes in the mass flow rate of air across the heat exchanger, as shown in Equation 2.14.

$$\alpha_o = \alpha_{o, initial} \left(\frac{\dot{m}_{air}}{\dot{m}_{air, initial}} \right)^n \quad (2.14)$$

A more rigorous approach to predicting this dominant thermal parameter was encouraged by industry sponsors of the project.

The key model parameters in the valve are the area and the discharge coefficient. In the compressor, the key model parameters are the volumetric efficiency and the adiabatic efficiency. As discussed above, in the original Thermosys models, users were constrained to use the equation structure for these parameters that was provided by

the developers. These parameters were identified as being very critical to system level model accuracy. A semi-empirical approach that blends the first-principles models with performance maps was employed to make the models more flexible as well as more accurate over a large range of operating conditions. The semi-empirical heat transfer and static mass flow device modeling improvements are described in Chapter 3.

2.4.2 Atmospheric Conditions

A fundamental limitation of the original heat exchanger models was the assumption that the air passing over the heat exchangers was completely dry. This condition would seldom exist in reality, and the prediction of dehumidification effects and the onset of condensation are important application issues. The only air-side parameters affecting the models were air mass flow rate and inlet air temperature. Relative humidity of the inlet air also has an effect on system performance. Chapter 4 describes humidity modeling efforts.

2.4.3 Expanding Operating Conditions

The original Thermosys Toolbox contained neither receiver nor accumulator models. Shah [44] presented one approach to modeling these components. However, the models were not distributed with Thermosys because they were very complex and not adequately robust. The majority of VCC systems contain a receiver, an accumulator, or both components. Without robust models of these components, a large number of practical systems could not be simulated by Thermosys. The derivation of unique first-principles condenser with receiver and evaporator with accumulator models is presented in Chapter 5.

2.4.4 Dynamic Compressor Shell Model

The original compressor model assumed the refrigerant outlet enthalpy to be determined by a static relationship, as shown in Equation 2.12. Observations from experimental data indicated that this assumption was not adequate. The simulation outlet enthalpy response was consistently much faster than the actual response to compressor steps. Chapter 5 contains the description of a simple dynamic addition to the compressor outlet enthalpy model that accounts for the compressor shell thermal capacitance.

2.4.5 Large Transient Simulation

Attempts to validate models with large compressor step inputs revealed that the models were not capable of accurately predicting critical outputs. Chapter 5 presents an iterative learning control (ILC) method for reducing pressure prediction errors caused by large input steps. Mass flow rate prediction errors are identified as the likely source of significant pressure prediction errors occurring during large transients. Potential sources of mass flow errors include the compressor or unmodeled components such as the oil separator. Due to the lack of a high side mass flow sensor, the compressor model is one of the most uncertain components in the system. Finally, an evaluation of possible methods for handling the challenges of compressor cycling and start-up/shut-down transients are presented, as well as an examination of current cycling simulation capabilities.

Chapter 3. Semi-empirical Models

Semi-empirical models combine first-principles component models with experimental data to improve the system level simulation accuracy. By using data-driven correlations, accuracy is increased without increasing the model's dynamic complexity.

3.1 External Heat Transfer Coefficients

A critical heat exchanger design parameter is the overall thermal resistance between the internal and the external fluids. In the case of refrigerant-to-air heat exchangers, the air-side heat transfer coefficient is often the dominating component of this thermal resistance. A heat exchanger model should be able to accurately predict the air-side heat transfer coefficient through the entire feasible range of air mass flow rates. An accurate external heat transfer coefficient contributes to the model's ability to transition to a correct steady-state operating condition following a change in the model inputs.

3.1.1 Empirical Heat Transfer Model

A semi-empirical modeling approach is applied to increase the accuracy of air-side heat transfer coefficient predictions. A more accurate air-side heat transfer coefficient prediction results in an improved model of the flow of energy from the heat exchanger wall to the surrounding air, and therefore, an improved model of the overall system dynamics. The semi-empirical model used here is the Colburn j factor. The j factor provides a means of correlating experimentally determined heat transfer characteristics of a heat exchanger with the Reynolds number of air flowing through the heat exchanger [22]. The correlation is of the form given in Equation 3.1.

$$j = StPr^{2/3} \quad (3.1)$$

The Stanton number in Equation 3.1 is based on the air-side heat transfer coefficient, α_o :

$$St = \frac{\alpha_o}{G \cdot C_p} \quad (3.2)$$

The maximum mass velocity, G , is a function of the mass flow rate of air through the heat exchanger; C_p is the specific heat of air. By combining Equation 3.1 and Equation 3.2, we arrive at an expression for the external heat transfer coefficient, as given in Equation 3.3.

$$\alpha_o = \frac{j \cdot G \cdot C_p}{Pr^{2/3}} \quad (3.3)$$

3.1.2 Sources of Empirical Heat Transfer Data

A heat exchanger's j factor data as a function of Reynolds number is typically presented graphically or in tabular form, as in the classic work of Kays and London [25]. Figure 3.1 shows an example of a typical j factor vs. Reynolds number plot. Correlations for determining the j factor of various heat exchanger geometries are available in the literature.

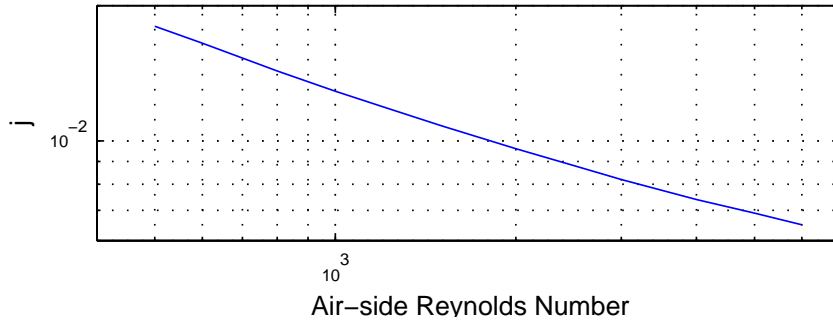


Figure 3.1 The experimentally obtained j factor plot for surface CF-8.72 from [25]

3.1.2.1 Experimental System Condenser j Factor

The experimental system condenser j factor data is obtained from a plain-fin heat exchanger correlation proposed by [45]. The MATLAB code used to implement the correlation is given in Appendix A. The condenser j factor is plotted as a function of Reynolds number in Figure 3.2.

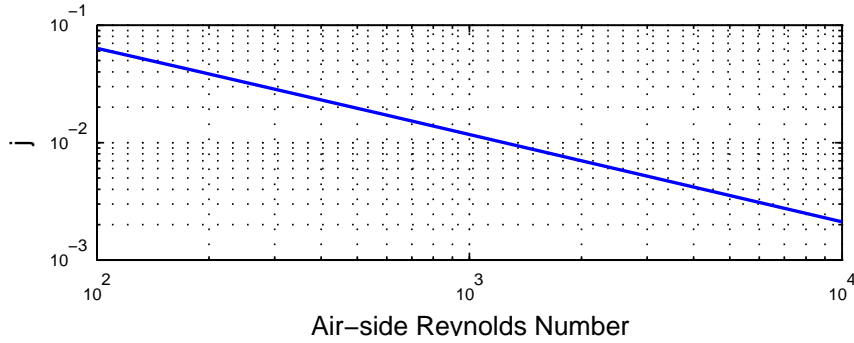


Figure 3.2 Experimental system condenser j factor from correlation

3.1.2.2 Experimental System Evaporator j Factor

The j factor data for the second evaporator is obtained from a wavy-fin heat exchanger correlation proposed by [28]. The MATLAB code used to implement the correlation is given in Appendix A. The j factor is plotted as a function of Reynolds number in Figure 3.3.

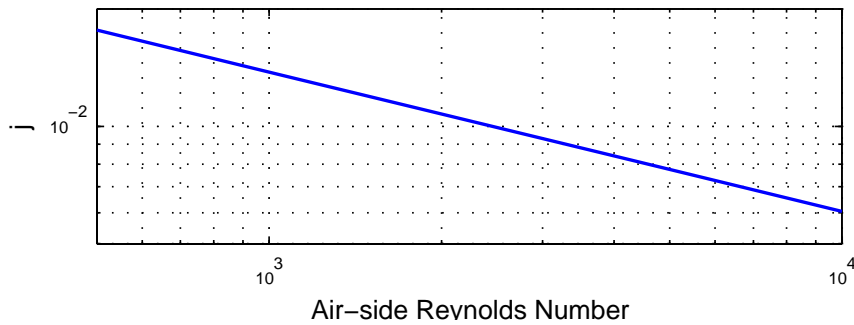


Figure 3.3 Experimental system evaporator j factor from correlation

3.1.3 Implementation in Thermosys

During simulation of a heat exchanger, the mass flow rate of air is assumed to be a known input. Using this mass flow rate, an air-side Reynolds number is calculated and used to find a j factor value from the experimental data. The Reynolds number is found from Equation 3.4.

$$Re = \frac{G \cdot D_h}{\mu} \quad (3.4)$$

The air viscosity, μ , is found from a lookup table with an average air temperature input. The hydraulic diameter, D_h , is a property of the heat exchanger geometry as defined in Equation 3.5.

$$D_h = 4L \cdot \frac{A_c}{A} \quad (3.5)$$

The flow length, L , is defined as the distance the air travels through the heat exchanger from the leading edge of the first row of tubes to the leading edge of an additional fictitious row of tubes located at one longitudinal tube pitch behind the last row of tubes. For example, in Figure 3.4, the heat exchanger flow length would be $L = 3$ inches.

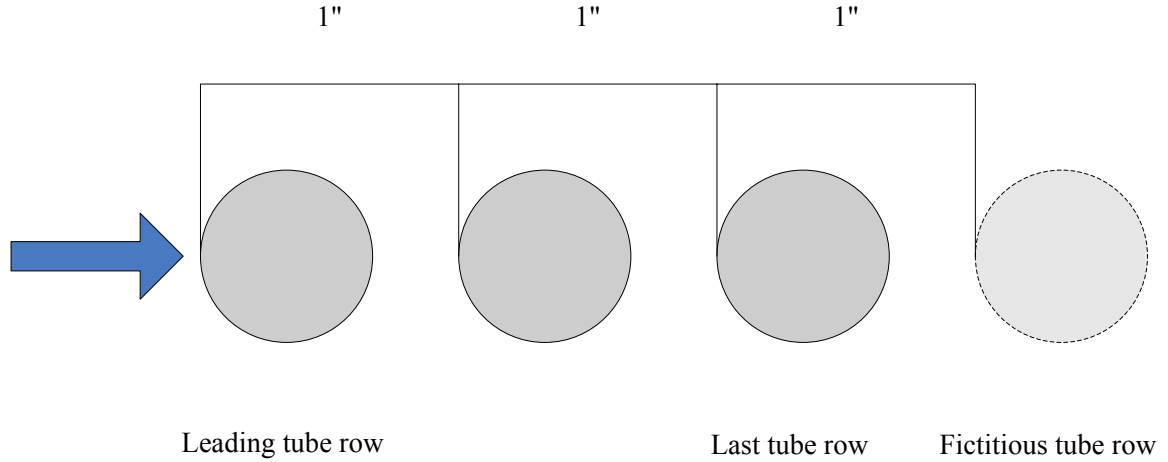


Figure 3.4 Example calculation of heat exchanger flow length

The parameter A in Equation 3.5 is the total heat transfer area. In a tube-and-fin heat exchanger, this parameter would be found from the combined surface area of all external tube walls and fins. The parameter A_c is the minimum free flow area. To determine this parameter, first find the plane in the heat exchanger where air flow is the most constricted. At this plane, subtract the cross-sectional area of all flow obstructions (tubes and fins) from the total frontal area of the heat exchanger. An example is given in Figure 3.5.

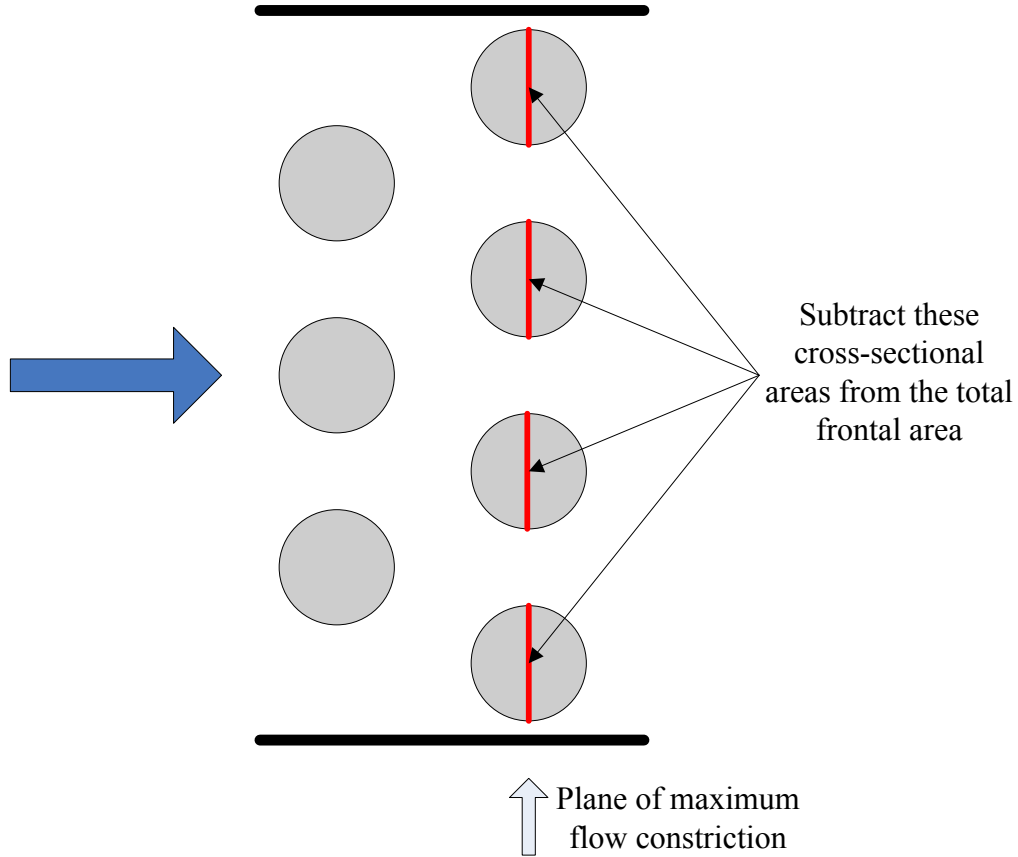


Figure 3.5 Plane of maximum flow constriction used in calculation of the minimum free flow area

Unfortunately, the hydraulic diameter (Equation 3.5) is not used consistently in the literature. Some authors prefer to develop correlations based on the collar diameter, such as the correlation [28] used for the experimental system's second evaporator. The collar diameter is defined in Equation 3.6, where D_o is the tube outside diameter and δ_f is the fin thickness.

$$D_c = D_o + 2\delta_f \quad (3.6)$$

The simulation Reynolds number must be calculated from the same diameter, D_h or D_c , that was used to reduce experimental heat transfer data to a j factor correlation.

Returning to Equation 3.4, the only remaining parameter to be calculated is G , the maximum mass velocity. This parameter is found from Equation 3.7.

$$G = \frac{\dot{m}_{air}}{\sigma \cdot A_{fr}} \quad (3.7)$$

A_{fr} is the frontal area and σ , the constriction ratio, is the ratio of the minimum free flow area, A_c , to the frontal area.

An empirically-based external heat transfer coefficient is calculated from Equation 3.3 at each time step of the simulation. A Simulink block diagram of the calculations carried out in Thermosys is shown in Figure 3.6.

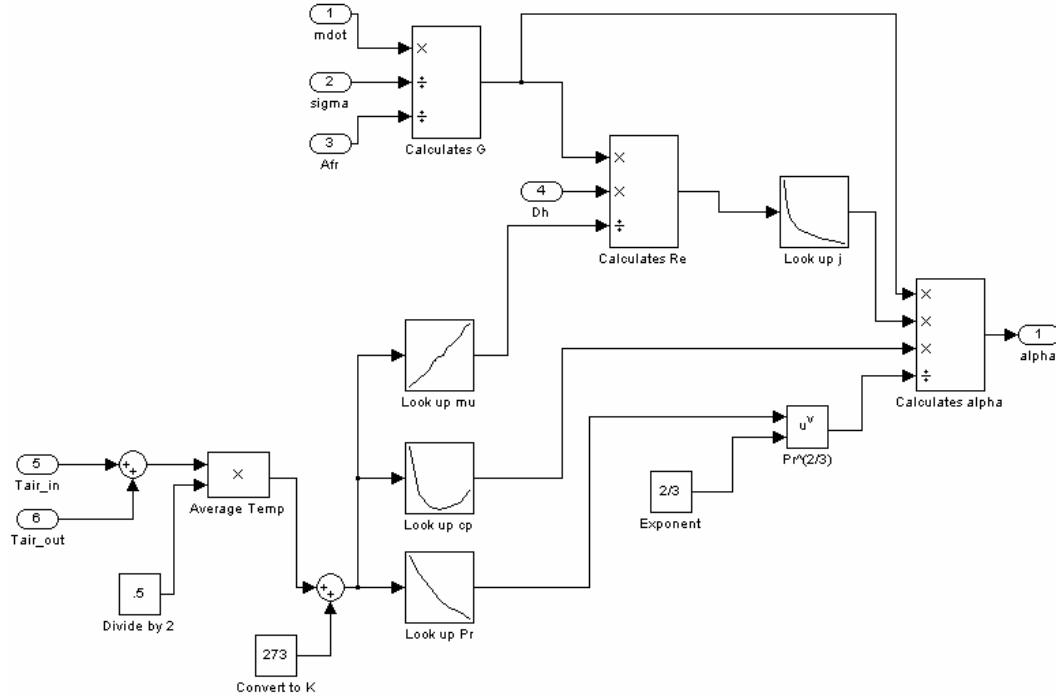


Figure 3.6 Block diagram of heat transfer coefficient calculation from j factor data

The j factor and Reynolds number data points for a variety of heat exchanger geometries from [25] are stored in a MATLAB data structure called HX. The structure also contains the geometric information necessary for calculating a heat transfer coefficient from the j factor. The structure fields and their contents are summarized in Table 3.1. Thermosys developers and users can easily add additional data to the HX structure.

Table 3.1 Fields in the HX data structure

Field Name	Field Contents
Core	name of the core geometry assigned by Kays and London
Num	number indicating the location of the heat exchanger in the HX structure
Redat	row vector of Reynolds number data points
jHdat	row vector of j factor data points
sigma	the constriction ratio
Dh	the air-side hydraulic diameter

Results presented in Chapter 7 demonstrate the increase in system level model accuracy obtained by using this semi-empirical modeling approach in the heat exchangers. Incorporating empirical results in this fashion improves model fidelity without increasing the dynamic complexity of the model.

3.2 Performance Mapping

The performance mapping approach presented here is based on the availability of large amounts of component experimental data. The data is used to characterize the key parameters in the mass flow models with performance maps. Performance maps can also be generated from other modeling frameworks. For example, if a strictly first-principles approach is used to model a component, then the model output could be treated as data and used to generate a performance map. Figure 3.7 shows the range of valve and compressor settings used to generate

the electronic expansion valve performance map and the compressor efficiency maps for the experimental system described in Chapter 6. The operating conditions produced by these inputs are shown in Figure 3.8. Similar inputs are used to generate data for mapping the other components described in this section. The experimental system that is the source of the performance mapping data is described in Chapter 6.

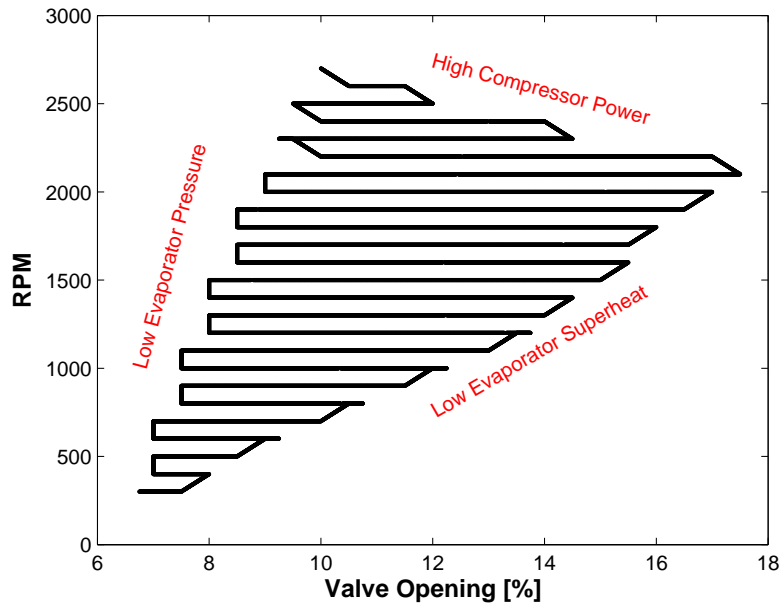


Figure 3.7 Compressor speed and valve opening settings

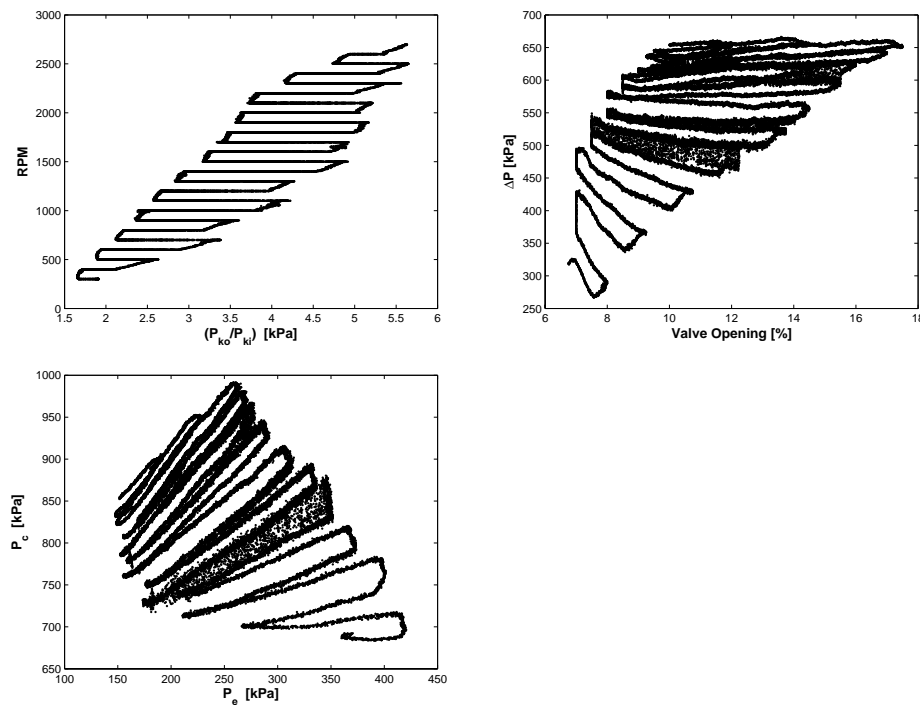


Figure 3.8 Range of operating conditions covered by performance maps

The changes in system inputs should be sufficiently slow that each operating condition can be considered nearly steady-state. The steady-state operating conditions should cover the feasible range of high side and low side pressures for the system.

The mapping approach discussed here provides greater flexibility to the model user when compared to the equation-based approach previously implemented in Thermosys. If a user has an existing model, it can be utilized in Thermosys by simply converting it to a performance map form. The only restriction is that the user model has the same inputs as the Thermosys performance map. The performance mapping approach is applied to valve flow coefficients and compressor volumetric and adiabatic efficiencies.

3.2.1 Valves

Thermosys valve models provide a mass flow rate for the condenser outlet and the evaporator inlet. Due to time scale separation [41], the valve mass flow may be modeled with algebraic relationships. The basic valve mass flow model is given in Equation 3.8. Assuming a sharp orifice, the models presented here use $n = 2$ in Equation 3.8. The main challenge of modeling the valves is determining the discharge coefficient, C_v .

$$\dot{m}_v = A_v C_v [\rho_v (P_{in} - P_{out})]^{1/n} \quad (3.8)$$

The orifice tube and the capillary tube have a fixed valve opening area. The thermostatic expansion valve (TEV), automatic expansion valve (AEV), and electronic expansion valve (EEV) have a variable valve opening area. The variable area valves are differentiated by the means of controlling the valve opening area. In situations where the valve area is variable or unknown, the valve area and discharge coefficient are lumped into a single parameter referred to as the valve flow coefficient, C_f .

$$\dot{m}_v = C_f \sqrt{\rho_v (P_{in} - P_{out})} \quad (3.9)$$

Solve Equation 3.9 for the flow coefficient to obtain Equation 3.10.

$$C_f = \frac{\dot{m}_v}{\sqrt{\rho_v (P_{in} - P_{out})}} \quad (3.10)$$

If the valve area is known, the discharge coefficient may be obtained directly from Equation 3.11.

$$C_v = \frac{\dot{m}_v}{A_v \sqrt{\rho_v (P_{in} - P_{out})}} \quad (3.11)$$

Using experimental measurements of mass flow rate, inlet refrigerant density, inlet pressure, and outlet pressure, the flow coefficient or discharge coefficient is calculated for a large number of steady-state operating conditions.

Once the flow coefficient data points are obtained, an equation model is then fit to the data. This equation fitting is carried out using a least-squares linear regression method. The best fit equation is then used to generate a lookup table for implementation in Thermosys. The quality of the model may be judged by such metrics as the RMS error between model coefficients and data coefficients or the R^2 value returned by MATLAB's linear regression command.

3.2.1.1 Mapping Procedure for the Electronic Expansion Valve

The valve opening area of the EEV is typically controlled by a stepper motor. The precise relationship between stepper motor position and valve area is often unknown. Therefore, the flow coefficient is used in place of

the valve area and the discharge coefficient. Thermosys contains EEV models with a two input map and a three input map. For the two input map, the inputs are pressure differential across the valve and the valve command signal, as shown in Equation 3.12. For the three input map, the inputs are valve command signal, inlet pressure, and outlet pressure, as shown in Equation 3.13.

$$C_f = f(u_v, \Delta P_v) \quad (3.12)$$

$$C_f = f(u_v, P_{in}, P_{out}) \quad (3.13)$$

Sample code for creating an EEV performance map is found in Appendix A. The most accurate EEV mass flow models have been obtained with the three input flow coefficient performance map. Figure 3.9 shows experimental mass flow data compared to model output from a two-input EEV and a three-input EEV. The three-input EEV is better able to capture the small magnitude mass flow changes.

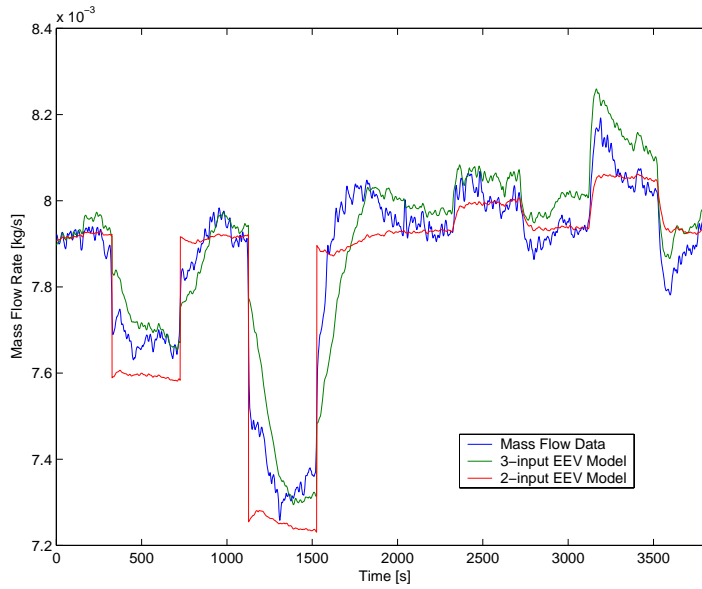


Figure 3.9 Comparison of 2-input and 3-input EEV models with experimental data

If two inputs are used, the performance map may be visualized as a three-dimensional surface. An experimentally obtained EEV map as a function of pressure differential and valve command signal is shown in Figure 3.10. A three input map cannot be visualized in this fashion.

$$C_f (10^{-6}) = (-9.5984) + (2.0481)u_v + (0.0054106)\Delta P + (-0.00074909)u_v\Delta P + (-0.037775)u_v^2$$

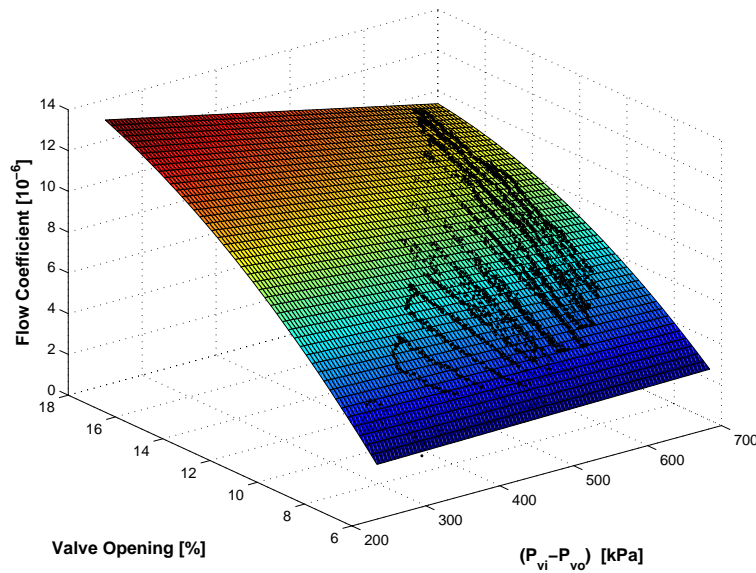


Figure 3.10 Flow coefficient map for an EEV with black points representing experimental data

3.2.1.1 Mapping Procedure for the Automatic Expansion Valve

Automatic expansion valves maintain a constant pressure in either the evaporator or the condenser, depending on the type of valve used. In order to maintain constant pressure, the valve opening area is based on the force balance of a spring and the inlet or outlet pressure on a diaphragm. Therefore, the inlet or outlet pressure is roughly equivalent to the valve command signal in the EEV. Figure 3.11 shows a schematic of an AEV with the spring, diaphragm, and refrigerant flow path visible.

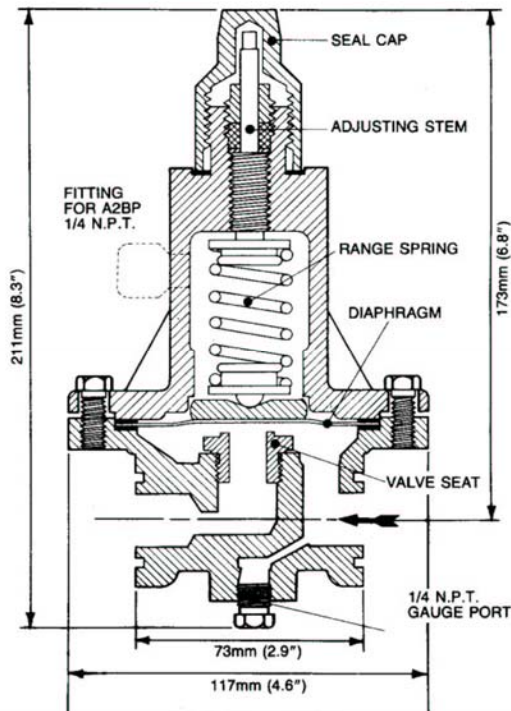


Figure 3.11 Schematic of an AEV [1]

The valve flow coefficient is mapped as a function of the pressure differential and the pressure being regulated, as shown in Equation 3.14. In the case of the experimental system, the outlet (evaporator) pressure is regulated. Sample code for creating an outlet pressure regulating AEV performance map is found in Appendix A, and a performance map with data points is shown in Figure 3.12.

$$C_f = f(P_{regulated}, \Delta P) \quad (3.14)$$

$$C_f = (-1.5796e-005) + (2.2945e-008)\Delta P + (3.2426e-008)P_e$$

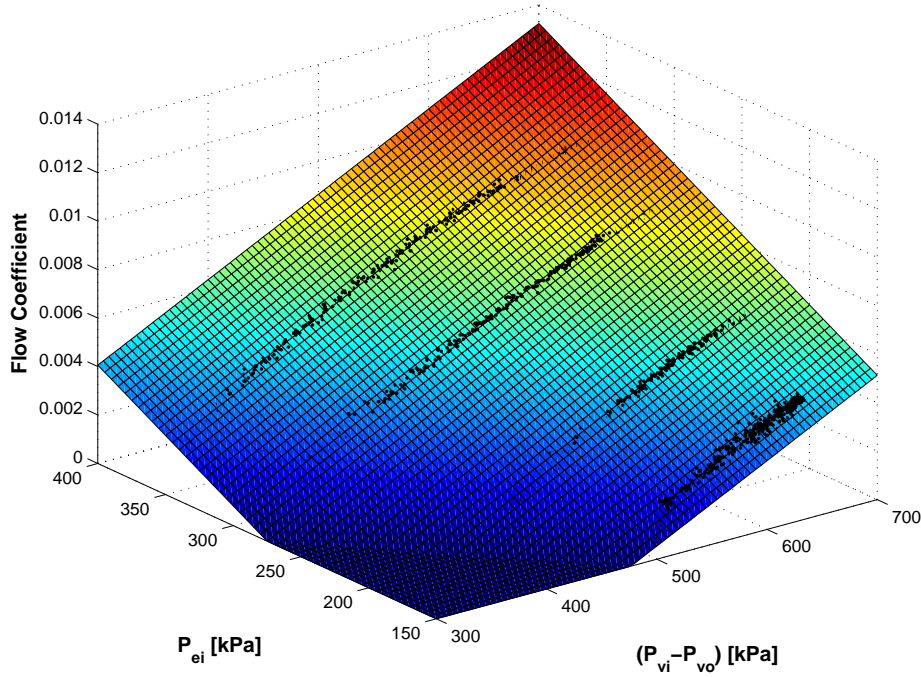


Figure 3.12 Flow coefficient performance map and data points for an AEV

3.2.1.2 Mapping Procedure for the Thermostatic Expansion Valve

Thermostatic expansion valves regulate the level of superheat at the evaporator outlet. The valve opening is determined by a force balance of the evaporator inlet pressure, the saturation pressure of the evaporator outlet temperature, and an adjustable spring force. The saturation pressure of the evaporator outlet temperature is obtained by means of a refrigerant-filled sensing bulb located at the evaporator outlet. The nominal force applied by the spring is adjusted by turning a threaded stem. A TEV schematic showing the principle of superheat regulation is found in Figure 3.13.

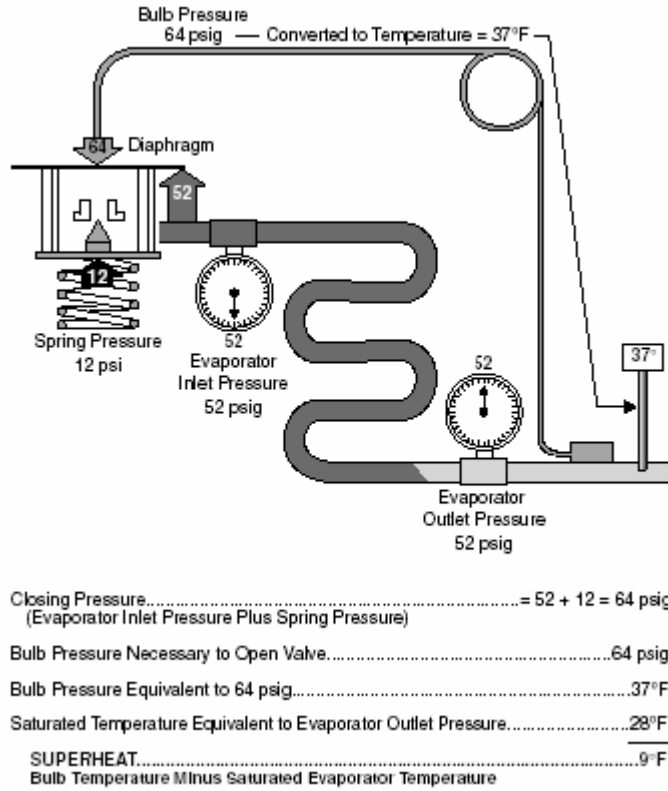


Figure 3.13 Schematic of a TEV and example values for superheat regulation [2]

The valve area and the discharge coefficient may not be lumped into a single parameter in this case because the valve area is a function of two dynamic variables, the sensing bulb pressure and the evaporator pressure. Two maps are required for the TEV, one for the discharge coefficient and one for the area. The discharge coefficient is found directly from Equation 3.15.

$$C_v = \frac{\dot{m}_v}{A_v \sqrt{\rho_v (P_{in} - P_{out})}} \quad (3.15)$$

The discharge coefficient is mapped as a function of the pressure differential and the number of preload turns on the spring, as shown in Equation 3.16. The mass flow rate, the inlet density, and the pressures are provided by experimental data.

$$C_v = f(\Delta P, \text{turns}) \quad (3.16)$$

The valve area is assumed to be a function of the difference between the evaporator pressure and the bulb pressure, as shown in Equation 3.17.

$$A_v = f(P_{bulb} - P_{evap}) \quad (3.17)$$

Calculation of the valve area from experimental data requires knowledge of numerous valve parameters, such as the obstructing tip angle, the spring constant, and the valve opening area. The TEV mapping code in Appendix A identifies the necessary physical parameters and their use in determining the valve opening area from experimental data.

For simulation purposes, a time constant, τ_{bulb} , is needed to account for the dynamic associated with the transfer of energy from the evaporator outlet refrigerant through the pipe wall to the sensing bulb. During simulation, the bulb pressure is found by integrating the bulb pressure derivative, shown in Equation 3.18. The bulb time constant, which is chosen by the user, is not needed in the mapping process because steady-state data is used to generate the maps.

$$\dot{P}_{bulb} = \frac{P_{sat}(T_{evap,out}) - P_{bulb}}{\tau_{bulb}} \quad (3.18)$$

The sample code in Appendix A uses valve geometry and parameter assumptions to generate a discharge coefficient map and an area map. The sample code approach loosely follows that of [31].

A discharge coefficient map generated using the assumed valve parameters is shown in Figure 3.14; the corresponding valve area map is shown in Figure 3.15. The sample maps may not be a numerically accurate reflection of the system TEV, but the qualitative behavior should be captured by the model. Finding TEV physical parameters is a non-trivial challenge. Manufacturers generally do not provide detailed valve geometry. For that reason, the Thermosys TEV model has not been validated.

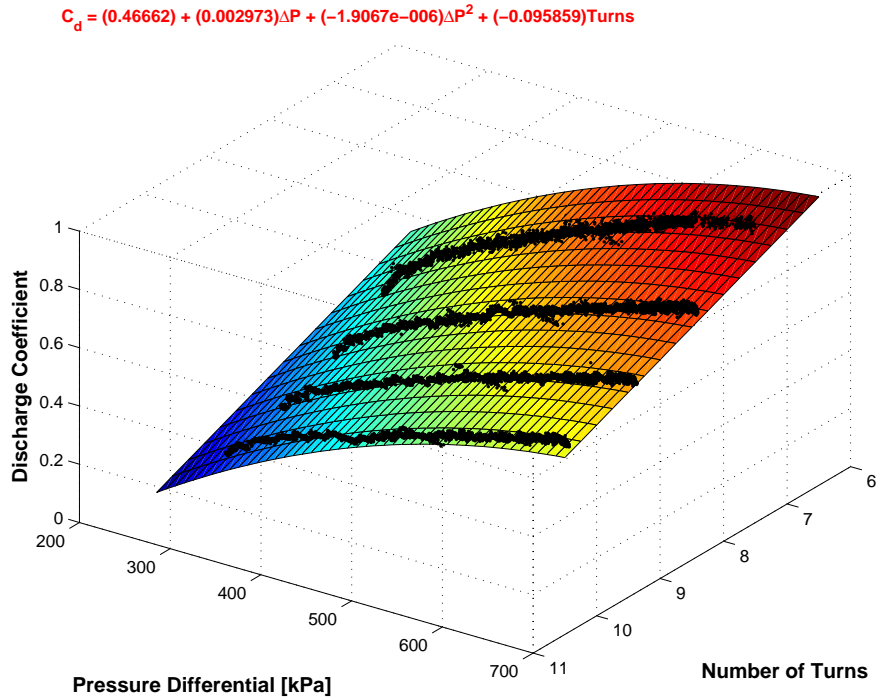


Figure 3.14 TEV discharge coefficient performance map and generating data

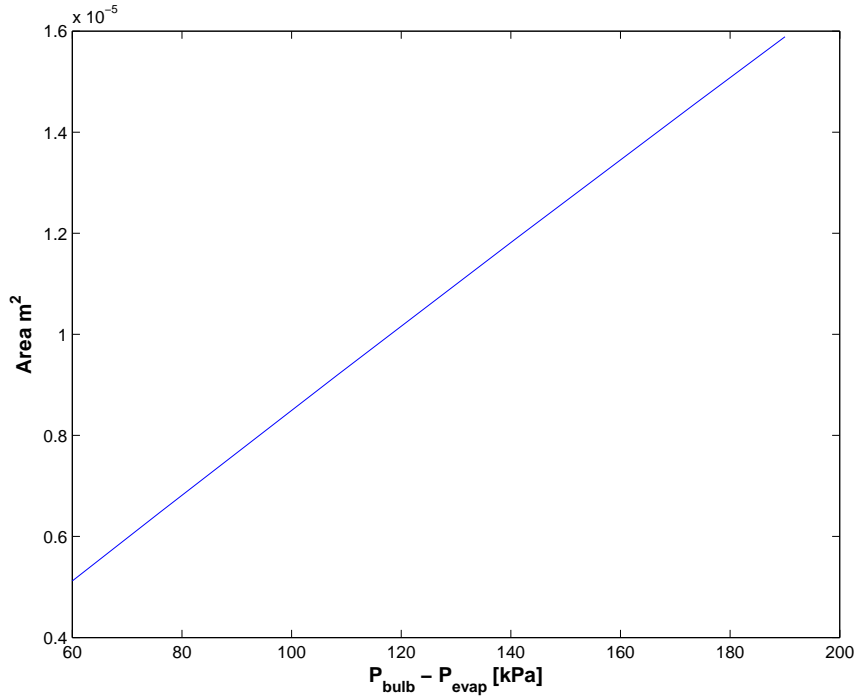


Figure 3.15 TEV area map

3.2.1.3 Mapping Procedure for Fixed Area Expansion Devices

Capillary tubes and orifice tubes are fixed area expansion devices. If the valve area is known, the discharge coefficient can be calculated from Equation 3.15. If the valve area is unknown, the flow coefficient is used as with the other valve models. In either case, the performance map is a function of the pressure differential across the expansion device.

$$C_{d,f} = f(\Delta P) \quad (3.19)$$

Sample code for generating a capillary/orifice tube performance map is found in Appendix A for the unknown area case. Figure 3.16 below shows an example of a capillary tube flow coefficient map.

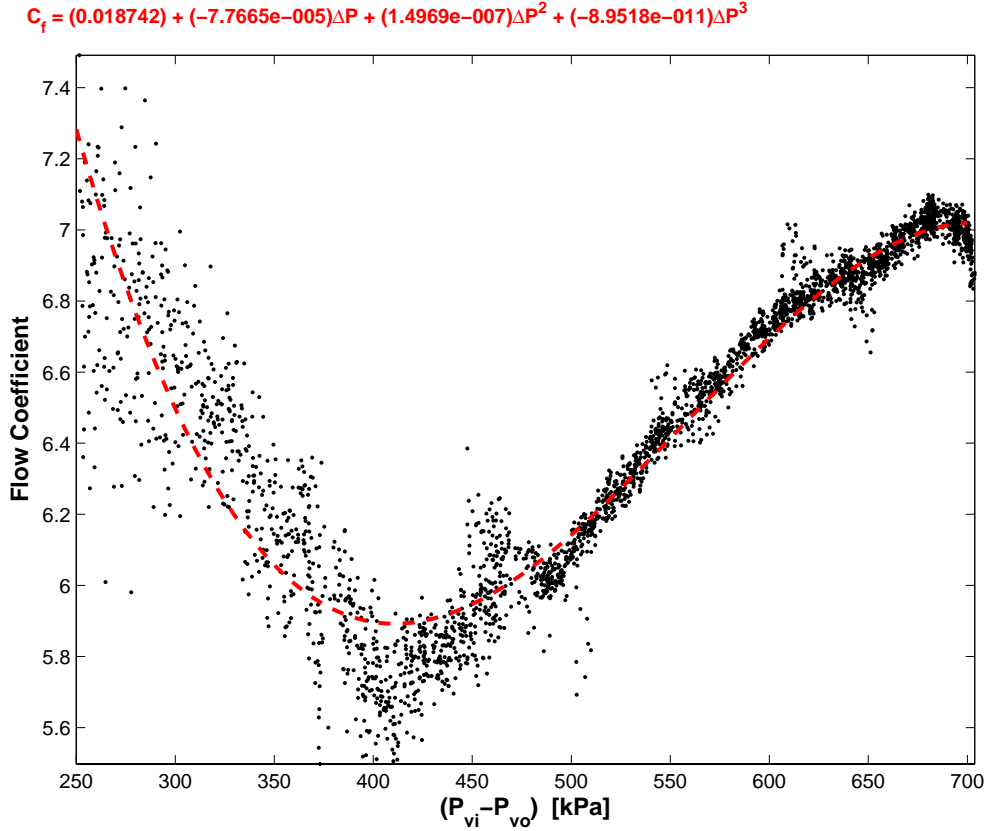


Figure 3.16 Capillary tube flow coefficient data points and best fit performance map

3.2.2 Compressor

The Thermosys compressor model provides a mass flow rate for the evaporator outlet and a mass flow rate and enthalpy for the condenser inlet. As with the expansion devices, the compressor is generally considered to be a static component. The compressor mass flow rate is modeled by Equation 3.20, where V_k is the compressor displacement volume per revolution, ω_k is the compressor speed, ρ_k is the inlet density, and η_{vol} is the compressor volumetric efficiency.

$$\dot{m}_k = V_k \omega_k \rho_k \eta_{vol} \quad (3.20)$$

The outlet enthalpy is based on an adiabatic efficiency, as shown in Equation 3.21, where $h_{out, isentropic}$ is the outlet enthalpy assuming isentropic compression, h_{in} is the inlet enthalpy, and η_a is the compressor adiabatic efficiency.

$$h_{out} = \frac{1}{\eta_a} [h_{out, isentropic} + h_{in} (\eta_a - 1)] \quad (3.21)$$

Determining the volumetric and adiabatic efficiency is the main challenge of compressor modeling. The flexible performance map approach is again applied to find the best model over a large range of operating conditions.

3.2.2.1 Mapping Procedure for Volumetric Efficiency

Equation 3.20 may be solved for volumetric efficiency. Given steady-state measurements of mass flow rate and inlet density, Equation 3.22 allows for the calculation of volumetric efficiency values. The steady-state measurements should cover the expected range of high side and low side pressures for the system.

$$\eta_{vol} = \frac{\dot{m}_k}{V_k \omega_k \rho_k} \quad (3.22)$$

Thermosys contains two-input and three-input performance map compressor models. In the two-input model, the volumetric efficiency is a function of the pressure ratio across the compressor and the compressor speed, as shown in Equation 3.23. The volumetric efficiency of the three-input model is assumed to be a function of the compressor speed, the inlet pressure, and the outlet pressure, as shown in Equation 3.24. Sample code for the creation of a three-input volumetric efficiency map is found in Appendix A. The three input performance map cannot be visualized, but a two input map with generating data is shown in Figure 3.17.

$$\eta_{vol} = f(P_r, \omega_k) \quad (3.23)$$

$$\eta_{vol} = f(\omega_k, P_{in}, P_{out}) \quad (3.24)$$

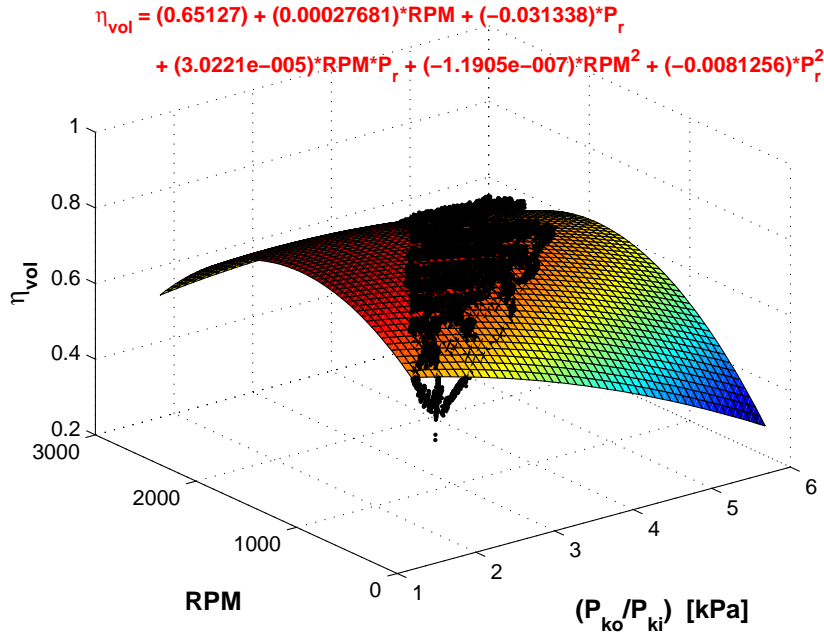


Figure 3.17 A two input performance map of volumetric efficiency

3.2.2.2 Mapping Procedure for Adiabatic Efficiency

Equation 3.21 may be solved for adiabatic efficiency to obtain Equation 3.25.

$$\eta_a = \frac{h_{out, isentropic} - h_{in}}{h_{out} - h_{in}} \quad (3.25)$$

Using steady-state measurements of inlet enthalpy, outlet enthalpy, and the calculated isentropic outlet enthalpy, this equation provides a means for calculating adiabatic efficiency values. As with the volumetric efficiency, the

adiabatic efficiency may be modeled with either two inputs or three inputs to the performance map. The adiabatic efficiency maps have the same inputs as the volumetric efficiency maps.

$$\eta_a = f(P_r, \omega_k) \quad (3.26)$$

$$\eta_a = f(\omega_k, P_{in}, P_{out}) \quad (3.27)$$

Code for generating a steady-state adiabatic efficiency map is found in Appendix A. A two input adiabatic efficiency map is shown in Figure 3.18.

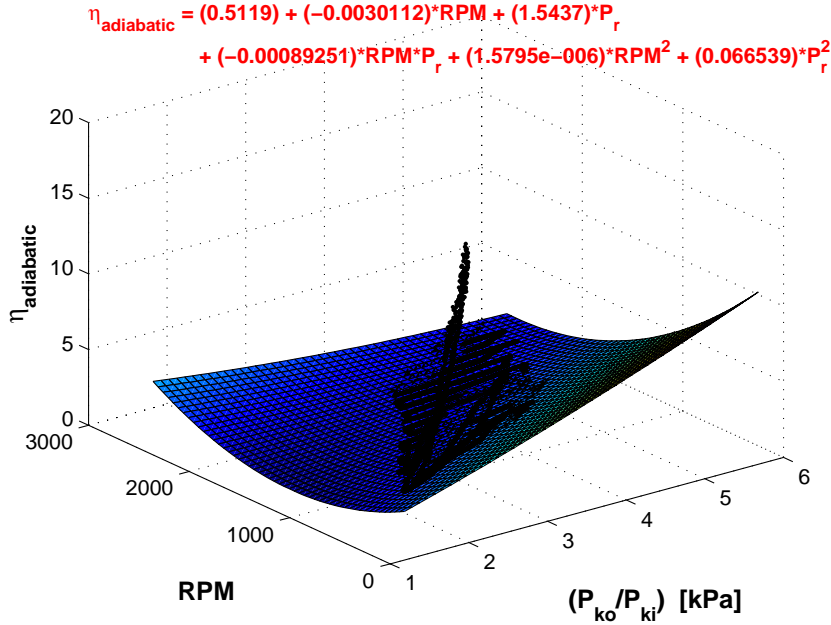


Figure 3.18 A two-input adiabatic efficiency map with experimental data

3.2.3 Implementation in Thermosys

Valve and compressor performance maps are implemented in Thermosys using the MATLAB lookup table interpolation functions “interp2” and “interp3” in code and the 2-D and n-D lookup table blocks (for $n = 3$) in Simulink. Each map input requires a vector of index values. For two input maps, the flow coefficient, discharge coefficient, volumetric efficiency, or adiabatic efficiency values are stored in a matrix. For three input maps, the coefficients and efficiencies are stored in a three dimensional array.

Examples of correctly formatted interpolation commands are shown in the following lines of code:

```
Cd=interp2(U_Vector,dP_Vector,Cd_matrix',U,dP);
```

```
Cd=interp3(Pin_Vector,U_Vector,Pout_Vector,Cd_matrix,Pin,U,Pout);
```

Figure 3.19 shows a 2-D lookup table block and its associated Block Parameters interface, while Figure 3.20 shows a 3-D lookup table block and its Block Parameters interface. It is important to note that the order of inputs for the interp3 function and the 3-D lookup table block is different.

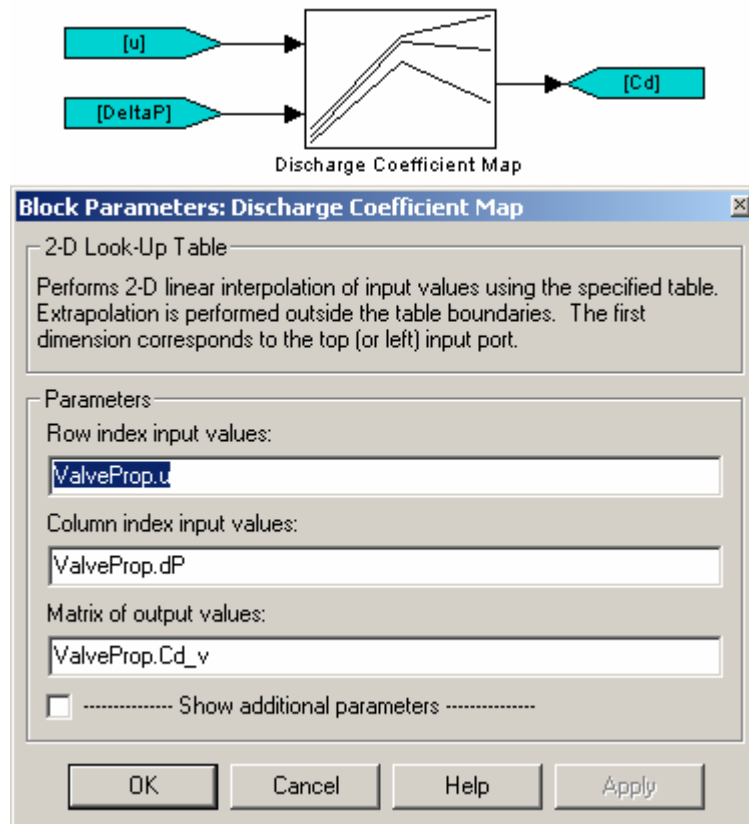


Figure 3.19 2-D lookup table block and Block Parameters interface

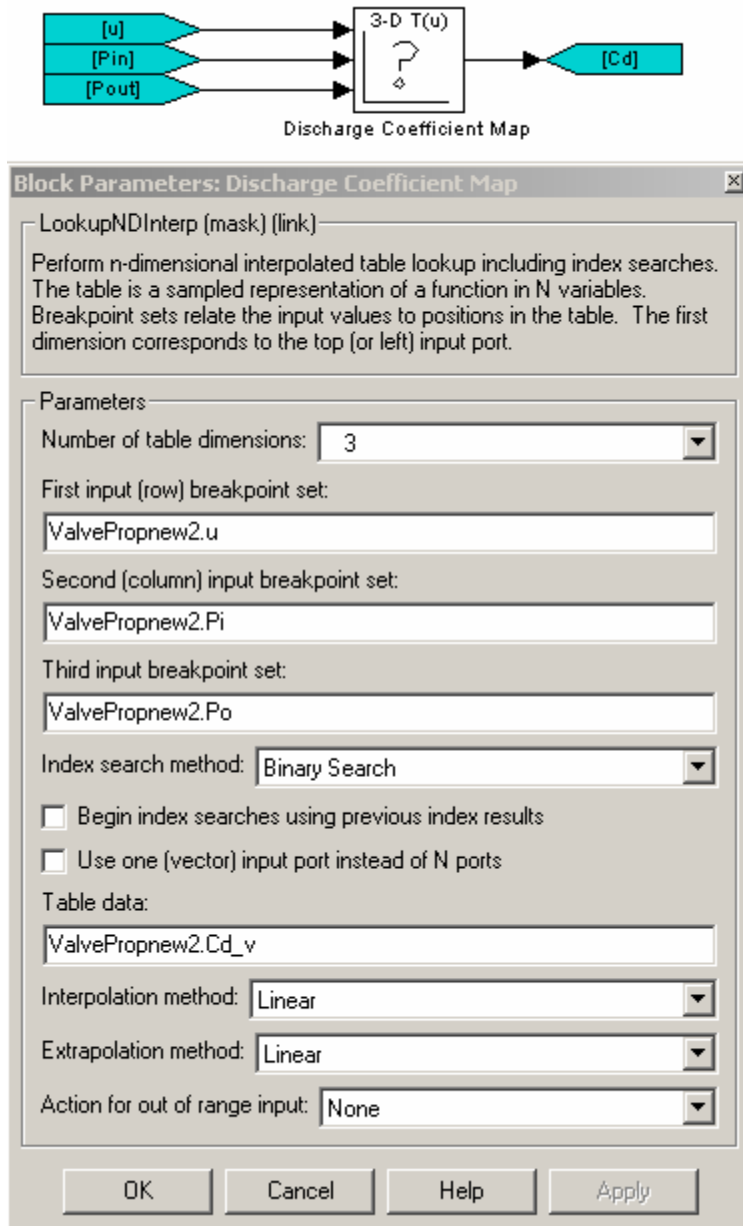


Figure 3.20 3-D lookup table block and Block Parameters interface

Flow coefficients, efficiencies, and input index vectors are stored in MATLAB data structures. For use in simulation, the data structures are first loaded into the MATLAB workspace. Then the appropriate data structure field names are entered in the component GUI, as shown in Figure 3.21 below. The GIU m-file loads the field names into the Block Parameters interface of the blocks in the Simulink model.

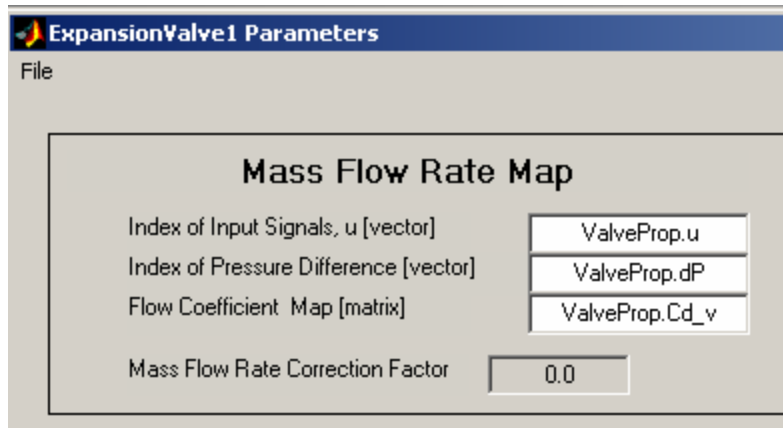


Figure 3.21 Performance map portion of the 2-input EEV component GUI showing data structure field names

Chapter 4. Atmospheric Conditions Modeling

Original Thermosys heat exchanger air-side mass and energy balances assumed dry air entering the heat exchangers. This chapter details the model modifications necessary to take into account the effects of the water vapor which is nearly always present to some degree in atmospheric air. Two modeling approaches are presented. The first approach is based on condensation occurring when the bulk air temperature reaches the dew point. The second approach assumes that condensation begins when the heat exchanger wall temperature reaches the dew point. The mass and energy balances follow from the discussion in [7].

Some equations appearing in the derivations represent fluid property functions. Due to the complex nature of the functions, they are not given explicitly in this thesis. For simulation purposes, the fluid property functions are implemented as lookup tables in Thermosys. The data contained in the tables was generated from the fluid property functions provided with the software package Engineering Equation Solver (EES) [29]. The EES documentation contains the details of the specific equations of state used for the various fluid properties. Plots for two common fluid properties, saturation pressure as a function of saturation temperature and saturated liquid enthalpy as a function of temperature, are shown in Figure 4.1 and Figure 4.2.

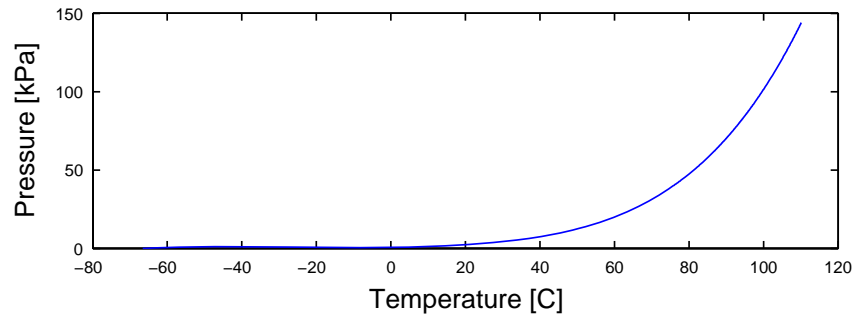


Figure 4.1 Water saturation pressure as a function of saturation temperature

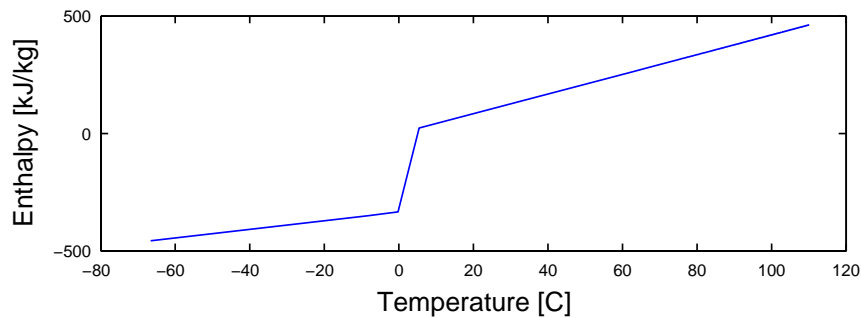


Figure 4.2 Water saturated liquid enthalpy as a function of temperature

4.1 Air Temperature Condensation Method

The air temperature condensation method assumes that condensation occurs when the bulk average air temperature is lower than the dew point. This highly idealized model does not take into account the spatial variation of air temperatures around the heat exchanger.

4.1.1 Modified Energy Balances

To properly model air-side behavior, mass and energy balances should take into account both air and water vapor entering the evaporator. Two distinct situations are possible. Water vapor may pass through the evaporator either with or without some condensation on the surface of the evaporator. The two conditions require different mass and energy balances. The non-condensing equations are presented first.

4.1.1.1 Non-condensing Conditions

Figure 4.3 shows a control volume containing the air around an evaporator. Air enters and exits the control volume at a known rate, \dot{m}_{air} . The inlet temperature, inlet enthalpy, and inlet relative humidity of the air are known quantities. Heat is transferred from the air to the evaporator wall. The variables to be determined are the outlet temperature, the outlet enthalpy, and the outlet relative humidity of the air. We assume that no condensation occurs and that the outlet relative humidity is less than one. The conservation of mass is given in Equation 4.1. The conservation of energy is given in Equation 4.2.

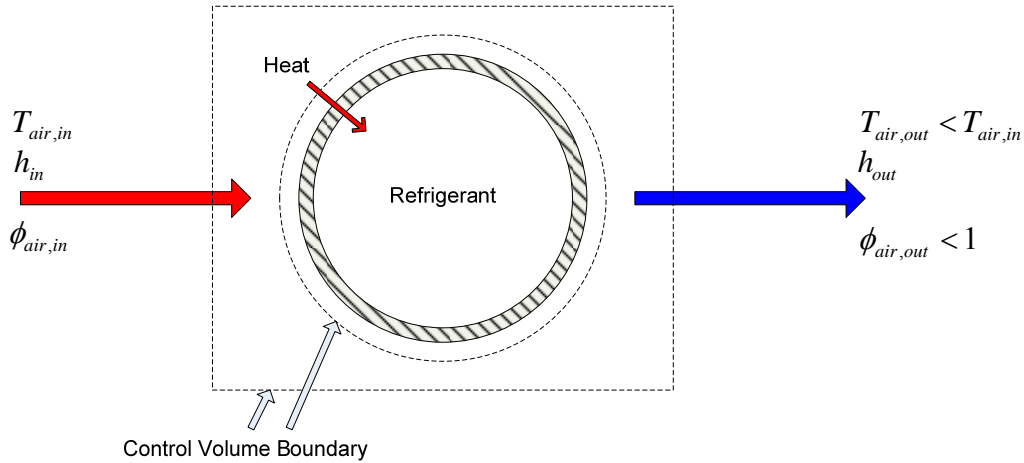


Figure 4.3 Control volume for humid air mass and energy balances under non-condensing conditions

$$\dot{m}_{air,in} = \dot{m}_{air,out} \quad (4.1)$$

$$\dot{Q}_{wall,in} = \dot{m}_{air}(h_{in} - h_{out}) \quad (4.2)$$

The inlet enthalpy is a combination of the dry air enthalpy and the enthalpy of water vapor in the air, as shown in Equation 4.3. A constant specific heat assumption results in errors less than 0.2 percent between -10 and 50°C. The inlet absolute humidity is calculated from Equation 4.4. The enthalpy of the water vapor (in kJ/kg) is approximated with Equation 4.5. The approximation error is again insignificant between -10 and 50°C. The inlet saturation pressure of water is a function of the inlet air temperature, as shown in Equation 4.6. Thus, with knowledge of $T_{air,in}$ and the ambient air pressure, the enthalpy of the air entering the control volume may be determined.

$$h_{in} = C_{p,air}T_{air,in} + \omega_{in}h_{g,in} \quad (4.3)$$

$$\omega_{in} = \frac{0.622\phi_{in}P_{g,in}}{P_{air} - \phi_{in}P_{g,in}} \quad (4.4)$$

$$h_{g,in} = 2501.3 + 1.82T_{air,in} \quad (4.5)$$

$$P_{g,in} = P_{sat}(T_{air,in}) \quad (4.6)$$

The outlet enthalpy is calculated from the energy balance for air, as shown in Equation 4.7. The heat transfer rate from the air to the evaporator is assumed to be a known quantity. As with the inlet air, the enthalpy of the outlet air is found from the dry air enthalpy and the water vapor enthalpy. Recognizing that the non-condensation condition implies that the inlet and outlet absolute humidity are equivalent, Equation 4.8 is obtained for the outlet enthalpy. Substituting the water vapor enthalpy approximation yields Equation 4.9. Solving for the outlet air temperature gives Equation 4.10.

$$h_{out} = h_{in} - \frac{\dot{Q}_{wall,in}}{\dot{m}_{air}} \quad (4.7)$$

$$h_{out} = C_{p,air}T_{air,out} + \omega_{in}h_{g,out} \quad (4.8)$$

$$h_{out} = C_{p,air}T_{air,out} + \omega_{in}(2501.3 + 1.82T_{air,out}) \quad (4.9)$$

$$T_{air,out} = \frac{h_{out} - 2501.3\omega_{in}}{C_{p,air} + 1.82\omega_{in}} \quad (4.10)$$

The outlet saturation pressure is a function of the outlet air temperature, as in Equation 4.11. Using this pressure, the outlet relative humidity is found from Equation 4.12.

$$P_{g,out} = P_{sat}(T_{air,out}) \quad (4.11)$$

$$\phi_{out} = \frac{\omega_{in}P_{air}}{P_{g,out}(0.622 + \omega_{in})} \quad (4.12)$$

Equations 4.7, 4.10, and 4.12 give the three outlet variables of interest. As a final step, the outlet air temperature is compared to the dew point temperature to verify that the non-condensation assumption is correct. The dew point is the saturation temperature of water at the water vapor partial pressure. The water vapor partial pressure is given in Equation 4.13. The dew point is then a function of the partial pressure, as shown in Equation 4.14. If the outlet air temperature is above the dew point, the non-condensation assumption is correct.

$$P_v = \phi_{in}P_{g,in} \quad (4.13)$$

$$T_{dp} = T_{sat}(P_v) \quad (4.14)$$

4.1.1.2 Condensing Conditions

Figure 4.4 shows a control volume for humid air under condensing conditions. The two major differences between this control volume and the non-condensing conditions control volume are the saturated air outlet condition and the presence of liquid water leaving the control volume. The liquid water is assumed to have the same temperature as the outlet air. The conservation of mass equation for the air is given in Equation 4.1. The conservation of mass for water is given in Equation 4.15, and the conservation of energy is found in Equation 4.16.

The variables to be determined are the outlet air temperature, the outlet enthalpy, and the liquid water mass flow rate.

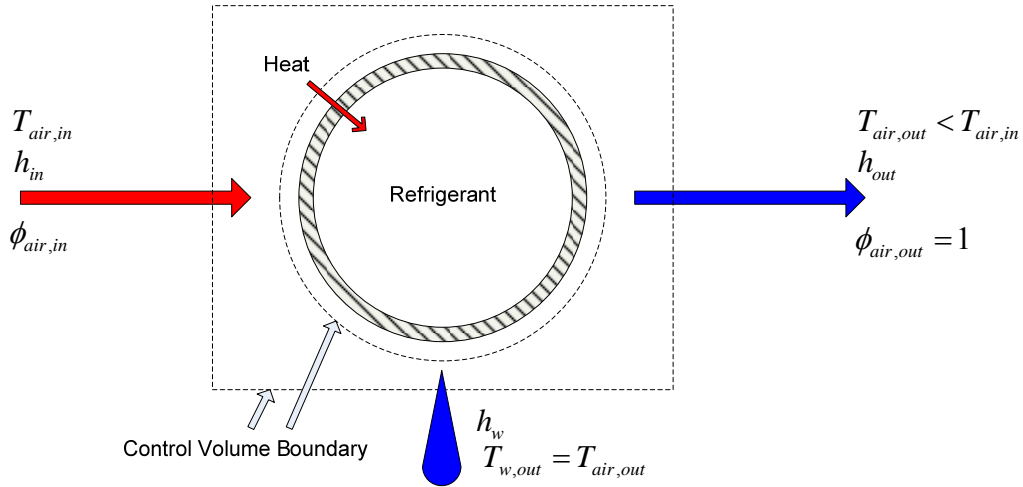


Figure 4.4 Control volume for humid air mass and energy balances under condensing conditions

$$\dot{m}_{air} \omega_{in} = \dot{m}_{air} \omega_{out} + \dot{m}_w \quad (4.15)$$

$$\dot{Q} = \dot{m}_{air} (h_{in} - h_{out}) - \dot{m}_w h_w \quad (4.16)$$

Unlike the non-condensing conditions equations, Equations 4.15 and 4.16 cannot be solved explicitly for the outlet air temperature and humidity. Instead, an outlet air temperature is assumed, and an iterative solution approach is applied. The inlet enthalpy is found from Equation 4.3 through Equation 4.6 above. Using the assumed outlet air temperature, the outlet saturation pressure is found from Equation 4.17. The inlet absolute humidity is found from Equation 4.4. Assuming saturated outlet conditions ($\phi_{out} = 1$), the outlet absolute humidity is found from Equation 4.18. Equation 4.19 gives the outlet enthalpy. The mass flow rate of liquid water leaving the control volume is given by Equation 4.20. The liquid water enthalpy is also found from the assumed outlet air temperature, as shown in Equation 4.21.

$$P_{g,out} = P_{sat}(T_{air,out}) \quad (4.17)$$

$$\omega_{out} = \frac{0.622 P_{g,out}}{P_{air} - P_{g,out}} \quad (4.18)$$

$$h_{out} = C_{p,air} T_{air,out} + \omega_{out} h_{g,out} \quad (4.19)$$

$$\dot{m}_w = \dot{m}_{air} (\omega_{in} - \omega_{out}) \quad (4.20)$$

$$h_w = h_f(T_{air,out}) \quad (4.21)$$

The variables found from the above equations are substituted into the energy balance equation, Equation 4.16, to check the validity of the assumed outlet air temperature. If the energy balance is not satisfied within a given tolerance, a new outlet air temperature is assumed and the calculations are repeated. Once the correct outlet air temperature is found, a check of the condensing conditions assumption is carried out with Equation 4.13 and Equation 4.14. If the outlet air temperature is below the dew point, the condensing conditions assumption is correct.

4.1.2 Heat Transfer Rates

4.1.2.1 Non-condensing Conditions

The equation for $\dot{Q}_{wall,in}$ is dependent on the presence or absence of condensation. Under non-condensing conditions, the heat transfer rate to the heat exchanger wall is found from Equation 4.22, where α_o is the air-side heat transfer coefficient, A_o is the external heat exchanger area, T_a is the average air temperature, and T_w is the lumped wall temperature.

$$\dot{Q}_{wall,in} = \alpha_o A_o (T_a - T_w) \quad (4.22)$$

4.1.2.2 Condensing Conditions

If condensation is occurring, the original heat transfer equation, Equation 4.22, must be modified to account for the energy released by the phase change of water from a vapor to a liquid. The result is Equation 4.23. The latent heat, h_{fg} , is found at the average air temperature, T_a .

$$\dot{Q}_{wall,in} = \alpha_o A_o (T_a - T_w) + \dot{m}_w h_{fg} \quad (4.23)$$

4.1.2.3 Wet Conditions Heat Transfer Coefficients

The presence of water droplets or a film of water on the evaporator changes the air-side heat transfer characteristics. Korte and Jacobi (2001) [30] studied plain fin heat exchangers under wet conditions. They found that there were clear trends when comparing dry and wet j factor data, but the differences were almost within the experimental uncertainty. Mirth and Ramadhyani [35] studied wavy fin heat exchangers. They found that the effect of condensation on the air-side heat transfer coefficient was unclear. Sometimes the wet surface heat transfer coefficients were higher than the dry surface coefficients. Sometimes the relationship was reversed. The authors claimed to demonstrate that “it is possible to predict heat transfer rates under a wide range of wet-surface conditions with good accuracy using only dry-surface heat transfer correlations.” Based on the findings of these researchers, adjustments to heat transfer coefficients under wet conditions are not included in the Thermosys model.

4.1.3 Implementation in Thermosys

The humid air functionality requires the user to supply the model with the inlet air temperature and the inlet relative humidity at the initial condition and at each subsequent time step. In addition, the user must supply an initial condition for the outlet air temperature. The ambient air pressure and the specific heat of air are assumed to be constants. The evaporator with humid air is implemented in a new, and as yet unreleased, version of Thermosys referred to as Thermosys Academic. In Thermosys Academic, the component models are based on MATLAB functions rather than Simulink block diagrams. This shift to code-based component models facilitates the incorporation of new, more complex models such as the evaporator with humid air.

The humid air outlet conditions solution is divided into two sections of code, a non-condensing section and a condensing section. The two sections are contained within a while loop. When one of the two sections successfully finds an outlet air temperature and verifies the condensing or non-condensing assumption, a flag is set to force an exit from the while loop. The code also sets a flag that indicates which assumption (non-condensing or condensing) to try first on the next iteration. For instance, if the current time step finds condensing conditions, the next time step will execute the condensing section first.

The iterative solution of the condensing conditions energy balance is carried out with the `fmincon` function, part of the Control Systems Toolbox. The initial guess for the outlet air temperature is the outlet air temperature found from the previous time step. The energy balance equation, Equation 4.24, is found by combining Equation 4.16 and Equation 4.23. The objective function for the minimization, Equation 4.25, is found by squaring the left side of Equation 4.24.

$$\dot{m}_a(h_{in} - h_{out}) - \dot{m}_w(h_w + h_{fg}) - \alpha_o A_o (T_a - T_w) = 0 \quad (4.24)$$

$$F = (\dot{m}_a(h_{in} - h_{out}) - \dot{m}_w(h_w + h_{fg}) - \alpha_o A_o (T_a - T_w))^2 \quad (4.25)$$

The iterative approach to solving the condensing conditions energy balances and to determining the condensing condition does not produce a noticeable slow-down in simulation speed.

4.2 Wall Temperature Condensation Method

Initial validation of the air temperature condensation method revealed that condensation occurred on the experimental evaporator when the outlet air temperature, and therefore the bulk average air temperature, was above the dew point. For example, the plot in Figure 4.5 shows dew point and outlet air temperature data for a test during which condensation was observed in the evaporator.

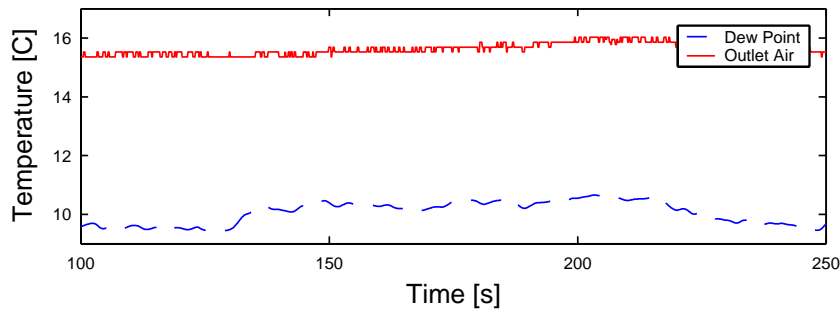


Figure 4.5 Data for a condensing conditions test with the air temperature well above the dew point temperature

This observation indicated that significant spatial air temperature variations were present in the heat exchanger. For this condition, which is common in compact heat exchangers, the air temperature condensation model is inadequate because it will not accurately predict the onset of condensing conditions. To address this inadequacy, an evaporator model was created that assumes a condensing condition when the heat exchanger wall temperature is less than the dew point. In this model, a mass transfer coefficient is used to determine the condensate mass flow rate. In addition, the model incorporates a higher level of detail by considering condensation in the different fluid regions of the evaporator. The general control volumes are the same as those used in the previous derivation, but they are separated by region, as shown in Figure 4.6. The control volume boundaries contain the air surrounding the heat exchanger and are only used for derivation purposes.

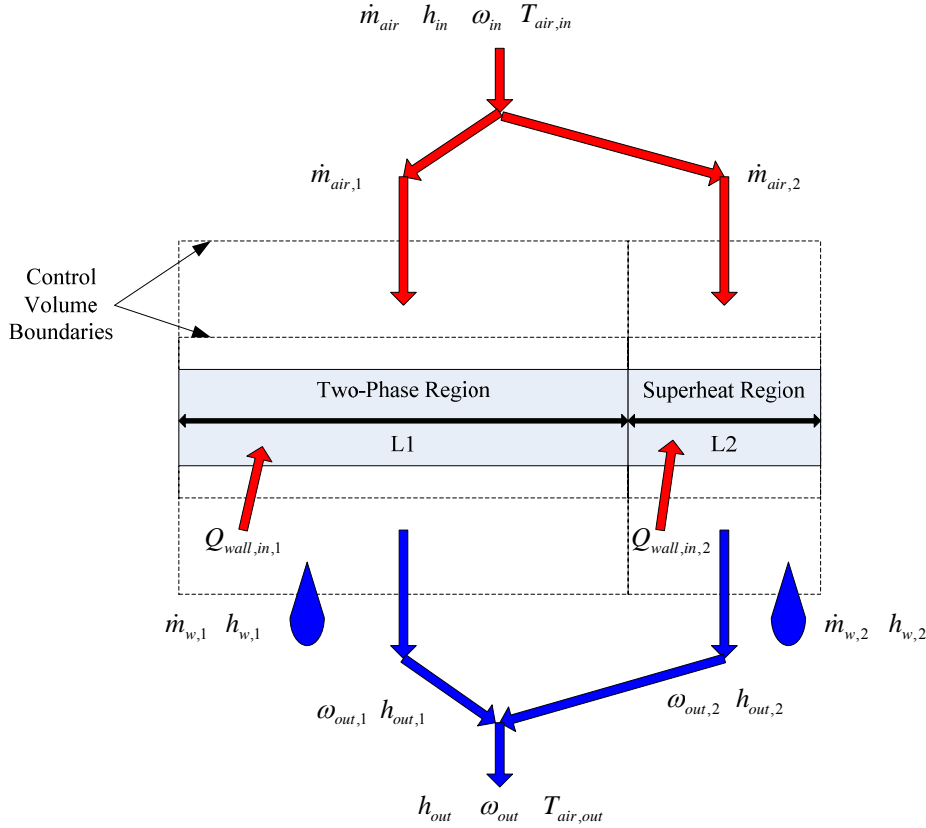


Figure 4.6 Divided air-side control volumes

4.2.1 Individual Region Mass and Energy Balances

As with the previous modeling approach, the model outputs of interest are the heat exchanger outlet air temperature and outlet relative humidity, which are obtained from the outlet enthalpy and the outlet absolute humidity. The outlet enthalpy in each region is found by rearranging the energy balance equation, Equation 4.16. This equation was previously used only for condensing conditions, but in this derivation it will be taken as a general energy balance for both condensing and non-condensing conditions. The equation for outlet enthalpy is given in Equation 4.26, where numeric subscripts denote individual fluid regions. The mass balance relations are given in Equation 4.27 through Equation 4.29. The derivation assumes an evaporator with a two-phase region (1) and a superheat region (2). Adding additional fluid regions to the derivation is trivial.

$$h_{out,1,2} = h_{in} - \frac{\dot{m}_{w,1,2}}{\dot{m}_{air,1,2}} h_{w,1,2} - \frac{\dot{Q}_{wall,in,1,2}}{\dot{m}_{air,1,2}} \quad (4.26)$$

$$\dot{m}_{air,1} = \dot{m}_{air,1,in} = \dot{m}_{air,1,out} \quad (4.27)$$

$$\dot{m}_{air,2} = \dot{m}_{air,2,in} = \dot{m}_{air,2,out} \quad (4.28)$$

$$\dot{m}_{air} = \dot{m}_{air,1} + \dot{m}_{air,2} \quad (4.29)$$

Solution of Equation 4.26 requires an air mass flow rate across each region. The overall air mass flow rate is divided into two parts based on the length of each region, as shown in Equation 4.30 and Equation 4.31.

$$\dot{m}_{air,1} = \frac{L_1}{L_{Total}} \dot{m}_{air} \quad (4.30)$$

$$\dot{m}_{air,2} = \frac{L_2}{L_{Total}} \dot{m}_{air} \quad (4.31)$$

The heat transfer rates, $\dot{Q}_{wall,in}$, are found in the manner previously described for the air temperature condensation method derivation. Other key variables in Equation 4.26 are the mass flow rates of condensate leaving the control volume. These mass flow rates are found from Equation 4.32. The determination of the outlet absolute humidity terms is discussed in the following section.

$$\dot{m}_{w,1,2} = \dot{m}_{air,1,2} (\omega_{out,1,2} - \omega_{in}) \quad (4.32)$$

4.2.2 Outlet Humidity Calculations

Equation 4.33 provides a relationship between the outlet absolute humidity and the air mass flow rate in each region. The left hand side of Equation 4.33 gives the condensate mass flow rate based on the change in inlet and outlet absolute humidity. The right hand side of Equation 4.33 gives the condensate mass flow rate based on a mass transfer coefficient, a fin efficiency, and a log mean humidity difference. The log mean humidity difference approach is taken from [34].

$$\dot{m}_{air,1,2} (\omega_{out,1,2} - \omega_{in}) = \alpha_m A_{o,1,2} \eta_o \left(\frac{(\omega_{in} - \omega_{wall,1,2}) - (\omega_{out} - \omega_{wall,1,2})}{\ln \left(\frac{\omega_{in} - \omega_{out,1,2}}{\omega_{out,1,2} - \omega_{wall,1,2}} \right)} \right) \quad (4.33)$$

Solving for the outlet absolute humidity yields Equation 4.34.

$$\omega_{out,1,2} = \frac{\omega_{in} - \omega_{wall,1,2}}{e^{\left(\frac{\alpha_m A_{o,1,2} \eta_o}{\dot{m}_{air,1,2}} \right)}} + \omega_{wall,1,2} \quad (4.34)$$

Under condensing conditions, the absolute humidity at the wall, ω_{wall} , is the absolute humidity of saturated water at the wall temperature. The humidity is assumed to be uniform around the tube. The external heat transfer area, A_o , and the inlet absolute humidity, ω_{in} , are known parameters.

The amount of mass transfer is governed by the mass transfer coefficient, α_m . The mass transfer coefficient is often assumed to be a function of the heat transfer coefficient [13]. Equation 4.35 for the mass transfer coefficient assumes a Lewis number of one.

$$\alpha_m = \frac{\alpha_o}{\rho_{air} C_{p,air}} \quad (4.35)$$

The specific heat of dry air is taken to be a constant at 1.005 kJ/kg-K, and the air density is considered to be a function of temperature according to the ideal gas law.

The general expression for the overall surface effectiveness is given in Equation 4.36.

$$\eta_o = 1 - \frac{A_{fin}}{A_o} (1 - \eta_{fin}) \quad (4.36)$$

The fin efficiency parameter, η_{fin} , in Equation 4.36 requires detailed analysis of the heat exchanger geometry. The following discussion is specific to wavy-fin heat exchangers similar to that of the experimental system and is taken from [46]. Other heat exchanger geometries require different expressions for the fin efficiency. The wavy-fin efficiency is calculated from Equation 4.37.

$$\eta_{fin} = \frac{\tanh(mr\theta)}{mr\theta} \quad (4.37)$$

The parameter m is defined in Equation 4.38, and the parameter θ is defined in Equation 4.39.

$$m = \sqrt{\frac{2\alpha_o}{k_{fin}\delta_{fin}}} \quad (4.38)$$

$$\theta = \left(\frac{R_{eq}}{r} - 1 \right) \left[1 + 0.35 \ln \left(\frac{R_{eq}}{r} \right) \right] \quad (4.39)$$

In Equation 4.38, k_{fin} is the fin material conductivity and δ_{fin} is the fin thickness. The equivalent radius parameter is given in Equation 4.40, where r is the tube inside radius which is also used in Equation 4.37.

$$R_{eq} = 1.27 X_M \left(\frac{X_L}{X_M} - 0.3 \right)^{0.5} \quad (4.40)$$

Equation 4.40 contains two additional geometric parameters, X_M and X_L , which are defined in Equation 4.41 and Equation 4.42. The parameters P_t and P_l are the transverse and longitudinal tube pitches, respectively.

$$X_M = \frac{P_t}{2} \quad (4.41)$$

$$X_L = \sqrt{\left(\frac{P_t}{2} \right)^2 + \frac{P_l^2}{2}} \quad (4.42)$$

4.2.3 Mixing of Region Outputs

Once the humidity and enthalpy outputs from each region have been determined, a single lumped outlet condition is found. Equation 4.43 for the adiabatic mixing of airstreams [7] relates the air mass flow rates and the outlet conditions of each region to the mixed outlet conditions.

$$\frac{\dot{m}_{air,1}}{\dot{m}_{air,2}} = \frac{\omega_{out,2} - \omega_{wout}}{\omega_{out} - \omega_{out,1}} = \frac{h_{out,2} - h_{out}}{h_{out} - h_{out,1}} \quad (4.43)$$

Solving for the mixed outlet enthalpy yields Equation 4.44, while solving for the mixed outlet absolute humidity gives Equation 4.45.

$$h_{out} = \frac{h_{out,2} + h_{out,1} \left(\frac{\dot{m}_{air,1}}{\dot{m}_{air,2}} \right)}{1 + \frac{\dot{m}_{air,1}}{\dot{m}_{air,2}}} \quad (4.44)$$

$$\omega_{out} = \frac{\omega_{out,2} + \omega_{out,1} \left(\frac{\dot{m}_{air,1}}{\dot{m}_{air,2}} \right)}{1 + \frac{\dot{m}_{air,1}}{\dot{m}_{air,2}}} \quad (4.45)$$

The outlet air temperature is found from Equation 4.46 as a function of both the mixed enthalpy and absolute humidity. The outlet relative humidity is found from Equation 4.47, where $P_{g,out}$ was given in Equation 4.11. Finally, the total condensate mass flow rate is the sum of the condensate mass flow rate found for each region, as shown in Equation 4.48.

$$T_{air,out} = \frac{h_{out} - 2501.3\omega_{out}}{C_{p,air} + 1.82\omega_{out}} \quad (4.46)$$

$$\phi_{out} = \frac{\omega_{out} P_{air}}{(0.622 + \omega_{out}) P_{g,out}} \quad (4.47)$$

$$\dot{m}_w = \dot{m}_{w,1} + \dot{m}_{w,2} \quad (4.48)$$

4.2.4 Implementation in Thermosys

The general implementation is similar to that described previously for the air temperature condensation model. The model inputs are the same, and the wall temperature condensation model is also implemented as a MATLAB function.

The code that calculates air-side outlet conditions is divided into two sections, one for each fluid region. The condensation condition in each region is first determined by checking the region wall temperature. If the wall temperature is above the dew point, the region absolute outlet humidity is set equal to the inlet absolute humidity and the region condensate mass flow rate is set to zero. The outlet condition is then found from Equation 4.26. If the wall temperature is below the dew point, the region outlet absolute humidity is determined from Equation 4.34. The condensate mass flow rate is found from Equation 4.32. Finally, the outlet enthalpy is again found from Equation 4.26. Once the outlet conditions of each region have been determined, the lumped outlet enthalpy and absolute humidity are found from Equation 4.44 and Equation 4.45. The outputs of interest, outlet air temperature, outlet relative humidity, and condensate mass flow rate, are then calculated with Equation 4.46 through Equation 4.48. Unlike the air temperature condensation method, an iterative solution procedure is not required for the condensing conditions case.

Chapter 5. Dynamic Modeling

5.1 Motivation

The overall motivation for the developments described in this chapter is to improve the accuracy and applicability of the Thermosys models through dynamic modeling techniques. Both first-principles and system identification modeling techniques are applied, depending on the situation. The first-principles approach is applied when the underlying physics is well understood, while the system identification approach is applied when the appropriate model structure is unknown or overly complex. This chapter also examines possible future extensions to dynamic simulation capabilities with emphasis on compressor cycling simulation.

5.1.1 Heat exchangers with Receivers/Accumulators

Heat exchangers with receivers/accumulators are found in the majority of VCC systems. These critical components were not included in previous distributions of Thermosys, severely limiting the types of systems and operating conditions that could be modeled. While the modeling of these components is challenging in the moving-boundary framework, employing a first-principles dynamic modeling approach gives the model developer the ability to apply assumptions in the derivation process that allow the models to run under varying fluid phase outlet conditions without using a model switching scheme. The new components are a necessary addition to Thermosys, allowing for simulation of a large range of common systems and operating conditions.

5.1.2 Compressor Shell Capacitance

The dynamic effects of the compressor shell thermal capacitance were not included in the original compressor model. Early validation results revealed that the static compressor outlet enthalpy model output did not match the experimental data. The static outlet enthalpy performance map accurately predicted the correct enthalpy for a given operating condition, but it could not account for the transients associated with transitions between operating conditions. A first-order dynamic model with a user-specified time constant was chosen as a means for capturing the dynamic effects of the compressor shell thermal capacitance and slowing the response speed of the model.

5.1.3 Dynamic Mass Flow Correction

Model validation results also suggested that the inaccurate prediction of the compressor mass flow rate was causing large errors in evaporator pressure and other model outputs. The mass flow rate errors could be caused by inadequacy of the static compressor model or by unmodeled components and component interactions. The compressor dynamic behavior is not well understood because the experimental system cannot directly measure the compressor mass flow rate. Because the sources of the modeling errors are not well understood, a system identification approach was applied. A combination of model output and system data was used to find a dynamic compressor mass flow rate correction model.

5.1.4 Compressor Cycling Simulation

A common control practice, and likely direction for future research, is compressor cycling. An analysis of current compressor cycling simulation capabilities is presented. Compressor cycling drives models towards conditions that violate the assumptions used in deriving the moving-boundary models. The results presented here give comparisons of model output and system data to demonstrate that the models qualitatively capture system

behavior under compressor cycling conditions. The extent to which cycling conditions cause violations of the modeling assumptions is also examined.

5.2 Heat Exchangers with Receivers/Accumulators

The majority of VCC systems include a receiver or an accumulator. The receiver is connected to the condenser outlet and stores excess refrigerant charge. The accumulator is connected to the evaporator outlet and captures liquid phase refrigerant, preventing it from damaging the compressor. These two components ensure safe and reliable operation over a wide range of conditions. The nonlinear model derivations are presented in the following sections. Linear models of the same components are available in [41].

5.2.1 Challenge of Receiver/Accumulator Modeling

The main challenge presented by the presence of receivers/accumulators is the possibility of multiple fluid phase conditions at the heat exchanger outlet. At steady-state conditions, a condenser with receiver will operate with saturated liquid or two-phase fluid at the outlet, as shown in Figure 5.1. During transients, the condenser outlet fluid condition could deviate to subcooled outlet conditions, as shown in Figure 5.2. Similarly, an evaporator with accumulator will operate with saturated vapor or two-phase fluid at the outlet. Transients could cause the evaporator outlet fluid condition to deviate to superheated vapor conditions.

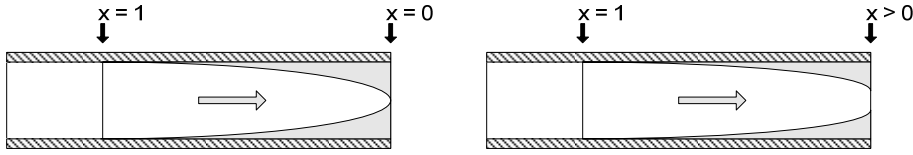


Figure 5.1 Two possible steady-state condenser with receiver operating conditions

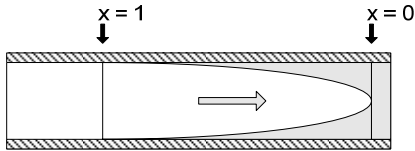


Figure 5.2 A possible transient condenser with receiver operating condition

The creation of a subcooled region in the condenser or a superheated region in the evaporator presents the problem of the creation of new dynamic states, as fluid region lengths and wall temperatures are states in the moving-boundary framework. When the system transients die out, the models face the problem of disappearing states. In the traditional moving-boundary framework, multiple model structures would be needed to capture the dynamics of heat exchangers operating with the possibility of multiple fluid phase conditions at the outlet. Previous work [11, 47] used a model switching approach to accommodate multiple modeling frameworks in one simulation. In the following heat exchanger derivations, an extended definition of quality is used to capture the transient behavior of heat exchangers with receivers/accumulators and avoid the complications of switching model structures during simulation.

5.2.2 Receiver Model

High side receivers provide a volume for storing excess refrigerant charge and ensuring liquid flow into the expansion device. The receiver is modeled as a simple control volume with refrigerant entering and exiting the

control volume boundary. Heat transfer may occur between the walls of the receiver and the surroundings. The entering refrigerant is either two-phase, saturated liquid, or subcooled, and the exiting refrigerant is assumed to be saturated liquid, as shown in Figure 5.3. The receiver pressure is assumed to be the condenser pressure.

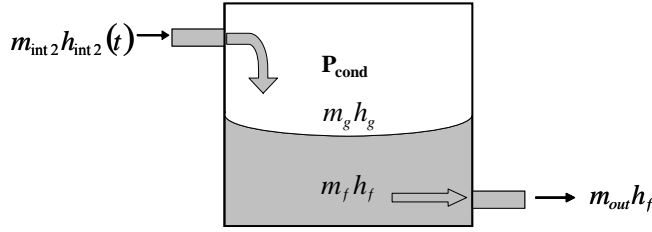


Figure 5.3 Control volume for receiver model

The conservation of mass and energy for the receiver are written as Equation 5.1 and Equation 5.2.

$$\frac{dm_{rec}}{dt} = \dot{m}_{in} - \dot{m}_{out} \quad (5.1)$$

$$\frac{d(m_{rec}u_{rec})}{dt} = \dot{m}_{in}h_{in} - \dot{m}_{out}h_{out} + UA(T_{amb} - T_{rec}) \quad (5.2)$$

Expanding the time derivative term of Equation 5.2 results in a conservation of refrigerant energy equation in terms of \dot{m}_{rec} and \dot{P}_{rec} . Thus Equation 5.1 and Equation 5.3 form the governing differential equations for the receiver.

$$\left[\left(\frac{d\rho_g}{dP_c} V_g u_g + \frac{d\rho_f}{dP_c} V_f u_f + \frac{du_g}{dP_c} \rho_g V_g + \frac{du_f}{dP_c} \rho_f V_f \right) - \left(\frac{\rho_g u_g - \rho_f u_f}{\rho_g - \rho_f} \right) \left(\frac{d\rho_g}{dP_c} V_g + \frac{d\rho_f}{dP_c} V_f \right) \right] \dot{P}_c + \left[\frac{\rho_g u_g - \rho_f u_f}{\rho_g - \rho_f} \right] \dot{m}_{rec} = \dot{m}_{int} h_{int} - \dot{m}_{out} h_{out} - UA_{rec} (T_{rec} - T_{amb}) \quad (5.3)$$

5.2.3 Accumulator Model

Low side accumulators protect compressors from “slugging” by capturing two-phase refrigerant and allowing only vapor to exit the accumulator and enter the compressor. The only difference between the accumulator model and the receiver model is the inlet and outlet conditions. For the accumulator, the entering refrigerant is either two-phase, saturated vapor, or superheated, and the exiting fluid is assumed to be saturated vapor, as shown in Figure 5.4. The accumulator pressure is assumed to be the evaporator pressure.

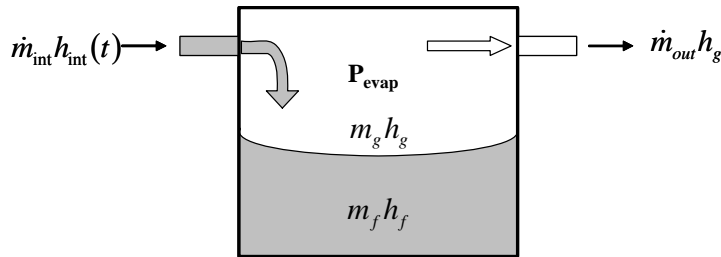


Figure 5.4 Control volume for accumulator model

The equations for the accumulator are obtained by replacing the receiver terms with accumulator terms and the condenser terms with evaporator terms in Equation 5.1 and Equation 5.3.

5.2.4 Nonlinear Condenser with Receiver

Nominally, the condenser is assumed to have two fluid regions (superheat and two-phase), as shown in Figure 5.1. The derivation here follows the method presented in [41]. The starting point is the governing PDEs for mass and energy, Equation 5.4 and Equation 5.5. Integrating along the length of the heat exchanger and applying the lumped parameter assumptions gives the conservation of mass in Equation 5.6 and Equation 5.7 and the conservation of energy in Equation 5.8 and Equation 5.9 for the superheat and two-phase regions of the heat exchanger.

$$\frac{\partial(\rho A_{cs})}{\partial t} + \frac{\partial(\dot{m})}{\partial z} = 0 \quad (5.4)$$

$$\frac{\partial(\rho A_{cs} h - A_{cs} P)}{\partial t} + \frac{\partial(\dot{m} h)}{\partial z} = p_i \alpha_i (T_w - T_r) \quad (5.5)$$

$$\left(\frac{\partial \rho_1}{\partial P_c} + \frac{1}{2} \frac{\partial \rho_1}{\partial h_1} \frac{dh_g}{dP_c} \right) A_{cs} L_1 \dot{P}_c + \left(\frac{1}{2} \frac{\partial \rho_1}{\partial h_1} \right) A_{cs} L_1 \dot{h}_i + (\rho_1 - \rho_g) A_{cs} \dot{L}_1 = \dot{m}_i - \dot{m}_{int1} \quad (5.6)$$

$$(\rho_g - \rho_f)(1 - \bar{\gamma}) A_{cs} \dot{L}_1 + \left(\frac{d\rho_f}{dP_c} (1 - \bar{\gamma}) + \frac{d\rho_g}{dP_c} (\bar{\gamma}) \right) A_{cs} L_2 \dot{P}_c + (\rho_g - \rho_f) A_{cs} L_2 \dot{\bar{\gamma}} = \dot{m}_{int1} - \dot{m}_{int2} \quad (5.7)$$

$$\left[\left(\frac{\partial \rho_1}{\partial P_c} + \frac{1}{2} \frac{\partial \rho_1}{\partial h_1} \frac{dh_g}{dP_c} \right) h_1 + \left(\frac{1}{2} \frac{dh_g}{dP_c} \right) \rho_1 - 1 \right] A_{cs} L_1 \dot{P}_c + \left[\left(\frac{1}{2} \frac{\partial \rho_1}{\partial h_1} \right) h_1 + \left(\frac{1}{2} \right) \rho_1 \right] A_{cs} L_1 \dot{h}_i + (\rho_1 h_1 - \rho_g h_g) A_{cs} \dot{L}_1 \quad (5.8)$$

$$= \dot{m}_i h_i - \dot{m}_{int1} h_g + \alpha_{i1} A_i \left(\frac{L_1}{L_r} \right) (T_{w1} - T_{r1})$$

$$(\rho_g h_g - \rho_f h_f)(1 - \bar{\gamma}) A_{cs} \dot{L}_1 + (\rho_g h_g - \rho_f h_f) A_{cs} L_2 \dot{\bar{\gamma}} + \left(\frac{d(\rho_f h_f)}{dP_c} (1 - \bar{\gamma}) + \frac{d(\rho_g h_g)}{dP_c} (\bar{\gamma}) - 1 \right) A_{cs} L_2 \dot{P}_c \quad (5.9)$$

$$= \dot{m}_{int1} h_g - \dot{m}_{int2} h_{int2} + \alpha_{i2} A_i \left(\frac{L_2}{L_r} \right) (T_{w2} - T_{r2})$$

The heat exchanger wall energy conservation equations are given as Equation 5.10 and Equation 5.11.

$$(C_P \rho V)_w \left(\dot{T}_{w1} + \frac{T_{w1} - T_{w2}}{L_1} \dot{L}_1 \right) = \alpha_{i1} A_i (T_{r1} - T_{w1}) + \alpha_o A_o (T_a - T_{w1}) \quad (5.10)$$

$$(C_P \rho V)_w \dot{T}_{w2} = \alpha_{i2} A_i (T_{r2} - T_{w2}) + \alpha_o A_o (T_a - T_{w2}) \quad (5.11)$$

Equations 5.6 through 5.11 together with Equations 5.1 and 5.3 from the receiver are combined to eliminate the variables \dot{m}_{int1} and \dot{m}_{int2} , resulting in a model with six states: $x_c = [L_1 \quad P_c \quad m_{rec} \quad \bar{\gamma} \quad T_{w1} \quad T_{w2}]^T$.

The model inputs are defined as $u_c = [\dot{m}_{c,in} \quad \dot{m}_{c,out} \quad h_{c,in} \quad T_{c,air,in} \quad \dot{m}_{c,air} \quad T_{amb}]^T$. The resulting model is given in Equation 5.12 in descriptor form, $Z_c(x_c, u_c) \cdot \dot{x}_c = f_c(x_c, u_c)$, with the elements of the $Z_c(x_c, u_c)$ matrix found in Table 5.1.

$$\begin{bmatrix} z_{11} & z_{12} & 0 & 0 & 0 & 0 \\ z_{21} & z_{22} & z_{23} & z_{24} & 0 & 0 \\ z_{31} & z_{32} & z_{33} & z_{34} & 0 & 0 \\ 0 & z_{42} & 0 & z_{44} & 0 & 0 \\ z_{51} & 0 & 0 & 0 & z_{55} & 0 \\ 0 & 0 & 0 & 0 & 0 & z_{66} \end{bmatrix} \begin{bmatrix} \dot{L}_1 \\ \dot{P}_c \\ \dot{\gamma} \\ \dot{m}_{rec} \\ \dot{T}_{w1} \\ \dot{T}_{w2} \end{bmatrix} = \begin{bmatrix} \dot{m}_i(h_i - h_g) + \alpha_{i1} A_i \left(\frac{L_1}{L_{Total}} \right) (T_{w1} - T_{r1}) \\ \dot{m}_o(h_g - h_{int2}) + \alpha_{i2} A_i \left(\frac{L_2}{L_{Total}} \right) (T_{w2} - T_{r2}) \\ \dot{m}_i - \dot{m}_o \\ \dot{m}_o(h_{int2} - h_f) - UA_{rec}(T_{rec} - T_{amb}) \\ \alpha_{i1} A_i (T_{r1} - T_{w1}) + \alpha_o A_o (T_a - T_{w1}) \\ \alpha_{i2} A_i (T_{r2} - T_{w2}) + \alpha_o A_o (T_a - T_{w2}) \end{bmatrix} \quad (5.12)$$

Table 5.1 Entries of $Z_c(x_c, u_c)$ for the condenser with receiver model

z_{11}	$(\rho_1 h_1 - \rho_1 h_g) A_{cs}$
z_{12}	$\left[\left(\frac{\partial \rho_1}{\partial P_c} + \frac{1}{2} \frac{\partial \rho_1}{\partial h_1} \frac{dh_g}{dP_c} \right) (h_1 - h_g) + \left(\frac{1}{2} \frac{dh_g}{dP_c} \right) \rho_1 - 1 \right] A_{cs} L_1$
z_{21}	$(\rho_f h_g - \rho_f h_f) (1 - \bar{\gamma}) A_{cs}$
z_{22}	$\left(\frac{d(\rho_f h_f)}{dP_c} (1 - \bar{\gamma}) + \frac{d(\rho_g h_g)}{dP_c} \bar{\gamma} - \frac{d\rho_f}{dP_c} h_g (1 - \bar{\gamma}) - \frac{d\rho_g}{dP_c} h_g \bar{\gamma} - 1 \right) A_{cs} L_2$
z_{23}	$(\rho_f h_g - \rho_f h_f) A_{cs} L_2$
z_{24}	$(h_{int2} - h_g)$
z_{31}	$[\rho_1 - \rho_f (1 - \bar{\gamma}) - \rho_g \bar{\gamma}] A_{cs}$
z_{32}	$\left[\left(\frac{d\rho_f}{dP_c} (1 - \bar{\gamma}) + \frac{d\rho_g}{dP_c} \bar{\gamma} \right) L_2 + \left(\frac{\partial \rho_1}{\partial P_c} + \frac{1}{2} \frac{\partial \rho_1}{\partial h_1} \frac{dh_g}{dP_c} \right) L_1 \right] A_{cs}$
z_{33}	$(\rho_g - \rho_f) A_{cs} L_2$
z_{34}	1
z_{42}	$\frac{d\rho_g}{dP_c} V_g u_g + \frac{d\rho_f}{dP_c} V_f u_f + m_g \frac{du_g}{dP_c} + m_f \frac{du_f}{dP_c} - \left(\frac{\rho_g u_g - \rho_f u_f}{\rho_g - \rho_f} \right) \left(\frac{d\rho_g}{dP_c} V_g + \frac{d\rho_f}{dP_c} V_f \right)$
z_{44}	$\left(\frac{\rho_g u_g - \rho_f u_f}{\rho_g - \rho_f} - h_{int2} \right)$
z_{51}	$(c_p \rho V)_w \left(\frac{T_{w1} - T_{w2}}{L_1} \right)$
z_{55}	$(c_p \rho V)_w$
z_{66}	$(c_p \rho V)_w$

5.2.5 Nonlinear Evaporator with Accumulator

When connected to an accumulator containing fluid in the liquid phase, the evaporator outlet condition is saturated vapor ($x_{out} = 1$) or two-phase fluid ($x_{out} < 1$) at equilibrium. The derivation follows the method presented in [42]. The conservation of mass and conservation of energy equations are found in Equation 5.13 and Equation 5.14.

$$\left(\frac{d\rho_f}{dP_e}(1-\bar{\gamma}) + \frac{d\rho_g}{dP_e}(\bar{\gamma}) \right) A_{cs} L_T \dot{P}_e + (\rho_g - \rho_f) A_{cs} L_T \dot{\bar{\gamma}} = \dot{m}_{in} - \dot{m}_{int} \quad (5.13)$$

$$\left(\frac{d(\rho_f h_f)}{dP_e}(1-\bar{\gamma}) + \frac{d(\rho_g h_g)}{dP_e}(\bar{\gamma}) - 1 \right) A_{cs} L_T \dot{P}_e + (\rho_g h_g - \rho_f h_f) A_{cs} L_T \dot{\bar{\gamma}} = \dot{m}_{in} h_{in} - \dot{m}_{int} h_{int} + \alpha_i A_i (T_w - T_r) \quad (5.14)$$

The conservation of energy equation for the evaporator wall is given in Equation 5.15.

$$(C_p \rho V)_w \dot{T}_w = \alpha_i A_i (T_r - T_w) + \alpha_o A_o (T_a - T_w) \quad (5.15)$$

The above equations are combined to eliminate the interface mass flow variable, \dot{m}_{int} , between the evaporator and the accumulator. Combining the resulting equations with the equations for the accumulator results in a fourth-order model with states $x_e = [P_e \quad m_{rec} \quad \bar{\gamma} \quad T_w]^T$ and inputs

$$u_e = [\dot{m}_{e,in} \quad \dot{m}_{e,out} \quad h_{e,in} \quad T_{e,air,in} \quad \dot{m}_{e,air} \quad T_{amb}]^T. \text{ Writing the equations in descriptor form gives Equation}$$

5.16. The entries of $Z_e(x_e, u_e)$ are found in Table 5.2.

$$\begin{bmatrix} z_{11} & z_{12} & z_{13} & 0 \\ z_{21} & z_{22} & z_{23} & 0 \\ z_{31} & z_{32} & 0 & 0 \\ 0 & 0 & 0 & z_{44} \end{bmatrix} \begin{bmatrix} \dot{P}_e \\ \dot{m}_{acc} \\ \dot{\bar{\gamma}} \\ \dot{T}_w \end{bmatrix} = \begin{bmatrix} \dot{m}_{in} - \dot{m}_{out} \\ \dot{m}_{in} h_{in} - \dot{m}_{out} h_g + \alpha_i A_i (T_w - T_r) \\ \dot{m}_{out} (h_g - h_{out}) - UA_{rec} (T_{acc} - T_{amb}) \\ \alpha_i A_i (T_r - T_w) + \alpha_o A_o (T_a - T_w) \end{bmatrix} \quad (5.16)$$

Table 5.2 Entries of $Z_e(x_e, u_e)$ for the evaporator with accumulator model

z_{11}	$\left[\left(\frac{d\rho_f}{dP_e} \right) (1-\bar{\gamma}) + \left(\frac{d\rho_g}{dP_e} \right) (\bar{\gamma}) \right] A_{cs} L_{Total}$
z_{12}	1
z_{13}	$(\rho_g - \rho_f) A_{cs} L_{Total}$
z_{21}	$\left[\left(\frac{d(\rho_f h_f)}{dP_e} \right) (1-\bar{\gamma}) + \left(\frac{d(\rho_g h_g)}{dP_e} \right) (\bar{\gamma}) - 1 \right] A_{cs} L_{Total}$
z_{22}	h_{int}
z_{23}	$(\rho_g h_g - \rho_f h_f) A_{cs} L_{Total}$

z_{31}	$\left(\frac{d\rho_g}{dP_e} V_g u_g + \frac{d\rho_f}{dP_e} V_f u_f + \frac{du_g}{dP_e} \rho_g V_g + \frac{du_f}{dP_e} \rho_f V_f \right)$ $- \left(\frac{\rho_g u_g - \rho_f u_f}{\rho_g - \rho_f} \right) \left(\frac{d\rho_g}{dP_e} V_g + \frac{d\rho_f}{dP_e} V_f \right)$
z_{32}	$\left(\frac{\rho_g u_g - \rho_f u_f}{\rho_g - \rho_f} - h_{\text{int}} \right)$
z_{44}	$(C_p \rho V)_w$

5.2.6 Pseudo-Quality and Mean Void Fraction

The mean void fraction, $\bar{\gamma}$, was chosen in the condenser with receiver and evaporator with accumulator derivations as a dynamic state. The mean void fraction is used to determine the fluid properties at the outlet of the heat exchanger. A Slip-Ratio [43] void fraction correlation relates the void fraction to the quality at any point in the

two phase region, as shown in Equation 5.17, where $\mu_s = \left(\frac{\rho_g}{\rho_f} \right) S$.

$$\gamma = \frac{x}{x + (1-x)\mu_s} \quad (5.17)$$

The mean void fraction, Equation 5.18, results from integrating Equation 5.17 from x_{in} to x_{out} . This equation relates the mean void fraction to the inlet and outlet quality of the two-phase region. Once the outlet quality is obtained, all other outlet conditions may be calculated.

$$\bar{\gamma} = \frac{1}{(1-\mu_s)} + \frac{\mu_s}{(x_{\text{out}} - x_{\text{in}})(1-\mu_s)^2} \ln \left[\frac{\mu_s + x_{\text{in}}(1-\mu_s)}{\mu_s + x_{\text{in}}(1-\mu_s) + (x_{\text{out}} - x_{\text{in}})(1-\mu_s)} \right] \quad (5.18)$$

5.2.6.1 Condenser with Receiver Outlet Quality

At steady-state, the inlet fluid of the condenser with receiver two-phase region is saturated vapor ($x_{\text{in}} = 1$) and the outlet fluid is saturated liquid ($x_{\text{out}} = 0$) or two-phase liquid ($x_{\text{out}} > 0$). We would like to use Equation 5.18 to obtain the outlet quality for small deviations from saturated liquid conditions, but the equation is transcendental in outlet quality. Assuming small deviations from saturated liquid outlet conditions, we set $x_{\text{out}} = 0$ outside of the

natural log to arrive at Equation 5.19. Solving for x_{out} yields Equation 5.20, where $a = \frac{\mu_s}{1-\mu_s}$ and $b = \frac{1}{1-\mu_s}$.

$$\bar{\gamma} \approx \frac{1}{1-\mu_s} - \frac{\mu_s}{(1-\mu_s)^2} \ln \left[\frac{1}{\mu_s + x_{\text{out}}(1-\mu_s)} \right]. \quad (5.19)$$

$$x_{\text{out}} = b e^{\left(\frac{\bar{\gamma}-b}{ab} \right)} - a \quad (5.20)$$

5.2.6.2 Evaporator with Accumulator Outlet Quality

As with the condenser with receiver derivation, the mean void fraction is a dynamic state of the evaporator with accumulator model. Equation 5.18 again provides the means of relating mean void fraction to quality. We

assume small deviations from saturated vapor outlet conditions, setting $x_{out} = 1$ inside of the natural log to arrive at Equation 5.21. Solving for x_{out} yields Equation 5.22.

$$\bar{\gamma} \approx \frac{1}{1 - \mu_s} + \frac{\mu_s}{(x_{out} - x_{in})(1 - \mu_s)^2} \ln[\mu_s + x_{in}(1 - \mu_s)] \quad (5.21)$$

$$x_{out} = \frac{\mu_s \ln[\mu_s + x_{in}(1 - \mu_s)]}{(1 - \mu_s)^2 \bar{\gamma} - (1 - \mu_s)} + x_{in} \quad (5.22)$$

5.2.6.3 Pseudo-Quality

During simulation, some transients will cause the condenser outlet fluid to deviate towards subcooled conditions or the evaporator outlet fluid to deviate towards superheated conditions. When quality is calculated from the mean void fraction, Equation 5.20 and Equation 5.22, these deviations result in heat exchanger outlet quality values less than zero (condenser) and greater than one (evaporator). We therefore define a “pseudo-quality” that exists outside the normal bounds on quality, $x \in [0,1]$. This pseudo-quality is defined as

$\hat{x} \in [(0 - \varepsilon, 0) \cup (1, 1 + \varepsilon)]$, where $0 < \varepsilon \ll 1$. By using the two-phase property relationships with the pseudo-quality, outlet property approximations that capture the gross property behavior are obtained. This approach avoids the complications of switching between multiple model structures during simulation.

5.2.6.4 Validity of Pseudo-Quality Assumptions

This section addresses the validity of two key assumptions: the small deviation assumption used to derive Equation 5.19 and Equation 5.21 and the assumption that approximate refrigerant properties calculated from the pseudo-quality capture the basic behavior of the true refrigerant properties with sufficient accuracy for dynamic modeling purposes.

Figure 5.5 compares the mean void fraction of Equation 5.18 with the mean void fraction resulting from application of the condenser and evaporator small outlet quality deviation assumptions; see Equation 5.19 and Equation 5.21.

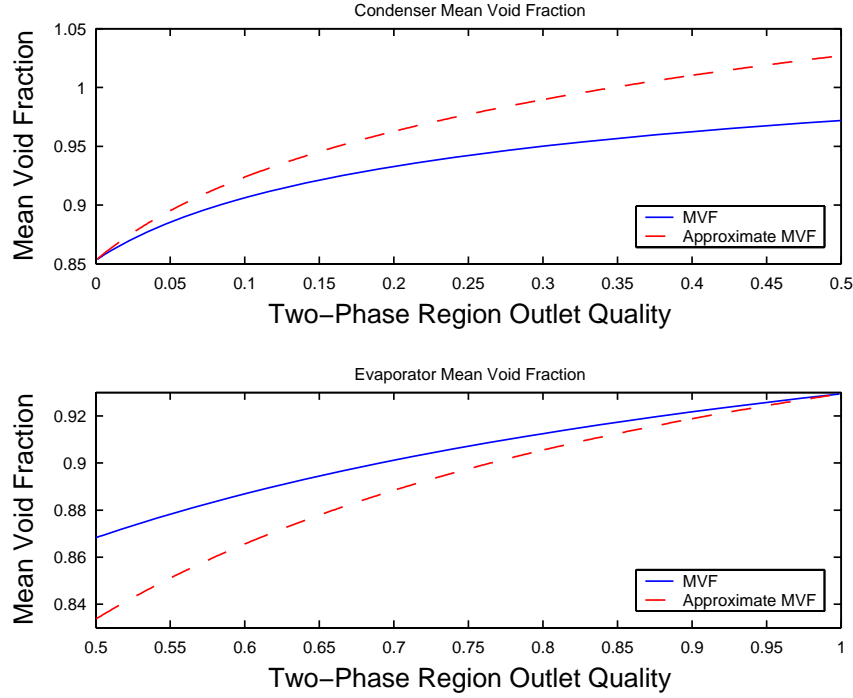


Figure 5.5 Mean void fraction for two-phase flows operating at 900 kPa (condenser) and 320 kPa (evaporator) as a function of the outlet quality

In the case of the condenser, deviations over the range $x_{out} \in [0, 0.2]$ result in errors lower than 3.5%. In the case of the evaporator, deviations over the range $x_{out} \in [0.8, 1]$ result in errors lower than 1%. Therefore, under these normal simulation conditions, the small deviation assumptions applied to the mean void fraction do not produce significant errors. The small deviation assumptions should not be applied to other operating conditions, such as start-up and shut-down transients where large deviations in heat exchanger outlet conditions are probable.

If a superheat region develops in the evaporator, the outlet enthalpy will increase with the outlet temperature. The approximate outlet enthalpy is calculated from the pseudo-quality as if the refrigerant were two-phase: $h = h_f(1 - \hat{x}) + h_g \hat{x}$. As the outlet conditions become more superheated, the mean void fraction increases and the pseudo-quality increases. This increasing pseudo-quality results in an increasing outlet enthalpy, demonstrating that the properties calculated from the pseudo-quality capture the key behavior of the true properties. A similar argument could be made for the case of subcooled outlet conditions in the condenser with negative pseudo-quality values.

5.3 Compressor Shell Thermal Capacitance Dynamic

The development of a dynamic model to capture the effect of the compressor shell thermal capacitance was motivated by observations of data from the experimental system. The observed response speed of the compressor outlet temperature was much slower than the response speed predicted by simulations. The difference in response speed was attributed to the heating and cooling of the compressor's metal shell, which represents a significant

thermal capacitance. Temperature data such as that shown in Figure 5.6 indicates that a first-order dynamic model would be sufficiently accurate to capture the effect of the compressor shell thermal capacitance on the outlet temperature. In [11], the authors point out that the temperatures in the compressor shell converge very slowly to a steady-state value due to the high thermal capacity of the metal and oil in the shell. They also use a thermal capacitance model to account for the compressor shell dynamics.

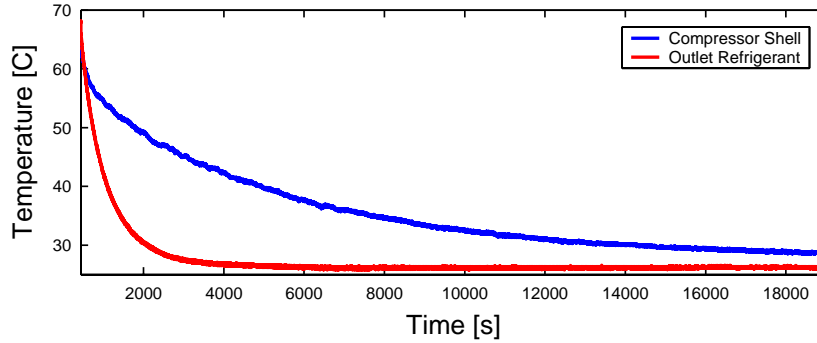


Figure 5.6 Compressor shell and refrigerant outlet temperature data for system shutdown from 1600 RPM

Using the data in Figure 5.6, time constants may be found for both the refrigerant temperature decay and the shell temperature decay. The time constant of the shell temperature decay is approximately 4490 seconds, and the time constant of the refrigerant temperature decay is approximately 610 seconds. The refrigerant temperature was measured with an immersion thermocouple, while the compressor shell temperature shell temperature was measured with a contact thermocouple.

5.3.1 Implementation in Thermosys

The desired first-order response is achieved by filtering the semi-empirical model's static enthalpy prediction. The filter transfer function is given in Equation 5.23, where τ is the chosen time constant for the first-order response.

$$\frac{h_{out}}{h_{out,semi-empirical}} = \frac{1}{\tau s + 1} \quad (5.23)$$

The transfer function is depicted in block diagram form in Figure 5.7.

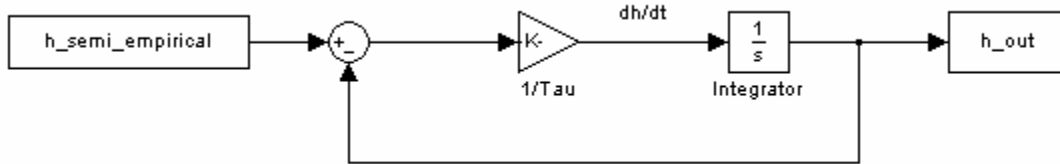


Figure 5.7 Block diagram of Equation 5.23

In the Thermosys framework, dynamic component models calculate state derivatives which are then integrated to find the states. The time derivative of the compressor outlet enthalpy is found by examination of Figure 5.7 to be the following:

$$\dot{h}_{out} = \frac{h_{out,semi-empirical} - h_{out}}{\tau} \quad (5.24)$$

The time constant is set by the user in the compressor graphical user interface.

The following plots compare output of compressor models for various time constant values. Figure 5.8 shows the compressor outlet temperature data for a test with numerous large compressor steps. Note the different scales of the temperature data (blue, left side) and the model output (green, right side). The data shows minimal temperature fluctuations compared to those of the model. The model output was generated with a time constant of 0.5 seconds, approximating a model without the compressor shell dynamic. Similar results motivated the development of the thermal capacitance model. Figure 5.9 shows the same temperature data with model output generated by various compressor shell time constants. The results indicate that a time constant between 1200 seconds and 1500 seconds is appropriate. These time constants fall between the shell and refrigerant temperature decay time constants observed from system data.

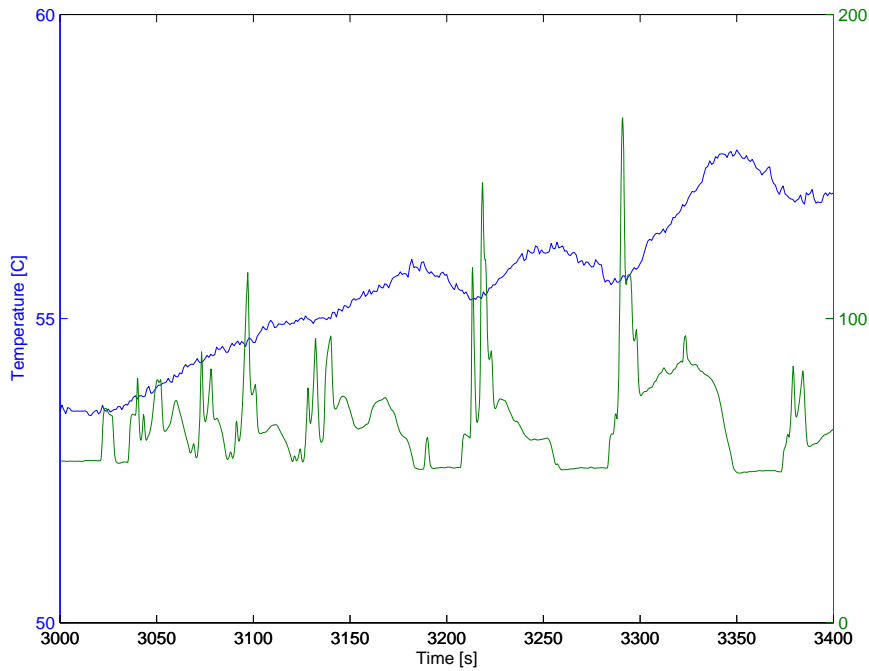


Figure 5.8 Compressor outlet temperature data (blue) and small time constant model output (green)

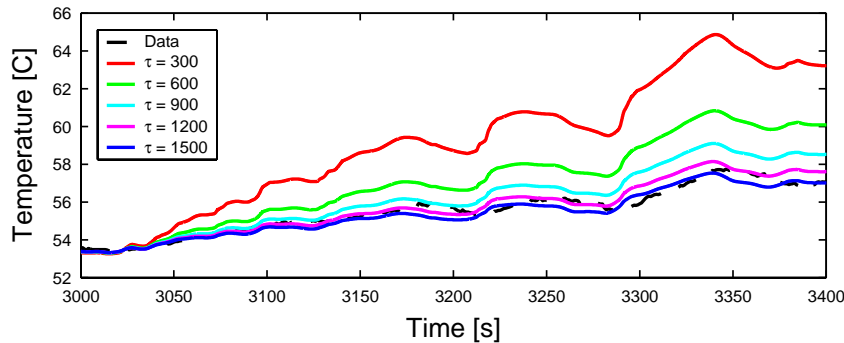


Figure 5.9 Compressor outlet temperature model output for various time constants

5.4 Identified Compressor Mass Flow Model

While the previous section dealt with improving the transient compressor enthalpy prediction, this section addresses the accuracy of the compressor mass flow rate prediction. In the case of the compressor mass flow prediction, early model validation efforts revealed that the static compressor performance map model was not adequately predicting true system behavior during transients. The inaccuracy of the mass flow model caused significant inaccuracy in other model outputs, particularly the evaporator pressure. Possible causes of the discrepancies could be deficiencies in the compressor model itself, unmodeled components such as the oil separator, or interactions between the various component models. Since no physical understanding of the source of the model errors is available, a system identification approach was chosen to find a mass flow correction. The necessary mass flow correction is first isolated from simulation and system data using an iterative learning control (ILC) algorithm. Standard system identification techniques are then used to find a simple model for the mass flow correction.

5.4.1 Compressor Mass Flow Dynamics Isolation

The first step in this identification method is the isolation of the mass flow correction from simulation output and experimental system data. The static, semi-empirical compressor model is the baseline compressor model. An iterative learning control algorithm [36,5] is used to identify a compressor mass flow rate correction. The ILC algorithm adjusts the compressor mass flow rate to reduce the error in one of the model outputs, in this case the evaporator pressure. Figure 5.10 shows a schematic of the isolation procedure.

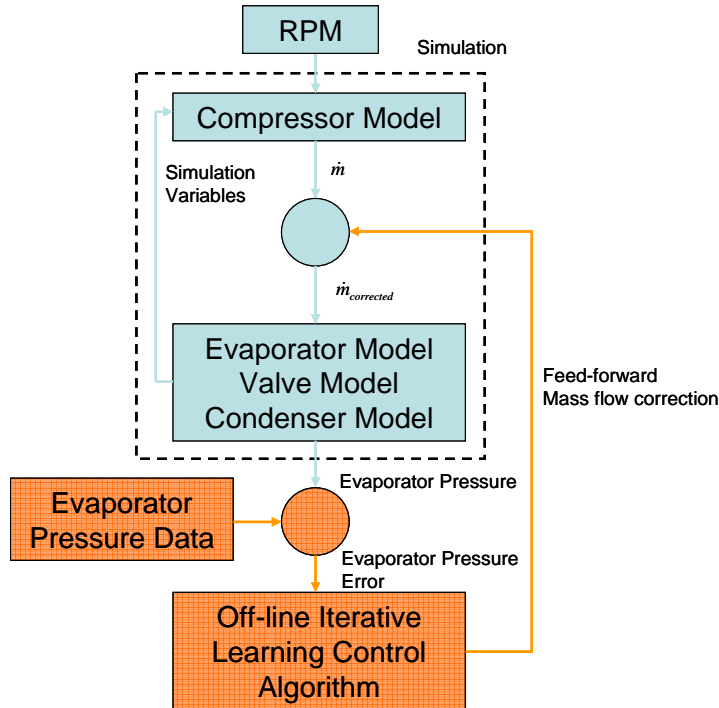


Figure 5.10 Compressor mass flow dynamics isolation procedure

For the first run of the simulation, the baseline static compressor model produces a compressor mass flow rate prediction. This mass flow rate is passed to the other component models which, in turn, generate additional model outputs. After the simulation has finished, the evaporator pressure model output is compared to evaporator pressure data to generate an evaporator pressure error signal. This error signal is passed to the PD-type ILC

algorithm given in Equation 5.25, where P and D are tunable gains on the evaporator pressure error and pressure error derivative, j is the iteration number, and T is the data length.

$$\dot{m}(t)_{\text{correction},j} = \dot{m}(t)_{\text{correction},j-1} + P \cdot e(t)_{j-1} + D \cdot \dot{e}(t)_{j-1} \quad t \in [0, T] \quad (5.25)$$

The ILC algorithm produces a feed-forward mass flow rate correction signal that is applied to the mass flow rate predicted by the static compressor model during the next iteration of the simulation. Iterations continue until the evaporator pressure RMS error reaches an acceptably small value. At the final iteration, the mass flow rate correction signal represents an isolation of the compressor mass flow rate dynamics not captured by the static compressor model.

5.4.2 Identification of Isolated Dynamics

After isolation of the compressor mass flow dynamics, a model is identified to capture the dynamic behavior in simulation. Any standard system identification technique could be applied to this problem; see [32] for examples. MATLAB's System Identification Toolbox has been more than adequate for identifying the dynamic mass flow correction model. Two examples of the application of this technique are found in Chapter 7.

5.5 Compressor Cycling Dynamics

While it is not an efficient capacity control method [27], compressor cycling is frequently used in vapor compression cycle systems with fixed-speed compressors. Compressor cycling produces very large transients that cause substantial difficulties in the moving-boundary modeling framework. As with the heat exchanger with receiver/accumulator model, the main challenge is the destruction and creation of dynamic states due to a changing number of fluid regions in the heat exchangers. The cycling transients are so severe that they cannot be handled with the modeling assumptions applied to the heat exchanger with receiver/accumulator models. A compressor cycling model also requires an accurate prediction of mass flow behavior for the expansion device and the compressor at very low mass flow rates. A similar but more challenging problem is system start-up. In addition to the cycling difficulties already mentioned, modeling start-up transients requires knowledge of the initial distribution of refrigerant charge in the system. Modeling start-up transients is a difficult challenge for even the well-developed commercial modeling tools. This work will focus on possible solutions to the slightly less challenging compressor cycling problems. Overcoming the compressor cycling challenges will be a first step towards modeling start-up transients. A review of current Thermosys model capabilities in regards to cycling transients is provided as a starting point for future research.

5.5.1 Literature Review

Two papers based on the moving-boundary framework have discussed modeling techniques appropriate for capturing compressor cycling behavior. In the follow sections, the work of Dhar and Soedel [11] is briefly described, followed by a discussion of the work of Pettit, Willatzen, and Ploug-Sorensen [47, 38].

5.5.1.1 Dhar and Soedel

Dhar and Soedel present the component models necessary to simulate a complete VCC system. Three condenser models are presented: a superheated model, a two-phase model, and a subcooled model. The three models may be combined to form a condenser model with multiple fluid regions. Only one evaporator model is presented. Logic statements are used in the main simulation program to call the correct heat exchanger subroutine.

Simulation results indicate that the models were used for a system start-up simulation that should require model switching. The paper does not indicate how potential discontinuities and numerical difficulties are handled, but the simulation output appears to be free of discontinuities. The lack of multiple evaporator model structures raises questions as to the applicability of the model to start-up transients. It is expected that the evaporator would operate with different combinations of fluid regions during the severe start-up transients.

5.5.1.2 Willatzen, Pettit, and Ploug-Sorensen

Willatzen, Pettit, and Ploug-Sorensen derive a generic moving-boundary heat exchanger model very similar to those of [19]. They do not include expansion device or compressor models.

The authors go to great length to explain their approach for handling the discontinuities and numerical challenges associated with switching model structures during simulation. The models are implemented in ACSL, a modeling environment for continuous dynamic systems. This platform was chosen because it allows for event-driven procedures and user access to integrator properties.

The evaporator model is given as an example of their approach. Four model structures are considered: a subcool/two-phase/superheat model, a subcool/two-phase model, a two-phase model, and a two-phase/superheat model. The models are made up of explicit equations for the state derivatives. The major contribution of the paper is the discussion of what to do with these state derivatives when the physical entities that they represent are no longer active in the model. Two guiding principles are presented. First, if a state going to zero will adversely affect numerics, do not allow the state to go all the way to zero. Second, force inactive states to track a meaningful physical value. The value to be tracked is determined by the desired state value at the time of its reactivation in the model. For example, consider the case of an evaporator switching from a subcool/two-phase/superheat model to a two-phase/superheat model. As the model structure switch occurs, the subcooled region length goes to zero and the subcooled region wall temperature state becomes inactive. The length is prevented from reaching zero by changing the original length derivative equation to Equation 5.26 when a model switch is imminent.

$$\dot{L}_{e1} = -(L_{e1} - \varepsilon) \quad (5.26)$$

The inactive wall temperature is forced to track the adjacent active wall temperature by replacing the original temperature state derivative equation with Equation 5.27. The parameter k is a time constant that controls how quickly the inactive wall temperature converges to the value of the active wall temperature.

$$\dot{T}_{ew1} = k(T_{ew2} - T_{ew1}) \quad (5.27)$$

Using this method, if the subcooled region is reactivated in the model, the length will start from a small non-zero value and the subcooled region wall temperature will start with the same value as the adjacent two-phase region wall temperature.

The model structure switching is based on the inlet and outlet refrigerant enthalpy. If the inlet enthalpy is less than the saturated liquid enthalpy, the subcooled region is included. If the outlet enthalpy is greater than the saturated vapor enthalpy, the superheat region is included.

No model validation results are presented in the papers, but simulation results are presented for a number of model outputs. The model inputs are shaped such that switching between various model structures occurs during the

simulation. The usefulness of the simulation results is questionable because the pressure state was set to a constant value and the inlet and outlet mass flow rates were forced to be equivalent throughout the simulation.

5.5.2 Current Thermosys Model Cycling Capabilities

The existing Thermosys heat exchanger models are capable of modeling some cycling conditions without modification. The models are first tested to evaluate their response to a large reduction in compressor speed (quasi shut-down). The model output is compared to data from a quasi shut-down test carried out on the experimental system described in Chapter 6. The quasi shut-down simulation is used to determine the length of time that the moving-boundary models will run before the modeling assumptions are violated and to determine which modeling assumptions are violated. The models are also tested under cycling conditions, and the results are qualitatively compared to cycling data from the experimental system.

5.5.2.1 Quasi Shut-down Test: Simulation Results

The models were first tested to see how long they would run after a compressor speed step from 1600 RPM to 100 RPM. The compressor speed was not set to zero, so this was not a true shut-down test. A true shut-down test is not performed due to the lack of data characterizing the behavior of the compressor at zero RPM. Future work should overcome this deficiency.

The initial quasi shut-down simulation revealed that the condenser with receiver model experiences numerical difficulties brought on by the large compressor step, as seen in Figure 5.11. The condenser with receiver model computes a matrix inversion at each time step to find the state derivatives. The large compressor step drives the model to an operating condition that causes this matrix to become singular. The effects of the singularity can be reduced by specifying a stiff solver in Simulink, but these solvers greatly increase the simulation time. The numerical difficulties occur when the z_{44} entry in the Z matrix (see Chapter 5) goes to zero. For the results presented here, the model was modified to prevent the z_{44} entry from approaching zero by enforcing the following condition: $z_{44} \in (-\infty, -5] \cup [5, \infty)$. Using this model modification, the model output was relatively smooth, and the faster standard solvers could be used. Other potential solutions to the numerical problems are the subject of future research.

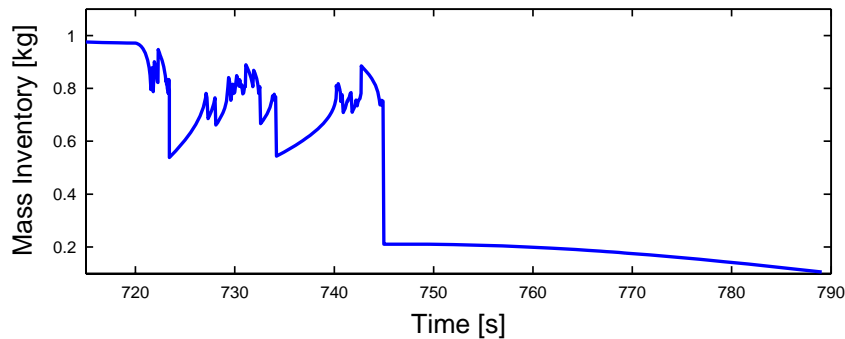


Figure 5.11 Receiver mass inventory showing numerical instability

Figure 5.12 through Figure 5.16 show the simulation response for the system model. The model was stopped because the length of the superheat region in the evaporator went to zero. The model ran for approximately 120 seconds following the compressor step.

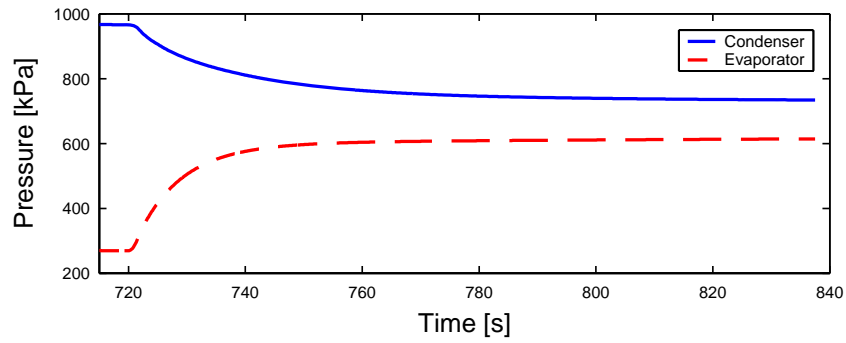


Figure 5.12 Pressures

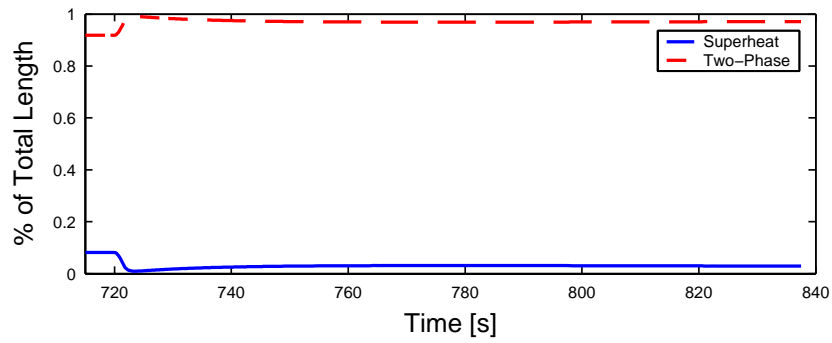


Figure 5.13 Condenser fluid region lengths

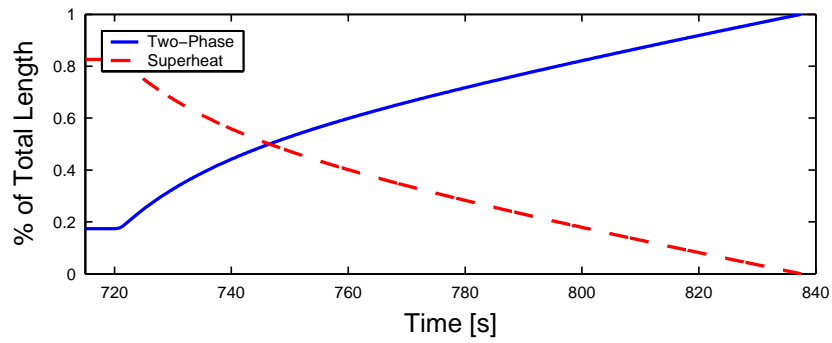


Figure 5.14 Evaporator fluid region lengths with the superheat length vanishing

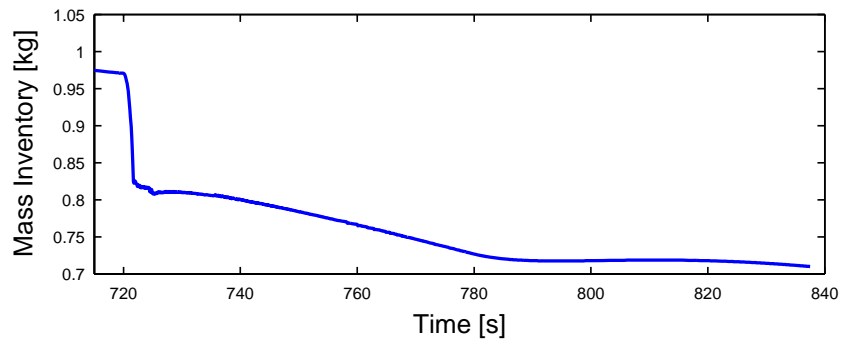


Figure 5.15 Receiver mass inventory

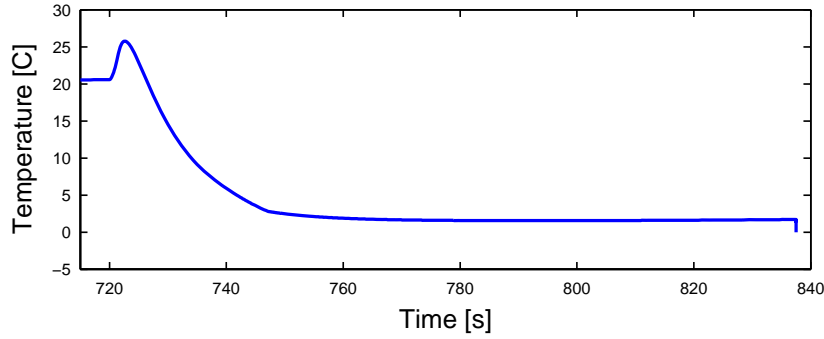


Figure 5.16 Evaporator superheat

5.5.2.2 Quasi Shut-down Test: Experimental Data

Figure 5.17 and Figure 5.18 show experimental system data for a compressor step from 1600 RPM to 100 RPM. The initial conditions and the time length presented on the plots are similar to that of the simulation results presented in the previous section. Two variables of interest, receiver charge inventory and fluid region length, cannot be measured. However, heat exchanger pressures and evaporator superheat provide insight into system shut-down behavior. The system pressure data shows the two pressures approaching steady-state values that are similar to those approached by the model. The evaporator superheat data does not show the non-minimum phase behavior found in the model output. The source of the non-minimum phase behavior is unknown, but the extent of the behavior can be mitigated by adjusting the internal heat transfer coefficients. Minimizing both the two-phase and superheat region heat transfer coefficients has been found to minimize the non-minimum phase behavior. Also, it is possible that sensor dynamics prevent the observation of non-minimum phase behavior in the physical system. Both superheat data and model output decay to similar steady-state values of two to three degrees C. The model again responds faster than the experimental system. The difference in response speed could be caused by inaccurate valve and compressor performance maps at very low flow rates. Based on the evaporator pressure responses in Figure 5.12 and Figure 5.17, the system data shows a time constant of approximately 60 seconds, while the model shows a time constant of approximately 20 seconds.

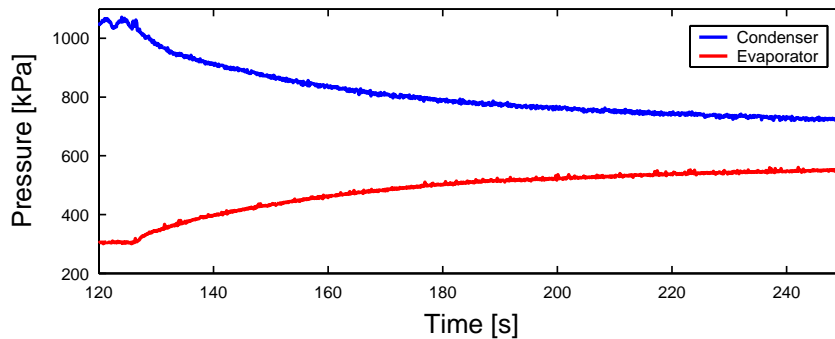


Figure 5.17 System pressure data

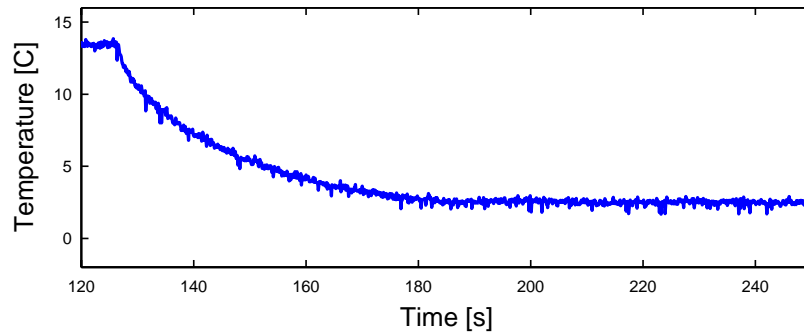


Figure 5.18 System evaporator superheat data

5.5.2.3 Quasi Cycling Test: Simulation

The system model was also evaluated under approximate compressor cycling conditions. The compressor speed was stepped between 1600 RPM and 100 RPM. The system was simulated with a cycling period of 140 seconds. Simulation results are shown in Figure 5.19 through Figure 5.22.

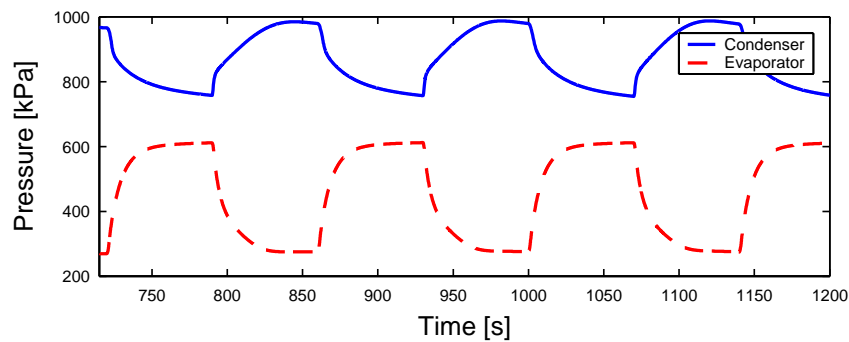


Figure 5.19 System pressures

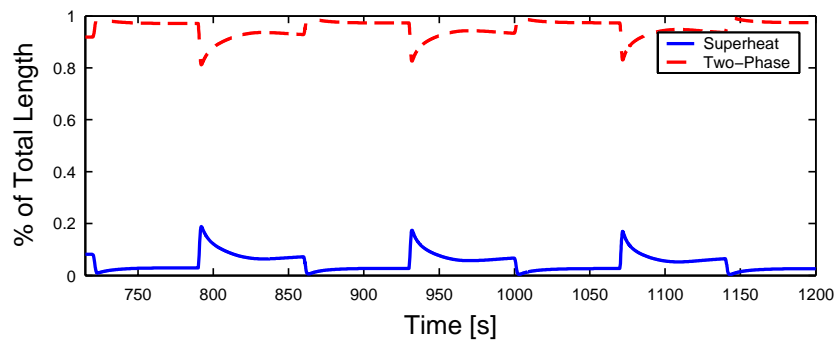


Figure 5.20 Condenser lengths

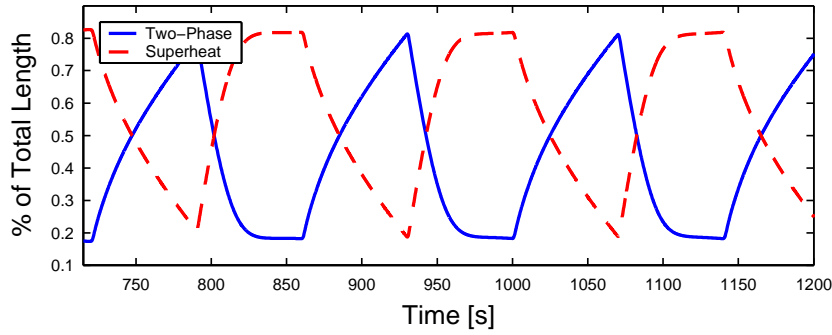


Figure 5.21 Evaporator lengths

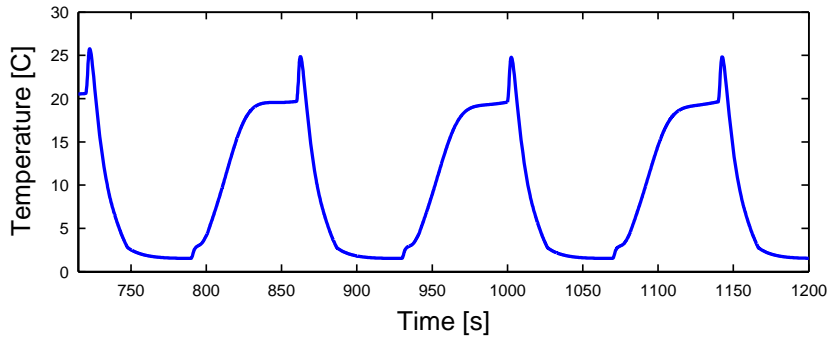


Figure 5.22 Evaporator superheat

5.5.2.4 Quasi Cycling Test: Experimental Data

The experimental system was run under cycling conditions similar to those used in the simulation. The system pressures and superheat data are found in Figure 5.23 and Figure 5.24. The qualitative aspects of the pressure model and data are very similar. The model again responds to compressor steps faster than the data. The pressure data does not reach a steady-state value between steps, so an evaluation of steady-state accuracy is not possible. The superheat data and model output are significantly different. The data shows a loss of superheat following the first compressor speed increase. The evaporator is subsequently unable to consistently regain a level of superheat. The model does not predict this loss of superheat; it shows large fluctuations in superheat for each compressor step. Very short cycling periods were also tested, but superheat was always lost. Shortening the cycling period delayed the onset of superheat loss.

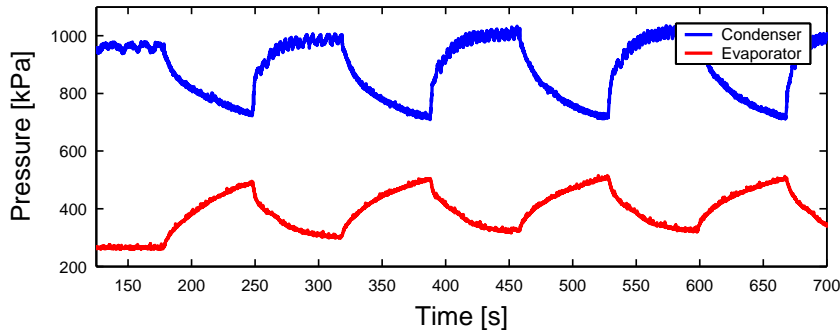


Figure 5.23 System pressure data

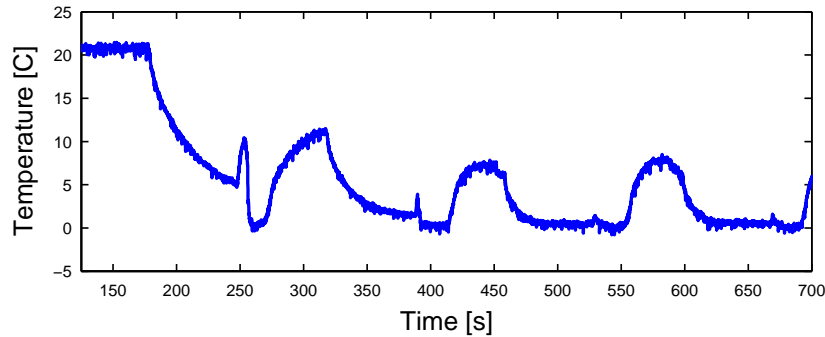


Figure 5.24 System evaporator superheat data

5.6 Future Work

Many opportunities for continued work in dynamic modeling of VCC systems are readily available. The dynamic modeling goals of greatest interest are the simulation of cycling conditions, the simulation of start-up conditions, and the improvement of the compressor mass flow rate prediction.

5.6.1 Cycling Simulation

The model output and data presented in the preceding sections showed that the current Thermosys models capture many of the qualitative features of the transient response associated with compressor cycling. However, some aspects of the data, such as the loss of the superheat in the evaporator, were not captured by the model. This loss of superheat behavior demonstrates the need for switching between model structures during simulation. Loss of superheat in a simulation should result in the evaporator model changing from a two-phase/superheat structure to two-phase only structure.

The approach presented by [38] could be applied to the Thermosys models. Some modifications to the existing models would be needed. The Thermosys models currently perform a matrix inversion at each time step to find the state derivatives. In the approach of [38], this matrix inversion is performed symbolically. This approach provides explicit expressions for the state derivatives. These expressions can then be manipulated to account for model switching numeric issues. Using this approach in Thermosys would require a significant amount of modification to the Simulink component models, but the change is not conceptually challenging. In addition to finding explicit state derivative expressions, new derivations of heat exchangers with different active fluid regions would be required. These new derivations would be very similar to both previous Thermosys derivations and derivations available in the literature. A final, and perhaps most time consuming challenge, is accurately characterizing the behavior of the expansion device and compressor at extremely low mass flow rates. But this challenge must be overcome regardless of the chosen method for dealing with compressor cycling.

5.6.2 Start-up Simulation

System start-up simulation will build upon the results of the cycling simulation efforts. Developing cycling simulation capabilities will provide the model switching structure necessary for start-up simulation as well as characterize the mass flow devices under very low flow conditions.

The additional difficulty presented by start-up simulation is the determination of the proper initial conditions. The behavior of a system during start-up is largely dependent on the location of the refrigerant charge.

The mechanisms governing the migration of charge while the system is not operating are not well understood. In addition, the migration of charge may continue over a long period of time. For example, a system's start-up transients could be significantly different if it has not been operated for one day as opposed to one week. This behavior has been observed in the experimental system described in Chapter 6.

5.6.3 Improved Compressor Mass Flow Prediction

The compressor mass flow prediction could be improved in a number of ways. One possibility is the development of a first-principles dynamic compressor model. Other moving-boundary model developers have taken this approach. Another possibility is the inclusion of oil flow modeling. The presence of oil in the compressor pistons affects the amount of refrigerant mass expelled during each compressor revolution. Oil circulation is also of interest to industry due to its effects on heat transfer and compressor reliability. A third approach is directly identifying a dynamic compressor mass flow model. This approach would be the simplest from a modeling point of view but would require the addition of a new sensor capable of measuring the mass flow rate of a fluid in the gas phase.

Chapter 6. Experimental System

The model validation results presented in this thesis were obtained using data from an experimental air-conditioning system. This chapter contains an overview of the experimental system sensors, actuators, data acquisition, and components. A detailed description of the experimental system is found in [41]. This chapter will describe significant changes to the system carried out since [41] was written.

6.1 General Description

The experimental system is a modified dual-evaporator industrial air-conditioning trainer system. The major components are two tube-and-fin evaporators, a tube-and-fin condenser, an internal heat exchanger, a liquid-line receiver, a suction-line accumulator, a semi-hermetic compressor, and a variety of expansion devices. The system is instrumented with a number of sensors, allowing for detailed observation of system transients. Manual valves allow for the selection of multiple system configurations. A schematic of the system is shown in Figure 6.1. The valve acronyms are defined in Table 6.1. The manufacturer and model number for each component are given in Table 6.2.

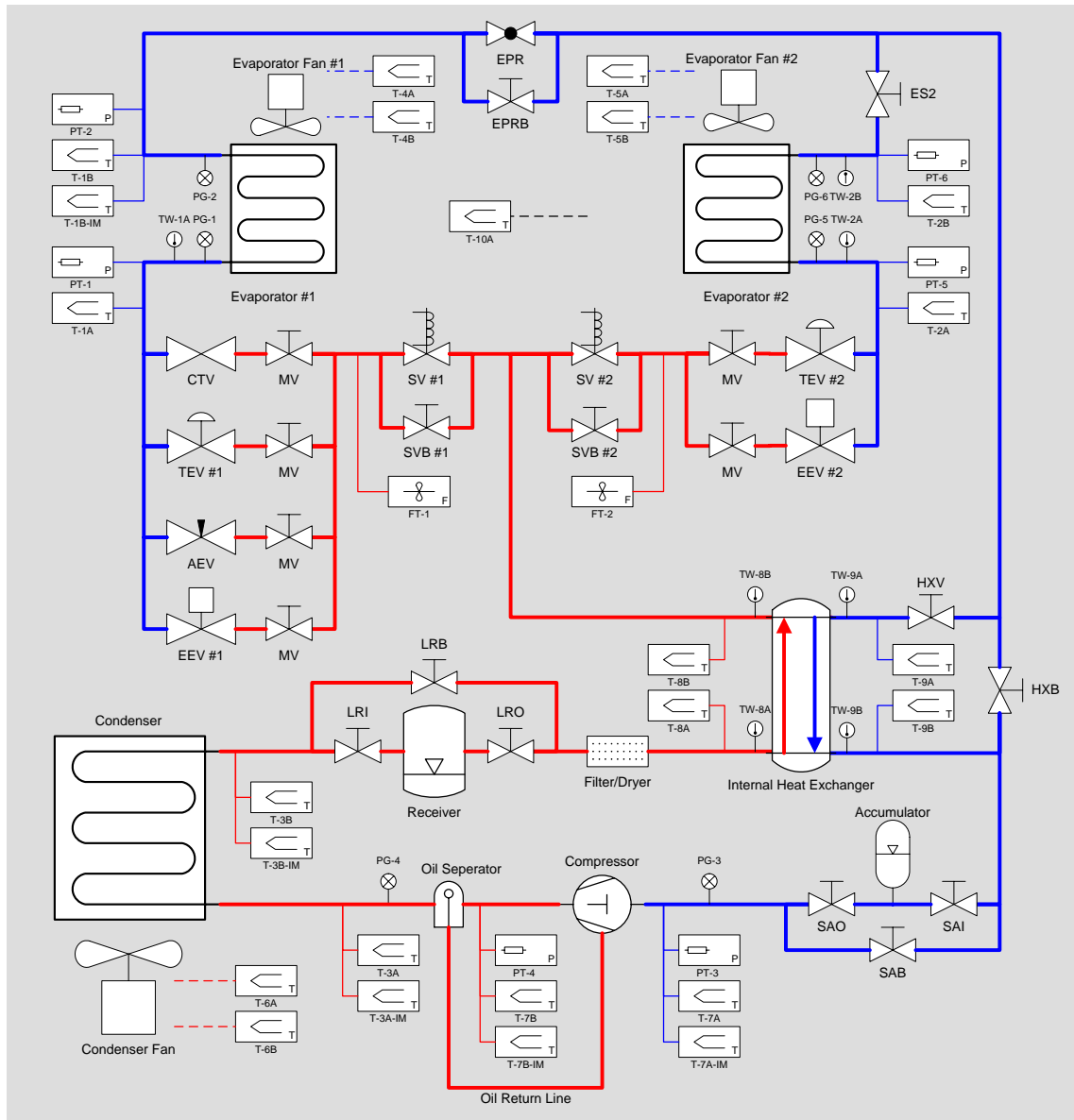


Figure 6.1 Experimental system schematic

Table 6.1 Valve acronyms and descriptions

Valve Designation	Description
CTV	Capillary Tube Valve
TEV	Thermostatic Expansion Valve
AEV	Automatic Expansion Valve
EEV	Electronic Expansion Valve
SV	Solenoid Valve
SVB	Solenoid Valve Bypass
EPR	Evaporator Pressure Regulating Valve
EPRB	Electronic Pressure Regulating Valve Bypass
ES2	Evaporator Side #2 Valve
HXV	Internal Heat Exchanger Valve
HXB	Internal Heat Exchanger Bypass

LRI	Liquid Line Receiver Inlet
LRO	Liquid Line Receiver Outlet
LRB	Liquid Line Receiver Bypass
SAI	Suction Line Accumulator Inlet
SAO	Suction Line Accumulator Outlet
SAB	Suction Line Accumulator Bypass
MV	Manual Valve

Table 6.2 Component name, manufacturer, model, and URL

Component	Manufacturer	Model	URL
Evaporator Fan and Casing	Larkin (HeatCraft)	VAK-17A	www.heatcrafttrpd.com
Evaporator #1	HeatCraft	52601301 (VAK-17A)	www.heatcrafttrpd.com
Evaporator #2	Blissfield	BH517	www.blissfield.com
Condenser and Fan	Tecumseh (Blissfield)	50803-1 (66001-3)	www.blissfield.com
Internal Heat Exchanger	Superior (Sherwood)	HXSV-1/2	www.sherwoodvalve.com
Liquid Line Receiver	AC&R Components, Inc. (Henry Tech.)	S-8064	www.henrytech.com
Suction Line Accumulator	AC&R Components, Inc. (Henry Tech.)	S-7043	www.henrytech.com
Oil Separator	AC&R Components, Inc. (Henry Tech.)	S-5581	www.henrytech.com
Compressor	Copeland	KANA-006E-TAC-800	www.copeland-corp.com
Variable Frequency Drive	Baldor	ID15J101-ER	www.baldor.com
Capillary Tubing	Sealed Unit Parts Co., Inc.	BC-4	www.supco.com
TEV	Sporlan Valve Co.	FJ ¼ C	www.sporlan.com
AEV	Parker-Hannefin	A2	www.parker.com
EEV	Sporlan Valve Co.	SEI-0.5	www.sporlan.com
EPR	Sporlan Valve Co.	ORIT 6-0/50-1/2"	www.sporlan.com
Manual Valves	Mueller Brass Co.	14838, 14841	www.muellerindustries.com
Filter-Dryer	Sporlan Valve Co.	C-052	www.sporlan.com
Sight Glasses	Sporlan Valve Co.	SA-14S, SA-12FM	www.sporlan.com
Pressure Transducers	Cole-Palmer	07356-53, 07356-54	www.coleparmer.com
Pressure Gauges	Ritchie Engineering Co., Inc.	49051, 49052	www.yellowjacket.com
Mass Flow Transducers	McMillan Company	102-6P	www.mcmflow.com
Immersion Thermocouple	Omega	GTMQSS-062U-6	www.omega.com
Welded Thermocouple	Omega	FF-T-20-100	www.omega.com
Watt Meter	Ohio Semitronics, Inc.	GW5-019D	www.ohiosemitronics.com
Pressure Switches	Ranco	010-1402, 011-1711	www.ranco.invensys.com
Line Reactors	MTE (Galco Industrial Electronics)	MTE RL-00402	www.galco.com
Analog Input Board	Measurement Computing, Inc.	PCI-DAS1200/JR	www.measurementcomputing.com
Analog Output Board	Measurement Computing, Inc.	PCI-DDA-08/12	www.measurementcomputing.com
Thermocouple Board	Measurement Computing, Inc.	PCI-DAS-TC	www.measurementcomputing.com
Signal Conditioners	Omega	OM5 Series	www.omega.com
Humidifier	Hunter	33222	www.hunterfan.com

6.2 Sensors

The experimental system is equipped with sensors to measure temperatures, pressures, mass flow rates, power, and humidity. Table 6.3 gives the location of these sensors on the system.

Table 6.3 Sensor designations and locations

Surface Thermocouple	Immersion Thermocouple	Thermowell	Location
T-1A		TW-1A	Evaporator #1 Inlet
T-1B	T-1B-IM	TW-1A (removed)	Evaporator #1 Outlet
T-2A		TW-2A	Evaporator #2 Inlet
T-2B	T-2B-IM	TW-2B (removed)	Evaporator #2 Outlet
T-3A	T-3A-IM	TW-3A (removed)	Condenser Inlet
T-3B	T-3B-IM	TW-3B (removed)	Condenser Outlet
T-4A			Evaporator #1 Air Inlet
T-4B			Evaporator #1 Air Outlet
T-5A			Evaporator #2 Air Inlet
T-5B			Evaporator #2 Air Outlet
T-6A			Condenser Air Inlet
T-6B			Condenser Air Outlet
T-7A	T-7A-IM	TW-7A (removed)	Compressor Inlet
T-7B	T-7B-IM	TW-7B (removed)	Compressor Outlet
T-8A		TW-8A	Internal Heat Exchanger – Liquid Inlet
T-8B		TW-8B	Internal Heat Exchanger – Liquid Outlet
T-9A		TW-9A	Internal Heat Exchanger – Vapor Inlet
T-9B		TW-9B	Internal Heat Exchanger – Vapor Outlet
T-10A			Ambient
Pressure Transducer	Pressure Gage	Flow Transducer	Location
PT-1	PG-1		Evaporator #1 Inlet
PT-2	PG-2		Evaporator #1 Outlet
PT-3	PG-3		Compressor Inlet
PT-4	PG-4		Compressor Outlet
PT-5	PG-5		Evaporator #2 Inlet
PT-6	PG-6		Evaporator #2 Outlet
		FT-1	Expansion Device #1 Inlet
		FT-2	Expansion Device #2 Inlet
Humidity Sensors			Location
RH-1			Evaporator #2 Air Inlet
RH-2			Evaporator #2 Air Outlet

6.2.1 Temperature, Pressure, Mass Flow, and Power Measurement

Temperature measurements are obtained with type T thermocouples. Welded tip thermocouples are used for air temperature and surface temperature measurements. Ungrounded, stainless steel sheathed thermocouples are used for immersed refrigerant measurement. Pressure measurements are obtained with strain-gage based pressure sensors. These sensors are located at the inlet and outlet of each evaporator and the compressor. Liquid mass flow is measured before the inlet to each valve array by turbine-based meters. Power consumed by the compressor or the heat exchanger fans is measured with an AC watt-transducer.

6.2.2 Humidity Measurement

To validate new heat exchanger models that incorporate humidity calculations, two humidity sensors were added to the experimental system. The sensors were placed at the inlet and outlet of the second evaporator.

The inlet sensor is a Honeywell model HIH-3610, and the outlet sensor is a Honeywell model HIH-4000. Each sensor consists of a thermoset polymer capacitive sensing element with on-chip integrated signal conditioning. They are powered by the data acquisition computer's 5 V power supply and provide a voltage output as a function of relative humidity. Using a manufacturer specified curve, the voltage output is converted to relative humidity. The conversion includes temperature compensation for deviations from the calibration temperature, 25°C. The HIH-3610 conversion is given in Equation 6.1. The HIH-4000 conversion is given in Equation 6.2. The HIH-3610 has a stated accuracy of 2% relative humidity. The HIH-4000 claims 3.5% relative humidity accuracy. Figure 6.2 shows the inlet relative humidity sensor; the outlet sensor is very similar in appearance. The sensors are approximately 4.27 mm by 9.47 mm by 2.03 mm in size.

$$\phi_{in} = \frac{\frac{1}{0.0062} \left(\frac{V_{out}}{V_{supply}} - 0.16 \right)}{1.0546 - 0.00216T_{air,in}} \quad (6.1)$$

$$\phi_{out} = \frac{V_{out} - (0.9237 - 0.0041T_{air,out} + 0.000040T_{air,out}^2)}{0.0305 + 0.000044T_{air,out} - 0.0000011T_{air,out}^2} \quad (6.2)$$



Figure 6.2 Photograph of the relative humidity sensor at the evaporator inlet

6.3 Actuators

The experimental system is designed for computer control of compressor speed, fan speeds, and electronic expansion valve opening. The other expansion devices operate as mechanical feedback devices or with no control.

6.3.1 Compressor, Fans, and Valves

The compressor is a semi-hermetic reciprocating machine. The pistons are driven by a crankshaft which is connected directly to an electric motor in the compressor shell. Compressor speed control is achieved with a variable frequency drive (VFD). The VFD converts single phase 120 VAC to the three-phase 240 VAC required by the compressor. The VFD uses pulse width modulation to control the compressor speed.

The three heat exchanger fans are powered by fan control boards than take in a DC command signal and output an AC signal to the fan motor. Air mass flow rate maps were generated by measuring the average air velocity over a range of locations and fan speeds.

The experimental system may be configured to use one of four expansion devices: an electronic expansion valve (EEV), a thermostatic expansion valve (TEV), an automatic expansion valve (AEV), and a capillary tube. The EEV uses a stepper motor to vary the size of the valve opening. The stepper motor is computer controlled, allowing the EEV to be used in feedback control schemes. The TEV uses a thermo-mechanical feedback system to regulate superheat at the evaporator outlet. The AEV regulates the evaporator at a constant pressure. Unlike the other three expansion devices, which incorporate variable area valves, the capillary tube geometry is fixed. It is therefore the simplest expansion device, but also the most limited in capabilities.

6.3.2 Humidifier

Validation of the humidity models requires the experimental system to run under conditions in which condensation occurs on the external evaporator surfaces. During drier seasons of the year, condensation will not naturally occur, and the relative humidity of the air entering the evaporator must be artificially raised to ensure that condensation will occur. To achieve elevated inlet air relative humidity, a small room humidifier was added to the system. The humidifier is a model 33222 from Hunter. The output of the humidifier is ducted directly to the evaporator inlet where it is mixed with room air before entering the evaporator, as shown in Figure 6.3. The humidifier has three speed settings, allowing for model validation to include step changes in inlet relative humidity.



Figure 6.3 Humidifier and tubing bringing moist air output to the evaporator inlet

6.4 Data Acquisition

Data acquisition and control are carried out with a 16 channel thermocouple board, an 8 channel 12-bit analog output board, and a 16 channel 12-bit analog input board from Measurement Computing. Models are interfaced with a PC using WinCon and the Real Time Workshop. For details on the wiring and the individual components of the data acquisition system, see [26].

6.5 Components

The experimental system contains four heat exchangers and a number of auxiliary components.

6.5.1 Heat Exchangers

Both evaporators are tube-and-fin models with copper tubes and aluminum fins. The first evaporator is a VAK17A from Larkin. The second evaporator is similar in size to the first evaporator, but has an alternative tube configuration. In the first evaporator, fluid enters at the top of the heat exchanger, flows back and forth down the front face, and then flows back and forth up the back face to exit at the top. This configuration effectively gives the first evaporator a “two-slab” configuration. Because this configuration is more difficult to model in the Thermosys framework, a “single-slab” design was chosen for the second evaporator. In this tube configuration, refrigerant enters at the top and exits at the bottom, flowing back and forth as it descends. The second evaporator was provided by Blissfield Manufacturing Company. The model validation results presented in this work were obtained from tests using the second evaporator.

The condenser, Tecumseh model #50803-1, is also a tube-and-fin design. Both the tubes and the fins are steel.

The internal heat exchanger is a Superior model HXSV-1/2. This component facilitates heat exchange between cold vapor exiting the evaporator and hot liquid exiting the condenser or the receiver. The internal heat exchanger makes it less likely that liquid will enter the compressor and two-phase flow will enter the expansion device, thus preventing slugging and choking. This component was not used for the tests described herein.

6.5.2 Auxiliary Components

The experimental system contains a receiver at the condenser outlet and an accumulator at the evaporator outlet. Both components are manufactured by AC&R Components, Inc. The receiver is a model S-8064 and the accumulator is a model S-7043. The receiver stores excess refrigerant charge and ensures that flow into the valve will not be two-phase. The accumulator captures liquid in the suction line, allowing only vapor to flow to the compressor. In the model validation tests presented in the next chapter, the receiver and the accumulator are both included in the system. However, the accumulator is not included in the models because it only contains vapor and therefore acts as an additional pipe volume.

The other auxiliary components are an oil separator, a filter/dryer, sight glasses, and hand valves. The oil separator, a model S-5581 from AC&R Components, captures oil from the discharge line and returns it to the compressor. The Sporlan C-052 Catch-All filter-dryer removes potentially damaging moisture, acids, and particulates from the system. This component is located between the receiver and the valves. At various locations throughout the system, sight glasses are included for visual monitoring of the fluid condition. The sight glasses contain a color-changing element that serves as an indication of excessive moisture in the system. Sporlan See-All

models SA-12FM and SA-14S are used. Manual valves (Mueller models 14838 and 14841) are used to isolate various sections of the system. They allow for multiple system configurations, such as single evaporator and dual evaporator operation.

6.6 Physical Parameters

Each component used in model validation must be characterized by physical parameters. Table 6.4 below shows the baseline physical parameter values for the components used in model validation simulations. They were obtained through a combination of manufacturer provided technical drawings and measurements of components.

Table 6.4 Component physical parameters used for model validation simulations

Component	Parameter	Value	Units	Comments
Condenser	Heat Exchanger Mass	4.656	kg	Calculated
	Heat Exchanger Specific Heat	0.467	kJ/kg-K	Steel
	Heat Exchanger Frontal Area	0.0898	m ²	From Manufacturer
	Hydraulic Diameter of Tubes	0.008103	m	Measured
	Internal Volume	0.00055716	m ³	From Manufacturer
	Internal Surface Area	0.274993	m ²	Calculated
	External Surface Area	2.7927	m ²	Calculated
	Total Fluid Flow Length	10.6895	m	Calculated
	Flow Cross Sectional Area	0.00005156	m ²	Calculated
	Receiver Volume	0.0007732	m ³	Measured
Evaporator 2	Heat Exchanger Mass	2.7438	kg	Calculated
	Heat Exchanger Specific Heat	0.4877	kJ/kg-K	Aluminum and Copper
	Heat Exchanger Frontal Area	0.0584	m ²	Calculated
	Hydraulic Diameter of Tubes	0.0081026	m	From Manufacturer
	Internal Volume	0.000591	m ³	From Manufacturer
	Internal Surface Area	0.29166	m ²	Calculated
	External Surface Area	3.068	m ²	Calculated
	Total Fluid Flow Length	11.45794	m	Calculated
	Flow Cross Sectional Area	0.00005156	m ²	Calculated
	Accumulator Volume	0.0028665	m ³	Measured
EEV	Rising Slew Rate	12.5	%/s	From Manufacturer
	Falling Slew Rate	-12.5	%/s	From Manufacturer
	Input Delay	0.5	s	Estimated
Compressor	Volume	0.0000304	m ³	From Manufacturer
	Rising Slew Rate	1000	rpm/s	Estimated
	Falling Slew Rate	-1000	rpm/s	Estimated
Pipe Length	Compressor to Condenser	4.04	m	Measured
	Condenser to Valve	4.79	m	Measured
	Valve to Evaporator	1.63	m	Measured
	Evaporator to Compressor	6.53	m	Measured
	Hydraulic Diameter	9.5	mm	Estimated

Chapter 7. Model Validation

This chapter addresses one of the key challenges of the model development process, model validation. While a model cannot be validated by a finite amount of data, the model user's confidence in the model may be increased through the model validation process. In this chapter, particular attention will be paid to the validation of the modeling techniques discussed in previous chapters, namely, the addition of semi-empirical modeling tools, the incorporation of heat exchanger with receiver/accumulator models, the use of a dynamic compressor mass flow correction, and the incorporation of humidity in the evaporator model. Extensive model validation has been lacking in the moving-boundary literature, as demonstrated in [41]; this work attempts to increase confidence in the moving-boundary modeling approach by presenting numerous comparisons of experimental data and simulation output. Model validation results are presented for three test scenarios: single-step validation, drive cycle validation, and atmospheric conditions validation.

7.1 Single-Step Model Validation Scenario

The single-step model validation scenario serves two main purposes: the validation of the condenser with receiver model and the validation of the semi-empirical modeling tools. The system identification technique for compressor mass flow correction was also applied to this validation scenario in a separate set of simulations. The experimental system was used to generate data containing a relatively small step in each of the system actuators. The liquid receiver at the condenser outlet was included in the experimental system, necessitating the use of the condenser with receiver component model. To quantify the accuracy improvements obtained through the use of the semi-empirical modeling and dynamic mass flow correction tools, the model outputs of various system simulations were compared. Each system simulation used a different subset of the available modeling tools.

7.1.1 System Inputs

Data was taken from the experimental system described in Chapter 6. Step inputs were applied to the compressor speed, the valve opening, the condenser fan speed, and the evaporator fan speed, as summarized in Table 7.1. Plots of the inputs are shown in Figure 7.1 through Figure 7.4.

Table 7.1 Summary of inputs used in the single-step validation scenario

Input	Step Time	Before Step	After Step	Percent of Range
Valve Open Command	1000 s	13	14.5	9.4 %
Compressor RPM	1400 s	1600 RPM	1800 RPM	14.3 %
Condenser Air Mass Flow	1800 s	0.2938 kg/s	0.2858 kg/s	2.7 %
Evaporator Air Mass Flow	2200 s	0.1568 kg/s	0.1363 kg/s	13.1 %

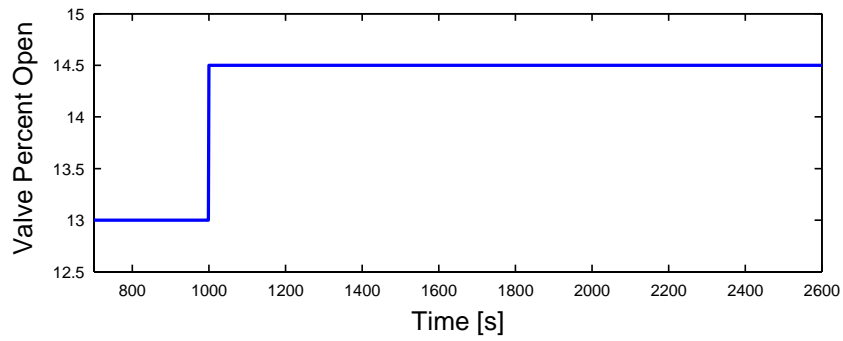


Figure 7.1 Valve input signal

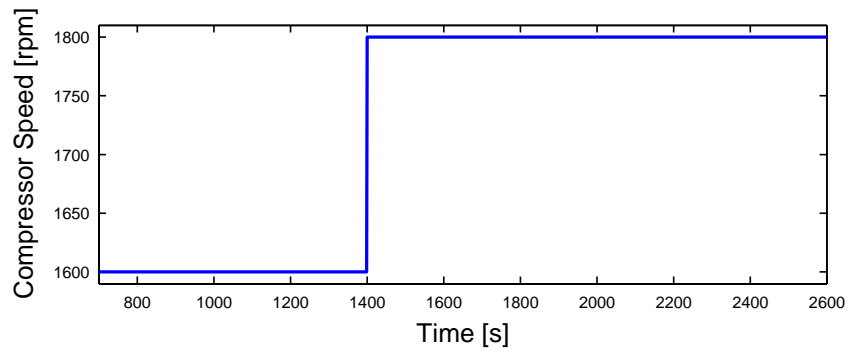


Figure 7.2 Compressor input signal

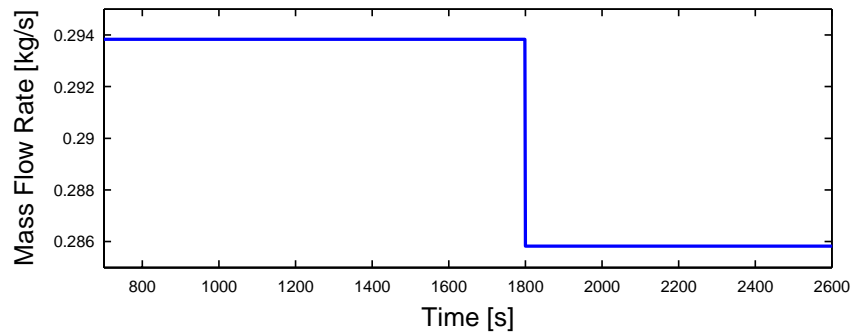


Figure 7.3 Condenser air mass flow rate input signal

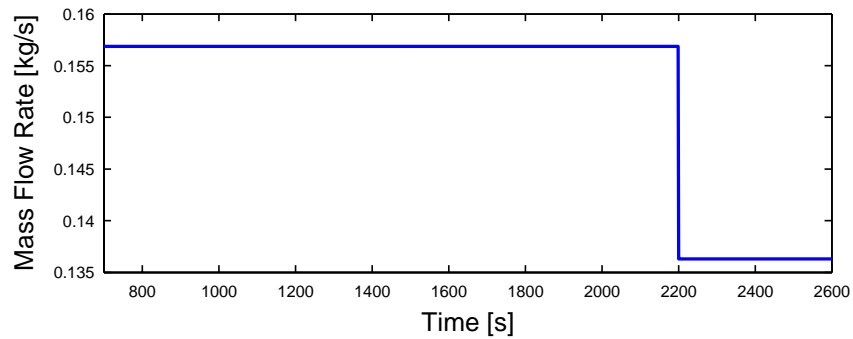


Figure 7.4 Evaporator mass flow rate input signal

7.1.2 System Output

Before presenting the model validation results, it should be noted that tables containing the user-specified initial conditions for each component are found in Appendix B for each validation scenario discussed in this chapter. Refer to [41] for a complete description of the physical parameters and initial conditions associated with each component. Two parameters, the air-side heat transfer coefficient and the cross-sectional area for refrigerant flow, merit additional discussion.

The initial value of the air-side heat transfer coefficient was determined by two methods to examine the effect of the j factor semi-empirical modeling technique. When the j factor semi-empirical approach was used, the initial condition for the air-side heat transfer coefficient was calculated from the j factor based on the user-supplied air mass flow rate and inlet air temperature. When the j factor approach was not used, the model steady-state solver calculated an initial air-side heat transfer coefficient based on the assumption that the lumped air temperature was the mean of the user-supplied inlet air temperature and outlet air temperature.

The equivalent pipe cross-sectional area was also considered to be a tunable physical parameter. This parameter has a significant effect on the general speed of response of the heat exchanger models. Model validation results demonstrated that a cross-sectional area larger than that calculated from the heat exchanger tube diameter was necessary to match the model response speed with the data response speed, particularly in the pressure output. Increasing the cross-sectional area effectively increases the volume of the heat exchanger equivalent pipe model. Considering that the pipe lengths between components participate in the pressure dynamics and are not currently modeled to account for those pressure dynamics, it is logical to include the volume of the pipes in the heat exchanger models. Table 7.2 shows estimates of the heat exchanger cross-sectional areas that could be used to account for the pipe volume by lumping it into the heat exchanger volumes. The cross-sectional areas are found by dividing the total high-side and low-side volumes by the condenser flow length and the evaporator flow length, respectively. The modified condenser cross-sectional area is approximately seven times larger than the tube cross-sectional area. The modified evaporator cross-sectional area is approximately three times larger than the tube cross-sectional area. Increased cross-sectional area values were used to generate all model validation results presented in this chapter.

Table 7.2 Cross-sectional areas based on total high-side and low-side volumes

High-Side (Condenser)		Low-Side (Evaporator 2)	
Component Volumes [m^3]			
Condenser	0.00055716	Evaporator	0.000590806
Receiver	0.002866511	Accumulator	0.000773225
Condenser to Valve Pipe	0.000339354	Compressor to Evaporator Pipe	0.000462626
Compressor to Condenser Pipe	0.000286219	Valve to Evaporator Pipe	0.000115479
Total Volume	0.004049243	Total Volume	0.001942137
Heat Exchanger Lengths [m]			
Condenser	10.6895493	Evaporator	11.4582
Cross-Sectional Areas [m^2]			
Condenser	0.000378804	Evaporator	0.000169498

7.1.2.1 Semi-empirical Results

Figure 7.5 through Figure 7.9 compare the experimental data with model output from a model utilizing all of the semi-empirical modeling techniques. The major dynamic effects associated with each input step are captured in the model outputs. The condenser with receiver model outputs match the system data very well, giving increased confidence in the receiver/accumulator modeling approach presented in Chapter 5. It should be noted that for these smaller transients the condenser with receiver model does not suffer from the same numerical problems encountered in the shut-down simulations presented in Chapter 5. The evaporator pressure prediction is less accurate, a result that is consistent across all model validation scenarios. The inaccuracy in the evaporator model is attributed to the fact that the evaporator model is more sensitive to errors in the compressor mass flow rate prediction. In addition, the evaporator on the experimental system is mounted on a plate in such a way that air flow out of the evaporator is restricted. The effects of the resulting changes in air flow patterns and temperatures in the evaporator cannot be captured by the model.

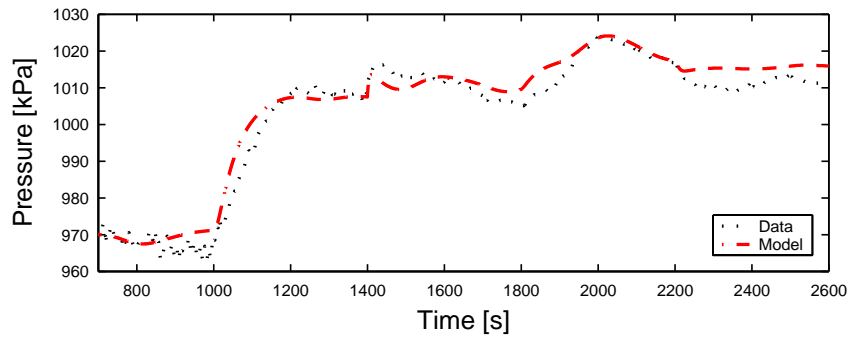


Figure 7.5 Condenser with receiver pressure

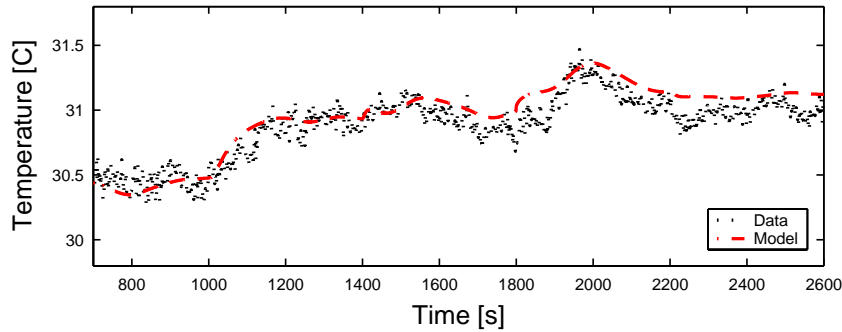


Figure 7.6 Condenser with receiver outlet air temperature

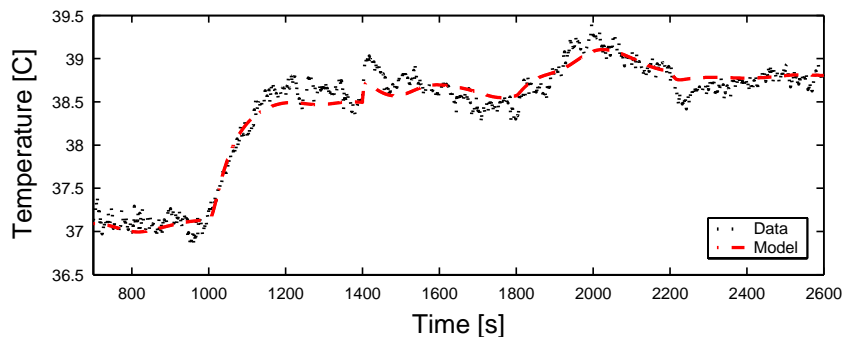


Figure 7.7 Condenser with receiver refrigerant outlet temperature

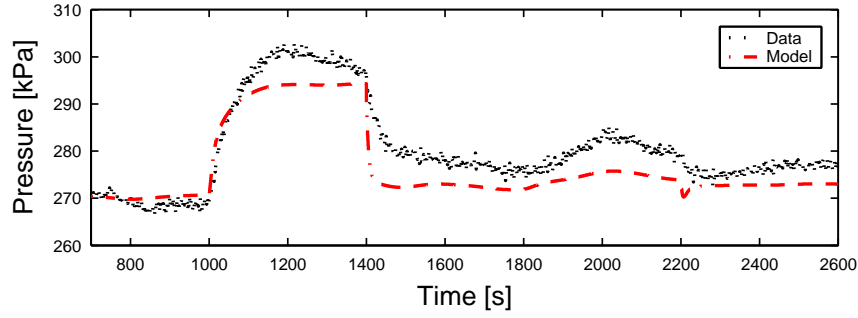


Figure 7.8 Evaporator pressure

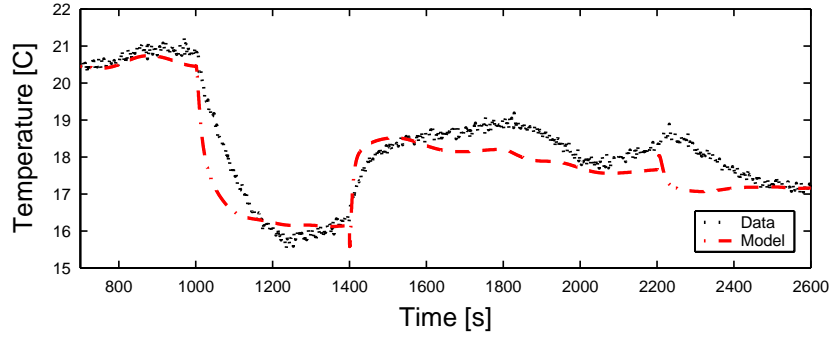


Figure 7.9 Evaporator superheat

7.1.2.2 Mass Flow Correction Results

Although this validation scenario was not the original motivation for the development of the system identification mass flow correction method, the method was also applied to the single-step validation models. The input to the ILC algorithm was the evaporator pressure error. The mass flow correction isolated by the ILC algorithm was modeled as shown in Equation 7.1, where G_1 , G_2 , and G_3 are the transfer functions defined in Equation 7.2 through Equation 7.4. The transfer function inputs were deviations from the initial values of compressor inlet pressure, outlet pressure and speed.

$$\dot{m}_{k,correction} = \begin{bmatrix} G_1 & G_2 & G_3 \end{bmatrix} \begin{bmatrix} \Delta P_{in} \\ \Delta P_{out} \\ \Delta \omega_k \end{bmatrix} \quad (7.1)$$

$$G_1 = \frac{8.698 \cdot 10^{-7} s + 9.014 \cdot 10^{-7}}{s + 0.07181} \quad (7.2)$$

$$G_2 = \frac{-4.893 \cdot 10^{-8} s - 4.923 \cdot 10^{-8}}{s + 0.01232} \quad (7.3)$$

$$G_3 = \frac{1.591 \cdot 10^{-7} s + 1.659 \cdot 10^{-7}}{s + 0.08469} \quad (7.4)$$

The transfer functions were generated using the MATLAB System Identification Toolbox. The model structure was the linear time-invariant output error model described in [32]. The metric for comparison is the percentage of output variations captured by the model. The models and their model fit metric values are shown in

Table 7.3. Using the principle of parsimony [3], the first order model was chosen as a desirable tradeoff between accuracy and simplicity since its accuracy was similar to higher order models.

Table 7.3 Comparison of model fit values

Model Order	Model Fit Metric
First	71.95
Second	75.54
Third	74.34

Figure 7.10 below compares the original static volumetric efficiency performance map with the volumetric efficiency data points obtained from the dynamically corrected compressor mass flow rate. The periods of relatively steady-state conditions are clustered around the performance map. The lowest volumetric efficiency is approximately 0.7 and corresponds to the mass flow rate immediately following a step change in the compressor speed. This point shows a large deviation from the steady-state performance map. While the volumetric efficiency is not necessarily the source of the model errors, examining it in this fashion demonstrates the dynamic nature of the modeling challenge addressed by the system identification approach.

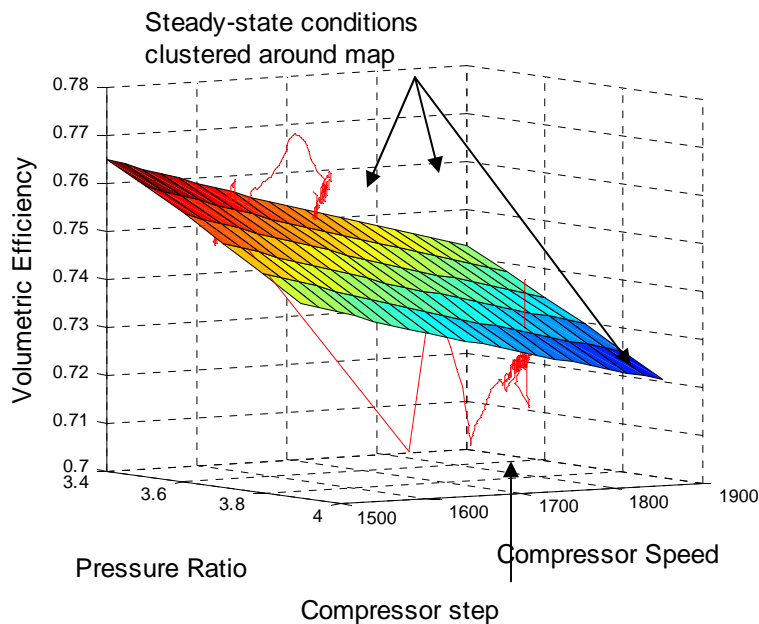


Figure 7.10 Static volumetric efficiency map (surface) and volumetric efficiency generated from mass flow correction (line)

The plots shown below in Figure 7.11 through Figure 7.15 compare a base model and a best model to the system data. The base model did not use the dynamic mass flow correction or the j factor semi-empirical heat transfer coefficient model. The best model incorporated both of these modeling tools. Applying the dynamic mass flow correction and the j factor significantly improves the evaporator pressure prediction (Figure 7.13). The condenser pressure prediction also improves slightly (Figure 7.11), and the outlet air temperatures remain nearly unchanged (Figure 7.12 and Figure 7.14). The majority of the difference between the base and best models is

attributed to the dynamic mass flow correction, as demonstrated by the quantitative results presented in the following section. These results demonstrate the high sensitivity from the evaporator outlet mass flow model input to the evaporator pressure model output. The effect of modifying the compressor mass flow rate is much more pronounced in the evaporator than in the condenser. The evaporator superheat plot (Figure 7.15) actually shows a decrease in accuracy for the best model. Recognizing that the superheat model output is closely tied to the evaporator pressure model output and that the pressure model output of the best model is very accurate, the clear conclusion is that errors must be present in the other component of the superheat prediction, the evaporator refrigerant outlet temperature.

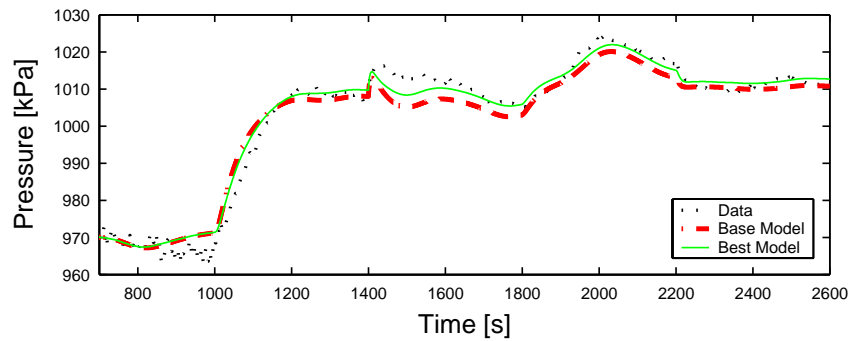


Figure 7.11 Condenser pressure

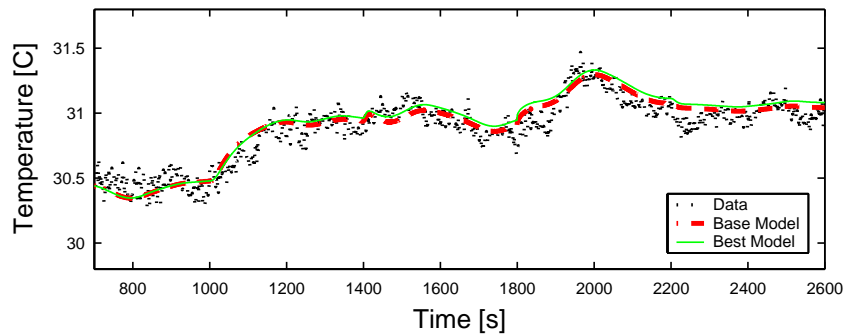


Figure 7.12 Condenser air outlet temperature

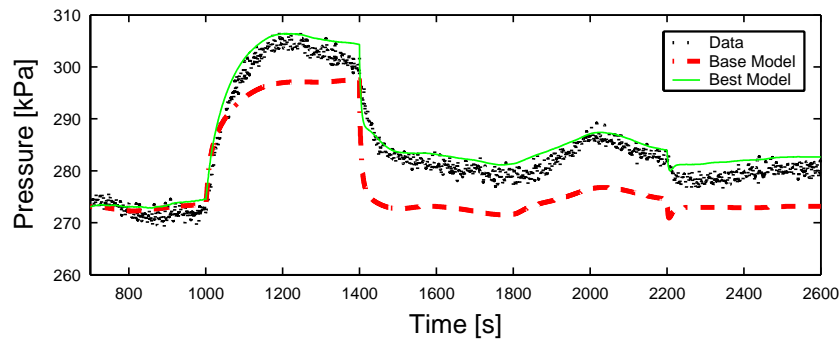


Figure 7.13 Evaporator pressure

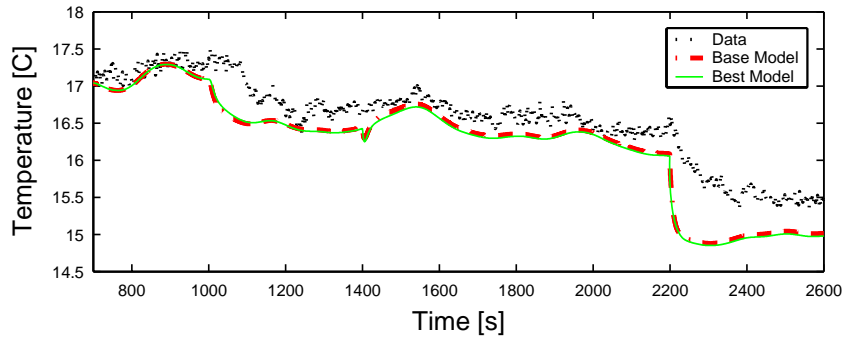


Figure 7.14 Evaporator air outlet temperature

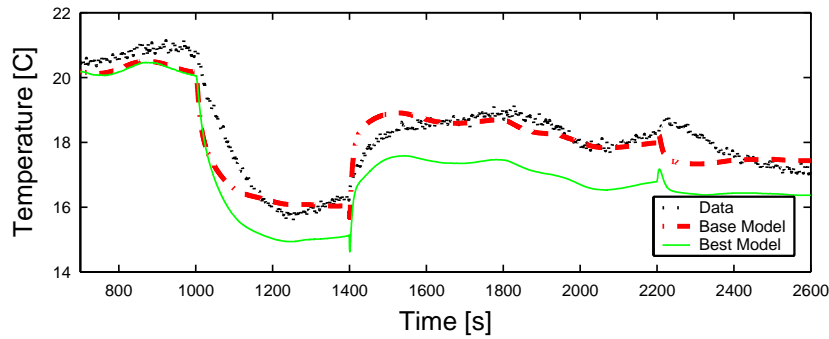


Figure 7.15 Evaporator superheat

7.1.3 Quantified Modeling Improvements

7.1.3.1 Semi-empirical Accuracy Improvements

For the initial single-step model validation, the RMS error was chosen as the metric for comparing the models that did and did not use the semi-empirical modeling techniques. As this validation scenario represented the initial attempt at implementing the condenser with receiver model, the condenser pressure was chosen as the output of interest for RMS error comparisons. The system simulation was run in six configurations. The base model contained none of the semi-empirical modeling improvements described in Chapter 3, namely the j factor and the mass flow component maps. The other simulation models used various combinations of the semi-empirical modeling techniques. The condenser pressure RMS error and percent reduction in RMS error for each simulation are summarized in Table 7.4.

Table 7.4 RMS error and RMS error reduction in the condenser pressure

Semi-empirical models in system	RMS Error	Percent Change in RMS Error from Base Model
Base—no semi-empirical models	7.55	--
Evaporator j factor	7.41	1.84
Condenser j factor	7.16	5.17
Condenser and Evaporator j factor	7.03	6.97
Valve and Compressor mass flow	6.02	20.31
All semi-empirical models—mass flow and j factor	5.62	25.64

Table 7.4 shows that, as expected, the largest error reduction comes from incorporating all of the semi-empirical modeling techniques. The largest individual error reduction comes from including the detailed valve and compressor performance maps generated from experimental system components. Validation results consistently demonstrate that accurate refrigerant mass flow rate prediction is essential to system level model accuracy.

7.1.3.2 Mass Flow Correction Accuracy Improvements

The effect of the dynamic mass flow correction method was also quantitatively compared to the effect of the j factor semi-empirical model. A new error metric was defined to capture the impact of the two modeling techniques on multiple model outputs, as shown in Equation 7.5. The chosen model outputs are those judged to be of greatest importance in control design: evaporator pressure, condenser pressure, evaporator superheat, and evaporator outlet air temperature.

$$ErrorMetric = \left(\alpha_1 \|e_{Pe}\|_{\infty}^2 + \alpha_2 \|e_{Pc}\|_{\infty}^2 + \alpha_3 \|e_{Tesh}\|_{\infty}^2 + \alpha_4 \|e_{Teao}\|_{\infty}^2 \right)^{1/2} \quad (7.5)$$

The weighting terms, α_1 through α_4 , are used to normalize by the mean value of each output. Table 7.5 gives the scaling factor values. Table 7.6 summarizes the percent reduction in the error metric achieved by using both the mass flow correction and the j factor modeling techniques. By far, the largest percentage error reductions come from incorporating the dynamic mass flow correction, again showing the importance of accurate mass flow prediction. The gains from incorporating the j factor are marginal compared to those from incorporating the dynamic mass flow correction.

Table 7.5 Error metric scaling factors

Scaling Factor (1/mean)	
α_1	0.003597
α_2	0.000998
α_3	0.055301
α_4	0.061596

Table 7.6 Error metric and error metric improvement

Model	Error Metric	Percent Improvement
Base-no j factor, no dynamic mass flow correction	1.3167	--
Dynamic mass flow correction	0.8523	35.2720
Dynamic mass flow correction and condenser j factor	0.8521	35.2878
Dynamic mass flow correction and evaporator j factor	0.8118	38.3479
Dynamic mass flow correction, condenser and evaporator j factor	0.8109	38.4179

7.2 Drive Cycle Model Validation Scenario

The drive cycle validation scenario is based on a standard EPA emissions test, the SFTP-SCO3 [16]. This test is of interest because it specifies that the vehicle air conditioning system must be operating while tailpipe emissions are measured. Therefore the efficiency of the air conditioner becomes critical for a vehicle to perform

well on the test. The large and numerous changes in system inputs also provide a more challenging validation scenario than the single step inputs.

7.2.1 System Inputs

The inputs were used on the experimental system described in Chapter 6 to mimic an automotive air conditioning system operating during the SFTP-SCO3 test. The compressor input was generated with ADVISOR [41] by assuming a small vehicle transmission and converting the test-specified vehicle speed to a compressor speed. The experimental system condenser fan speed was modulated to recreate the condenser mass flow rate associated with the vehicle speed. Finally, the valve opening was varied by a PID controller regulating the evaporator superheat. The evaporator air mass flow rate was held at a fixed value.

The maximum and minimum values of the drive cycle inputs are given in Table 7.7. As seen in the table, the percent of actuator range covered by these inputs is much larger than that of the single-step validation scenario. In addition, as seen in Figure 7.16 through Figure 7.18, there are numerous input variations and they frequently occur simultaneously, furthering adding to the challenging nature of this validation scenario.

Table 7.7 Table of inputs for the drive cycle validation scenario

Input	Minimum Value	Maximum Value	Percent of Range
Valve Open Command	8.9443	17.8997	56.0 %
Compressor RPM	1000 RPM	2146 RPM	81.9 %
Condenser Air Mass Flow Rate	0.2539 kg/s	0.2957 kg/s	14.1 %

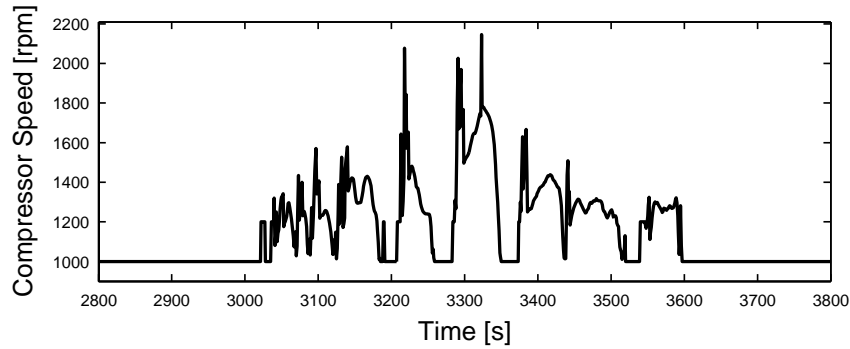


Figure 7.16 Compressor speed

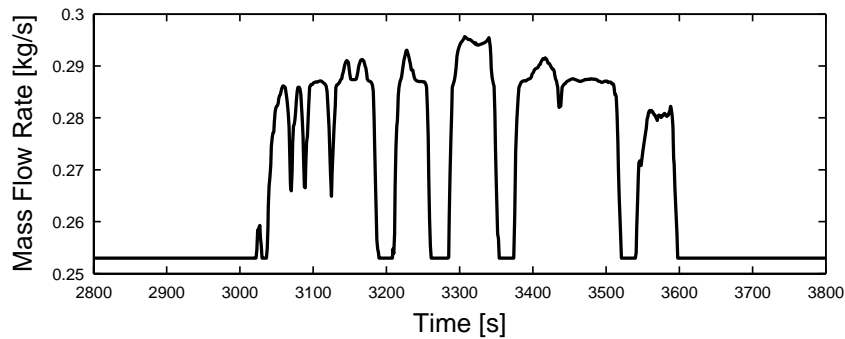


Figure 7.17 Condenser air mass flow rate

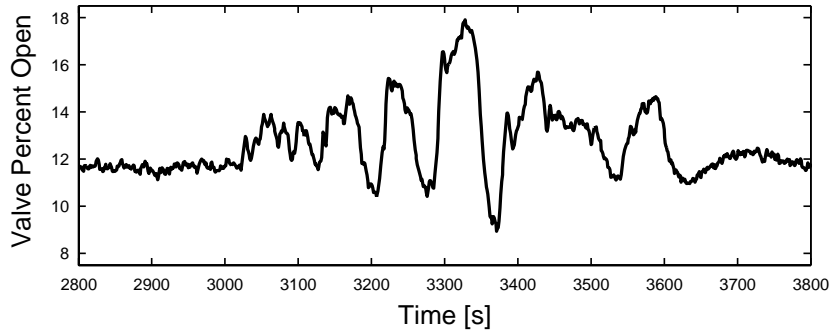


Figure 7.18 Valve opening

7.2.2 System Outputs

Figure 7.19 through Figure 7.24 compare experimental system data to models with and without the dynamic mass flow correction. The motivation for developing the system identification mass flow correction technique was the poor evaporator pressure prediction evident in Figure 7.22. There is a very notable improvement in evaporator pressure prediction after applying the mass flow correction. Besides the evaporator superheat, which is closely tied to evaporator pressure, the other model outputs are not significantly impacted by modifying the compressor mass flow rate.

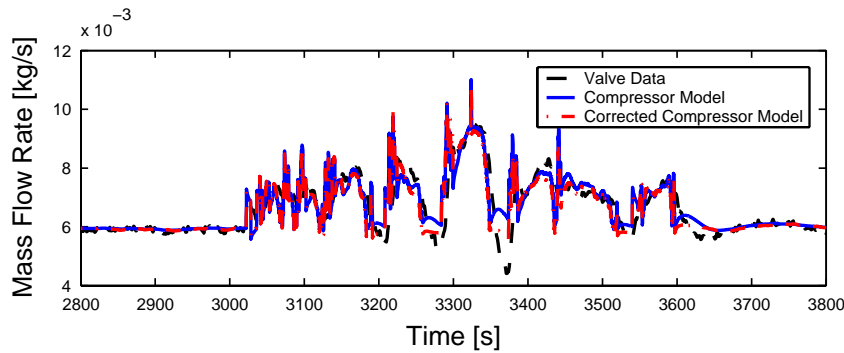


Figure 7.19 Valve mass flow data and compressor mass flow models

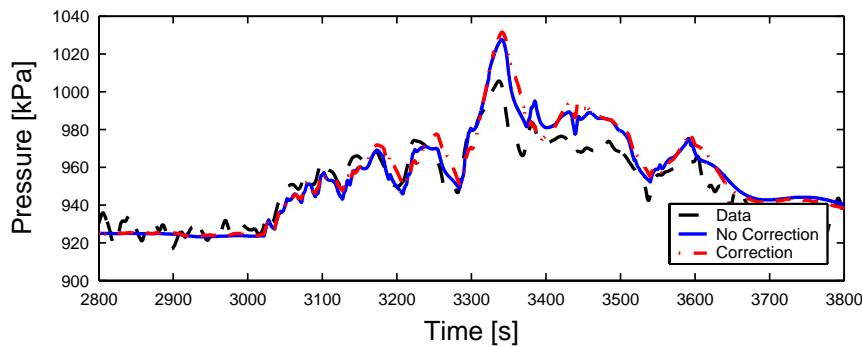


Figure 7.20 Condenser pressure data and models

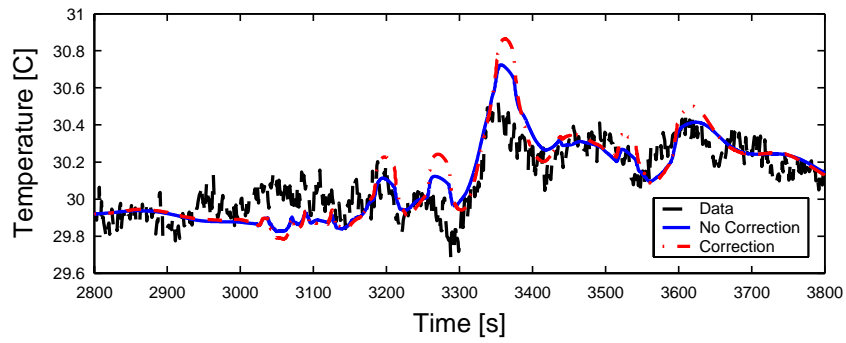


Figure 7.21 Condenser outlet air temperature data and models

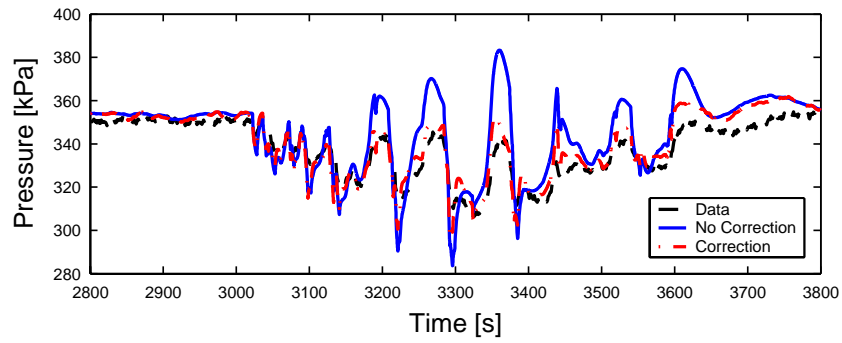


Figure 7.22 Evaporator pressure data and models

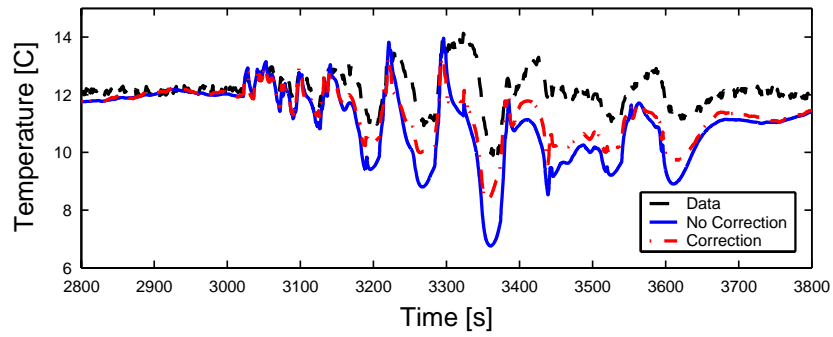


Figure 7.23 Evaporator superheat data and models

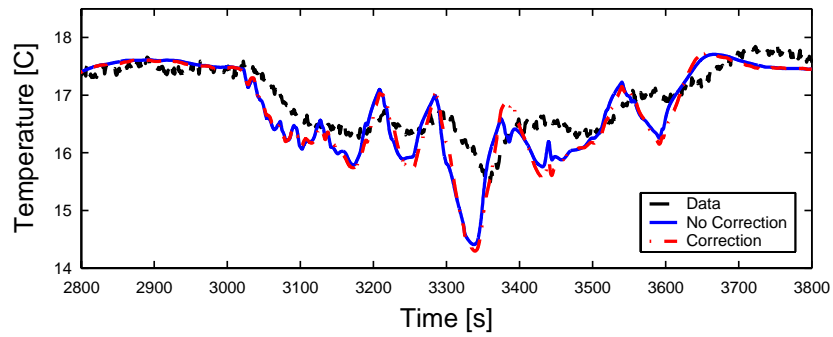


Figure 7.24 Evaporator outlet air temperature data and models

The mass flow correction factor is defined in Equation 7.6, where G_1 and G_2 are the transfer functions given in Equation 7.7 and Equation 7.8. The transfer functions were generated with the MATLAB System Identification Toolbox. The model structure is the ARMAX model described in [32]. The inputs to the correction model are the deviations from the initial conditions of compressor speed and valve opening. These inputs were chosen because they are the cause of most dynamic events in the system. However, using these inputs required the selection of a high-order model to capture the dynamics isolated by the ILC algorithm. For reasons of minimizing model complexity, the inputs used in the single-step validation scenario (compressor inlet pressure, outlet pressure, and speed) are probably more advantageous than the inputs used here.

$$\dot{m}_{k,correction} = [G_1 \quad G_2] \begin{bmatrix} \Delta\omega_k \\ \Delta Valve \end{bmatrix} \quad (7.6)$$

$$G_1 = \frac{-7 \times 10^{-11} s^3 - 2.8 \times 10^{-10} s^2 - 5.1 \times 10^{-10} s - 4 \times 10^{-10}}{s^4 + 0.111s^3 + 0.109s^2 + 0.0045s + 0.00056} \quad (7.7)$$

$$G_2 = \frac{5.4 \times 10^{-8} s^3 + 1.57 \times 10^{-7} s^2 + 1.33 \times 10^{-7} s - 4.4 \times 10^{-8}}{s^4 + 0.111s^3 + 0.109s^2 + 0.0045s + 0.00056} \quad (7.8)$$

Figure 7.19 shows the original compressor mass flow rate and the corrected compressor mass flow rate. By examining the compressor RPM plot and the mass flow rate plot, it is readily noted that the mass flow correction momentarily decreases the compressor mass flow following increases in the compressor speed. In other words, the static compressor model over-predicts the mass flow rate of refrigerant exiting the evaporator and entering the condenser following step increases in speed. A similar under-prediction of mass flow rate occurs for step decreases in speed. The source of these unmodeled dynamics has not been determined, but the dynamic mass flow correction provides a method for compensating for them. Possible sources of the unmodeled dynamics include the compressor model itself and the oil separator component, or some interaction between these components and others in the system.

7.3 Atmospheric Conditions Model Validation Scenario

To obtain a clear evaluation of the evaporator with humidity model, the atmospheric conditions model validation scenario was carried out with just the compressor model, the evaporator model, and a connecting pipe model. The evaporator and compressor inputs that would normally come from other components were replaced with experimental data. For example, the valve mass flow rate input to the evaporator model was replaced with experimental system mass flow rate data. The component models and inputs are shown in Figure 7.25.

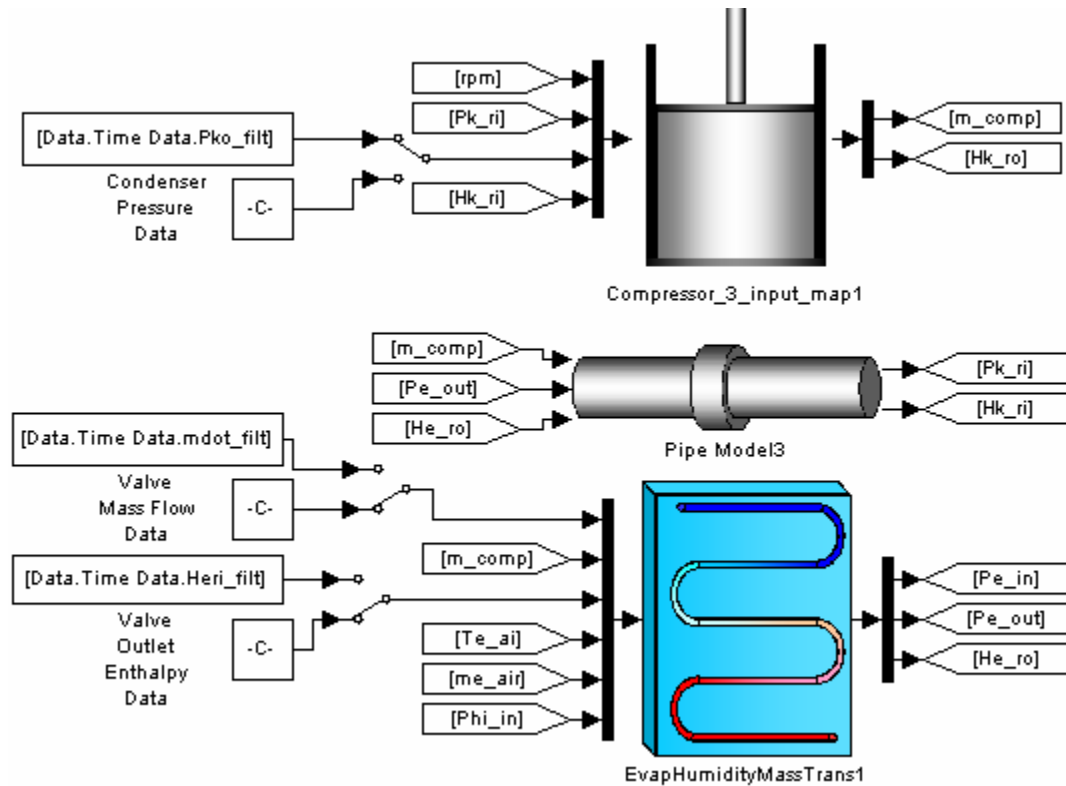


Figure 7.25 Components used in humidity model validation

7.3.1 System Inputs

The main model feature validated here is the ability to predict changes in outlet relative humidity induced by changes in inlet relative humidity. The inlet relative humidity was stepped up and down by turning the experimental system's humidifier on and off. The inlet relative humidity input plot is shown in Figure 7.26. The initial input value was determined by the ambient relative humidity in the room. The elevated relative humidity value was determined by the humidifier's capacity to add moisture to the air.

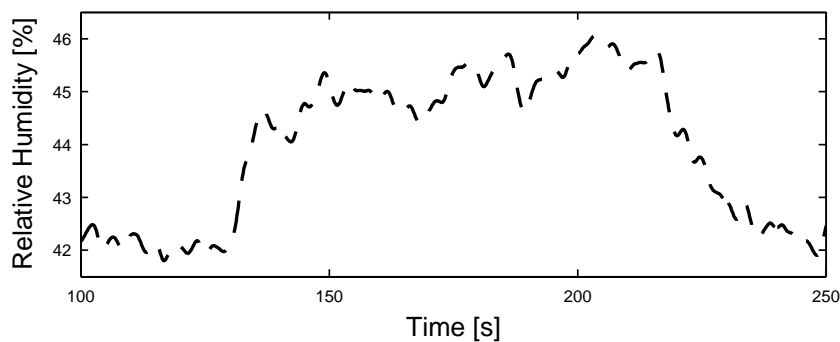


Figure 7.26 Inlet relative humidity data

Based on the measured initial conditions of inlet and outlet air temperatures, inlet and outlet relative humidity, inlet and outlet refrigerant temperature, pressure, and mass flow rate, the evaporator model's initial condition solver predicted that condensation was occurring in the first (two-phase) region but not in the second

(superheat) region. This initial condition solution was verified by observing that condensation had formed on the experimental system's evaporator inlet pipe but not on the evaporator outlet pipe, as shown in Figure 7.27.



Figure 7.27 Photograph on the inlet and outlet evaporator pipes with condensation on the inlet (lower) pipe

7.3.2 System Outputs

The two new outputs of the evaporator with humidity model are the outlet relative humidity and the condensate mass flow rate. Figure 7.28 shows a comparison of outlet relative humidity data and model output. There is a slight mismatch at the initial condition. Because the optimization problem used to solve for the initial conditions is highly constrained, the solver cannot adequately minimize the energy balance equations without producing some small deviations in the initial outlet relative humidity. The difference is not significant enough to adversely affect the validity of the simulation. The relative humidity model output matches the data very well. Figure 7.29 shows the simulated condensate mass flow rate. The experimental system does not have the capacity to measure condensate mass flow rate, so no data is presented. The plot does, however, demonstrate an increase in condensate mass flow when the inlet relative humidity increases, which is the expected result.

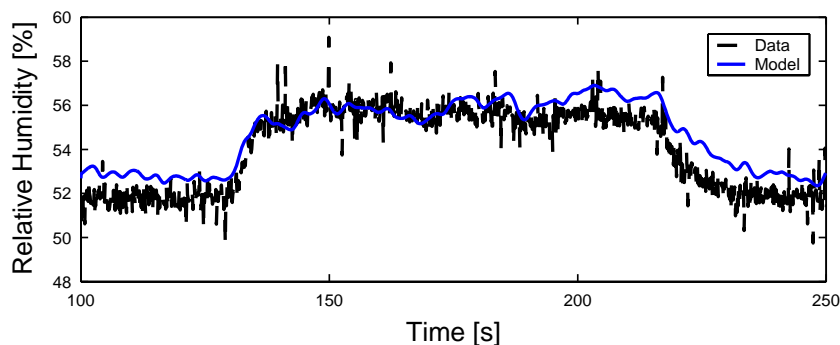


Figure 7.28 Outlet relative humidity data and model

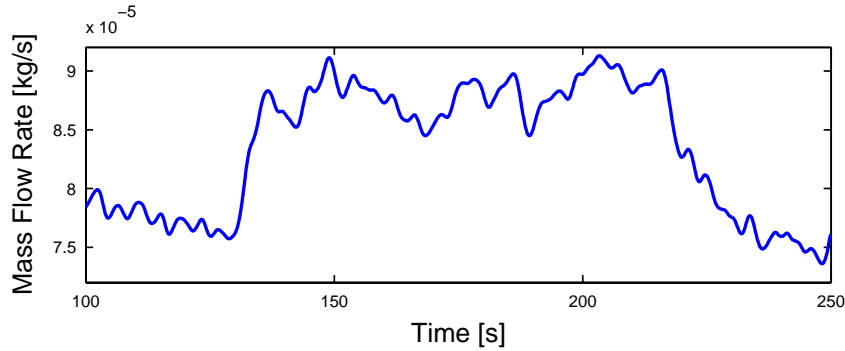


Figure 7.29 Condensate mass flow rate model

As with the outlet relative humidity initial condition, the outlet air temperature initial condition also does not match system data in Figure 7.30. The mismatch could be attributed to the sensitivity of the sensor measurement to the sensor location. On the outlet side of the evaporator, the relative humidity and the air temperature are each measured in a single location. In reality, there are significant spatial variations in outlet air temperature and relative humidity. To correct for this problem the system would need to be modified in such a way that a well-mixed outlet air stream was available for humidity and temperature measurements.

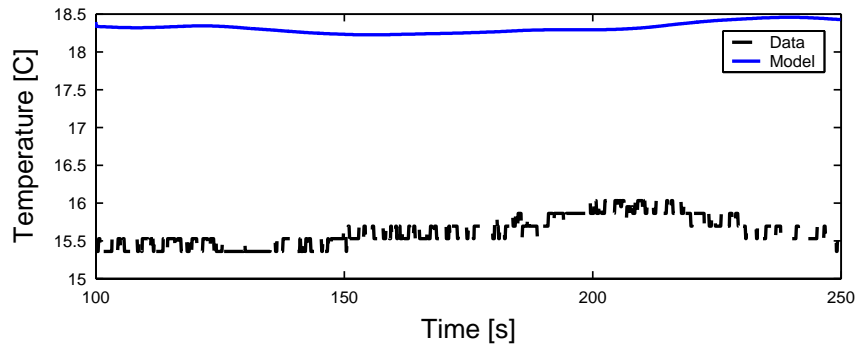


Figure 7.30 Evaporator outlet air temperature and model

In a separate test, the experimental system was used for an initial attempt at validating the condensate mass flow rate prediction. The system was run for approximately 5 hours at approximately steady-state operating conditions. The total condensate draining from the evaporator was collected, and the mass of the accumulated condensate was measured at intervals of 20 to 50 minutes. The data points are shown in Figure 7.31. A linear curve fit to the data points shows an estimated condensate mass flow rate of 4.1×10^{-5} kg/s. Based on the steady-state operating conditions used for this test, the humidity model predicts a condensate mass flow rate of 5.9×10^{-5} kg/s. The condensate mass accumulation for the model-predicted mass flow rate is also shown on the plot. For an initial modeling attempt, this degree of agreement between model and data suggests that the current model structure will be a suitable foundation for further development and refinement. The model mass flow rate may be brought closer to the measured mass flow rate by adjusting tunable parameters such as the mass transfer coefficient. For this operating condition, it was found that reducing the original mass transfer coefficient by 38% brought the mass flow

rate prediction to 4.12×10^{-5} kg/s. The justification for such an adjustment is a potential area for future research. The current calculation of the mass transfer coefficient is based on the assumption of a Lewis number of one [13]. If this assumption is not applied, the calculation of the mass transfer coefficient is much more challenging.

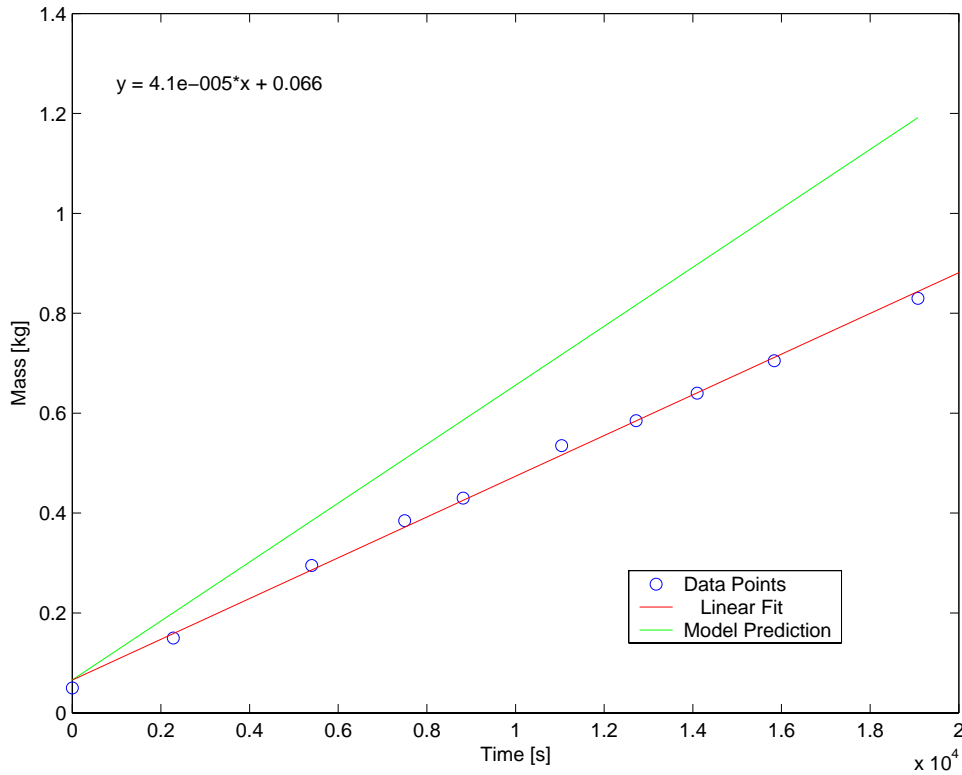


Figure 7.31 Accumulated condensation measurements and model prediction

7.3.3 Simulation Analysis

The existing experimental system does not allow for exhaustive validation of the humidity model, therefore simulation results are used to verify that model outputs are at least in agreement with logical expectations. The main shortcoming of the experimental system is the inability to create inlet conditions that force the model to operate in each of the three possible condensation conditions.

7.3.3.1 Simulation Input

Apart from the inlet relative humidity, all model inputs are constants. The initial operating condition is taken from an operating condition measured on the experimental system on a day with low ambient humidity. Initially, no condensation is occurring in the evaporator. The inlet relative humidity is ramped from the low initial value to a saturated condition. After holding the saturated condition, the inlet relative humidity is ramped back down to the initial value. The input is plotted in Figure 7.32. This input allows the model to run in all three possible conditions: no condensation, condensation in the two-phase region only, and condensation in both the two-phase region and the superheat region. The range of inlet relative humidity values (approximately 25% to 100%) used in the simulation analysis is much larger than the range (approximately 42% to 46%) covered in the model validation tests.

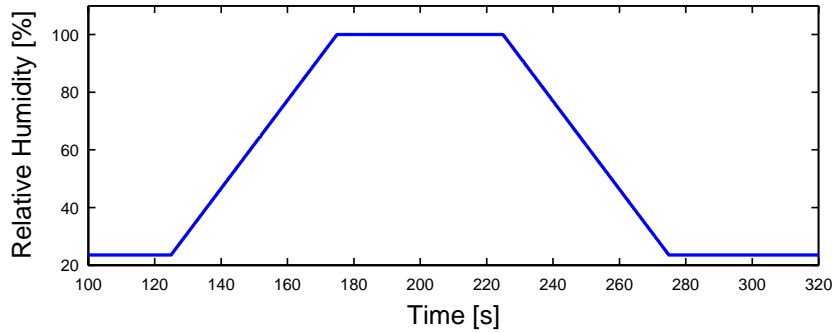


Figure 7.32 Inlet relative humidity

7.3.3.2 Simulation Output

Figure 7.33 shows the evaporator dew point temperature and the wall temperature of each fluid region. Condensation in a region occurs when the wall temperature is below the dew point temperature. As the inlet relative humidity increases, the dew point temperature increases as well, meaning that condensation will occur at higher temperatures due to the elevated moisture content in the air.

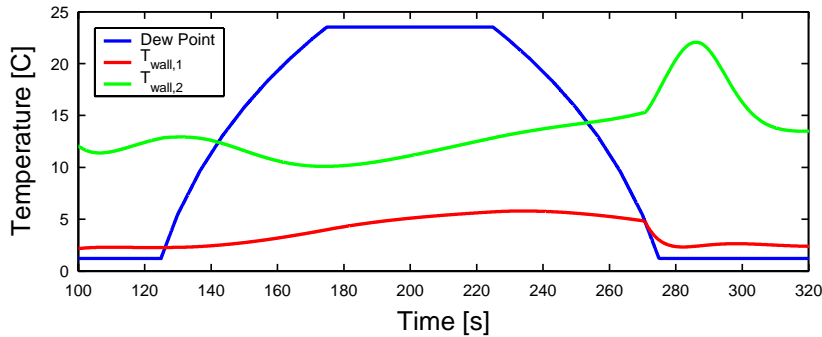


Figure 7.33 Dew point temperature and model wall temperatures

Figure 7.34 shows the outlet relative humidity prediction. The outlet relative humidity increases and decreases in roughly the same fashion as the inlet relative humidity. Small discontinuities are present when the condensation condition of a fluid region changes. One noteworthy feature of Figure 7.34 is that the outlet relative humidity reaches values greater than 100%. As explained in [8], this condition is referred to as super-saturation. The physical explanation for super-saturation is that some water vapor is condensing out of the air but not depositing on the evaporator pipes. Therefore the outlet fluid consists of a mixture of saturated air and tiny water droplets.

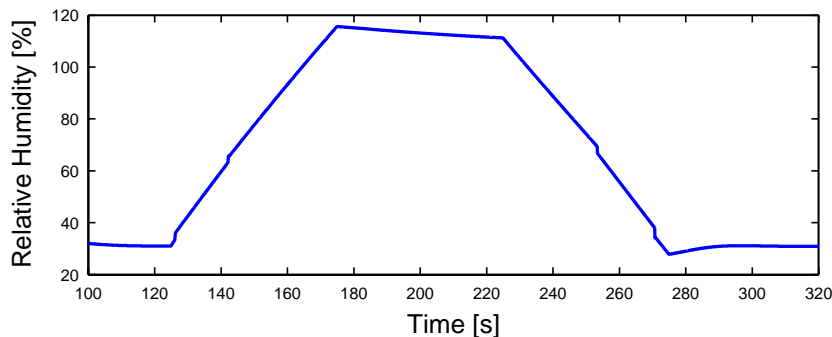


Figure 7.34 Outlet relative humidity model

Figure 7.35 shows the condensate mass flow rate prediction. The initial inlet relative humidity is sufficiently low that the mass flow rate is zero and no condensation is occurring. The mass flow rate becomes non-zero when the two-phase wall temperature drops below the dew point temperature, as seen in Figure 7.33. The mass flow rate steadily increases as the inlet relative humidity increases. The mass flow rate increases faster after condensation begins in the superheat region. Similar trends are observed for the downward inlet relative humidity ramp. The maximum condensate mass flow rate prediction is an order of magnitude larger than the maximum flow rate observed in the model validation tests. This difference is attributed to the fact that the simulation analysis inlet relative humidity input is significantly higher than the model validation test inlet relative humidity.

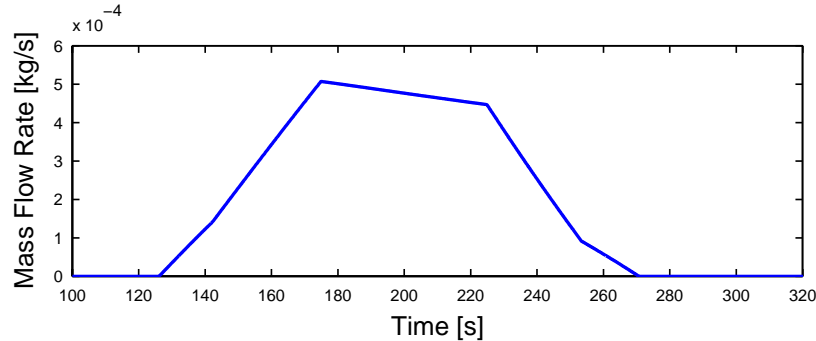


Figure 7.35 Condensate mass flow rate model

The following plots are not new outputs for the evaporator with humidity model, but they demonstrate the effects of including humidity calculations on other model outputs. Figure 7.36 shows the evaporator outlet air temperature. Discontinuities on the order of one to two degrees C are apparent when the condensation condition changes in a fluid region. These discontinuities certainly would not be present in experimental data. They are a product of the lumped parameter nature of the moving-boundary modeling approach. Figure 7.37 shows the evaporator pressure prediction. This plot is included to demonstrate that the changes in condensation condition also induce a dynamic response in the other system outputs.

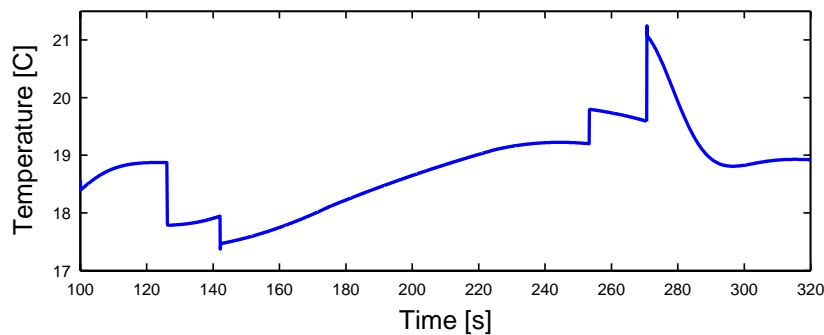


Figure 7.36 Outlet evaporator air temperature model

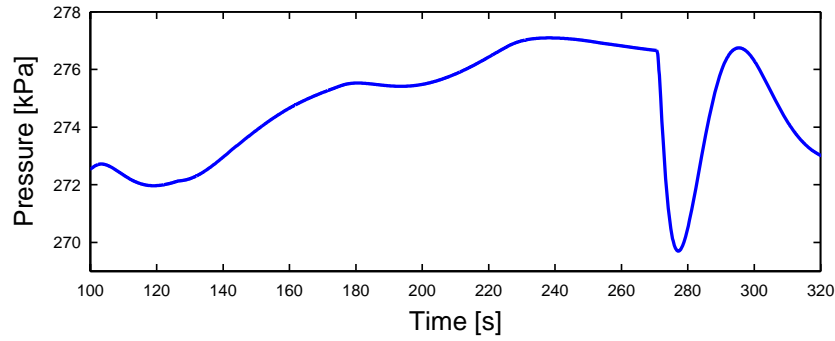


Figure 7.37 Evaporator pressure model

The simulation results indicate that the model accurately captures the qualitative effects of condensation. The model validation results show a good quantitative match between outlet relative humidity simulation output and experimental data. Based on these results, the evaporator with humidity model presented in Chapter 4 is judged to be a good foundation for future humidity and frosting model development. While the validation results presented in this section are very encouraging, they are also preliminary results and require further verification. Future model validation could include testing more operating conditions and reducing air-side spatial variations in temperature and humidity by mixing the airflow. An alternative to airflow mixing is measurement of multiple temperature and humidity signals with a sensor grid, as described in [10].

Chapter 8. Conclusions and Future Work

8.1 Summary of Research Contributions

The research described in this thesis attempts to improve the accuracy and expand the applicability of the Thermosys VCC system models. In addition, this work attempts to increase user confidence in the moving-boundary modeling framework. These goals are achieved through a number of model developments and model validation efforts.

8.1.1 Model Developments

Most of the model developments described here can be divided into the categories of semi-empirical modeling and dynamic modeling. The humidity model, which is based on first-principles but does not include dynamics or performance maps, does not fall into these categories.

8.1.1.1 Semi-empirical models

The semi-empirical model developments improve upon the accuracy of first-principles models by providing data-based estimates of key model parameters. The semi-empirical models presented here are

- j factor correlations for external heat transfer coefficient calculation
- performance maps for valve and compressor models.

The valve performance maps provide either a flow coefficient or a discharge coefficient. The compressor performance maps provide a volumetric efficiency and an adiabatic efficiency. The performance map approach gives the models both flexibility and accuracy.

8.1.1.2 Humidity Model

Two humidity models are presented. The first model assumes that condensation occurs when the bulk evaporator air temperature falls below the dew point. The second model assumes that condensation occurs when the evaporator wall temperature falls below the dew point. Based on model validation results, the second model appears to give a more accurate representation of the physical system behavior. Both models are based on first-principles energy balances and contain no dynamic relationships. A major assumption is that no condensate accumulates on the evaporator tubes.

8.1.1.3 Dynamic Models

A major contribution of this work is the presentation of the first-principles heat exchanger with receiver/accumulator models. The inclusion of these components greatly expands the range of operating conditions that can be modeled by the Thermosys Toolbox. A compressor shell thermal capacitance model is developed to account for the slow transients observed in the compressor outlet temperature. A system identification approach is used to provide a compressor mass flow correction model that minimizes errors in other component models. Finally, an evaluation of the current dynamic model capabilities under compressor cycling conditions is presented. The models are shown to be sufficiently robust to simulate some approximate cycling conditions.

8.1.2 Model Validation

The model validation results serve to evaluate the model improvements as well as increase the user's confidence in the moving-boundary modeling framework. Two main scenarios are presented, a single-steps scenario and a drive cycle scenario. The results validate the condenser with receiver model as well as demonstrate application of the dynamic mass flow correction model. Error metric comparisons are used to quantify the

improvements obtained through application of the semi-empirical modeling techniques. Results consistently demonstrate the importance of the compressor mass flow rate prediction. The humidity model is also shown to provide a reasonably accurate prediction of both the outlet relative humidity and the condensate mass flow rate.

8.2 Future Work

Future work in both modeling and model validation will improve the quality of the moving-boundary models and their acceptance in academia and industry. As the models improve and user confidence increases, the models will be useful in numerous applications.

8.2.1 Model Development

Opportunities for future model development are numerous. Possible directions for future research are given in the following list. The list is ordered according to a suggested priority for the research directions.

- Develop a model switching scheme. Completion of this task is essential for successful simulation of cycling and start-up conditions. In addition, the behavior of the mass flow devices at very low flow rates will need to be characterized.
- Develop a dynamic model to improve the compressor mass flow rate prediction, as this model output has a significant effect on the accuracy of other component models. Improvements in the mass flow rate prediction could be achieved by creating a first-principles dynamic compressor model, including oil flow modeling, or directly identifying a compressor mass flow rate model.
- Improve the semi-empirical modeling approach presented here by evaluating additional performance map structures and inputs. The semi-empirical approach could be applied to other VCC system components which contain parameters that are best described with data-driven correlations.
- Improve the humidity model by taking into account the effects of condensate retention on the heat exchanger tubes. This task will likely require a blending of first-principles dynamic modeling and semi-empirical parameter estimates.

8.2.2 Model Validation

Additional successful model validation results will always increase user confidence in the accuracy of the moving-boundary models. Future model validation could focus on validating the system models on a larger range of operating conditions. Some system configurations have yet to be validated, such as systems including models of the accumulator, the capillary tube, the automatic expansion valve, and the thermostatic expansion valve. The humidity model validation could be improved by validating a range of conditions that includes no condensation, condensation on the two-phase region, and condensation on both the two-phase and the superheat regions. Eliminating spatial variation in the air-side humidity and temperature measurements (through air flow mixing or spatially distributed sensor arrays) would also be an improvement to the results presented here.

8.2.3 Model Applications

An accurate and tractable dynamic model of VCC systems has numerous application areas. The most obvious is dynamic analysis for improved system level design. The low-order nature of the moving-boundary models makes them especially useful for control design. Control design based on moving-boundary models is already an active research area and should yield significant improvements in system efficiency [41, 20]. Fault detection is also being explored as a possible application of these models [26].

List of References

- [1] "Parker Bulletin 21-02D," Parker Hannifin, Cleveland, OH.
- [2] "Sporlan Bulletin 10-9," Sporlan Valve Company, Washington, MO, June 2001.
- [3] Anderson, B.D.O., "Controller Design: Moving From Theory to Practice," *IEEE Control Systems Magazine*, vol. 13, no. 4, pp. 16-25, Aug, 1993.
- [4] Bendapudi, S. and Braun, J.E., "A Review of Literature on Dynamic Models of Vapor Compression Equipment," ASHRAE Report #4036-5, May, 2002.
- [5] Bristow, D.A., Tharayil, M., and Alleyne, A., "A Survey of Iterative Learning Control," *IEEE Control Systems Magazine*, vol. 26, no. 3, pp. 96-114, Jun, 2006.
- [6] Broersen, P.M.T. and van der Jagt, M.F.G., "Hunting of Evaporators Controlled by a Thermostatic Expansion Valve," *ASME Journal of Dynamic Systems Measurement & Control*, vol. 102, no. 2, pp. 130-135, Jun, 1980.
- [7] Cengel, Y. A. and Boles, M. A. Thermodynamics: An Engineering Approach, Boston, MA: WCB McGraw-Hill, 1998.
- [8] Chen, H., Thomas, L, and Besant, R., "Fan Supplied Heat Exchanger Performance Under Frosting Conditions," *International Journal of Refrigeration*, vol. 26, no. 1, pp. 140-149, Jan, 2003.
- [9] Chi, J. and Didion, D., "A Simulation Model of the Transient Performance of a Heat Pump," *International Journal of Refrigeration*, vol. 5, no. 3, pp. 176-184, May, 1982.
- [10] Dane, M., Miller, N., Alleyne, A., Bullard, C., and Hrnjak, P., "Investigation of Control Strategies for Reducing Mobile Air Conditioning Power Consumption," Air Conditioning and Refrigeration Center, University of Illinois at Urbana-Champaign, ACRC TR-199, Aug, 2002.
- [11] Dhar, M. and Soedel, W., "Transient Analysis of a Vapor Compression Refrigeration System," in *Proceedings of the XVth International Congress of Refrigeration*, Venice, Italy, vol. 2, 1979 , pp. 1031-1067.
- [12] Eborn, J., "On Model Libraries for Thermo-hydraulic Applications," Department of Automatic Control, Lund Institute of Technology, Lund, Sweden, Mar. 2001.
- [13] Eckert, E.R.G. and Drake, R.M., Analysis of Heat and Mass Transfer, New York, NY: McGraw-Hill, 1972.
- [14] Energy Information Administration, 1999 CBECS Detailed Tables, http://www.eia.doe.gov/emeu/cbecs/detailed_tables_1999.html#ce
- [15] Energy Information Administration, Residential Energy Consumption Survey 2001 Consumption and Expenditure Data Tables, <http://www.eia.doe.gov/emeu/recs/recs2001/detailcetbls.html>
- [16] Federal Register, "Part II Environmental Protection Agency. Motor Vehicle Emissions Federal Test Procedure Revisions: Final Regulations," 40 CFR Part 86, Oct. 1996.
- [17] Grald, E.W. and MacArthur, J.W., "A Moving-Boundary Formulation for Modeling Time-Dependent Two-Phase Flows," *International Journal of Heat & Fluid Flow*, vol. 13, no. 3, pp. 266-272, Sep, 1992.
- [18] Gruhle, W.D. and Isermann, R., "Modeling and Control of a Refrigerant Evaporator," *ASME Journal of Dynamic Systems Measurement & Control*, vol. 107, no. 4, pp. 235-240, Dec, 1985.
- [19] He, X., Liu, S., and Asada, H., "Moving-Interface Model of Two-Phase Flow Heat Exchanger Dynamics for Control of Vapor Compression Cycle," *ASME Advanced Energy Systems*, vol. 32, pp. 69-75, 1994.
- [20] He, X.D., Asada, H., Liu, S., and Itoh, H., "Multivariable Control of Vapor Compression Systems," *HVAC&R Research*, vol. 4, no. 3, pp. 205-230, Jul, 1998.
- [21] He, X.D., Liu, S., and Asada, H., "Modeling of Vapor Compression Cycles for Multivariable Feedback Control of HVAC Systems," *ASME Journal of Dynamic Systems, Measurement, and Control*, vol. 119, no. 2, pp. 183-191, Jun, 1997.
- [22] Incropera, F. P. and DeWitt, D. P. Fundamentals of Heat and Mass Transfer, New York: John Wiley & Sons, 1996.

- [23] Jensen, J.M. and Tummescheit, H., "Moving Boundary Models for Dynamic Simulations of Two-Phase Flows," in *Proceedings of the 2nd International Modelica Conference*, 2002, pp. 235-244.
- [24] Kapadia, M. and Wolgemuth, C.H., "A Dynamic Model of a Condenser in a Closed Rankine Cycle Power Plant," in *Proceedings of the 1984 American Control Conference*, New York, NY, vol. 1, 1984, pp. 79-84.
- [25] Kays, W. M. and London, A. L. *Compact Heat Exchangers*, New York: McGraw-Hill Book Company, 1984.
- [26] Keir, M., "Dynamic Modeling, Control and Fault Detection in Vapor Compression Systems," Dept. of Mechanical and Industrial Engineering, University of Illinois, Urbana, IL, Aug, 2006.
- [27] Keir, M., Rasmussen, B.P., and Alleyne, A., "Improving Energy Efficiency in Automotive Vapor Compression Cycles through Advanced Control Design," SAE 2006 World Congress and Exposition, Detroit, MI, Apr, 2006.
- [28] Kim, N.-H., Yun, J.-H., and Webb, R.L., "Heat Transfer and Friction Correlations for Wavy Plate Fin-and-Tube Heat Exchangers," *ASME Journal of Heat Transfer*, vol. 119, no. 3, pp. 560-567, Aug, 1997.
- [29] Klein, S.A. and Alvarado, F.L., *EES-Engineering Equation Solver, F-Chart Software*, Middleton, WI, 2002.
- [30] Korte, C. and Jacobi, A.M., "Condensate Retention Effects on the Performance of Plain-Fin-and-Tube Heat Exchangers: Retention Data and Modeling," *ASME Journal of Heat Transfer*, vol. 123, no. 5, pp. 926-936, Oct, 2001.
- [31] Lenger, M.J., Jacobi, A.M., and Hrnjak, P.S., "Superheat Stability of an Evaporator and Thermostatic Expansion Valve," Air Conditioning and Refrigeration Center, University of Illinois at Urbana Champaign, ACRC TR-138, Jul 1998.
- [32] Ljung, L., *System Identification*, Prentice Hall, New Jersey, 1999.
- [33] MacArthur, J.W. and Grald, E.W., "Unsteady Compressible Two-Phase Flow Model for Predicting Cyclic Heat Pump Performance and a Comparison With Experimental Data," *International Journal of Refrigeration*, vol. 12, no. 1, pp. 29-41, Jan, 1989.
- [34] McQuiston, F.C., "Fin Efficiency with Combined Heat and Mass Transfer," *ASHRAE Transactions*, vol. 81, no. 1, pp. 350-355, 1975.
- [35] Mirth, D.R. and Ramadhyani, S., "Prediction of Cooling-Coil Performance Under Condensing Conditions," *International Journal of Heat and Fluid Flow*, vol. 14, no. 4, pp. 391-400, Dec, 1993.
- [36] Moore, K. L., *Iterative Learning Control for Deterministic Systems*, Springer-Verlag London, 1993.
- [37] National Renewable Energy Laboratory, Ancillary Loads Reduction, http://www.nrel.gov/vehiclesandfuels/ancillary_loads/ac_emissions.html
- [38] Pettit, N.B.O.L., Willatzen, M., and Ploug-Sorensen, L., "A General Dynamic Simulation Model for Evaporators and Condensers in Refrigeration. Part II: Simulation and Control of an Evaporator," *International Journal of Refrigeration*, vol. 21, no. 5, pp. 404-414, Aug, 1998.
- [39] Popper, K.R., *Logik der Forschung*, Julius Springer, Vienna, Austria, 1935.
- [40] Rasmussen, B.P., "Control-Oriented Modeling of Transcritical Vapor Compression Systems," Dept. of Mechanical and Industrial Engineering, University of Illinois, Urbana, IL, Oct. 2002.
- [41] Rasmussen, B.P., "Dynamic Modeling and Advanced Control of Air Conditioning and Refrigerating Systems," Dept. of Mechanical and Industrial Engineering, University of Illinois, Urbana, IL, Dec, 2005.
- [42] Rasmussen, B.P. and Alleyne, A., "Control-Oriented Modeling of Transcritical Vapor Compression Systems," *ASME Journal of Dynamic Systems, Measurement, and Control*, vol. 126, no. 1, pp. 54-64, Mar, 2004.
- [43] Rice, C.K., "Effect of Void Fraction Correlation and Heat Flux Assumption on Refrigerant Charge Inventory Predictions," *ASHRAE Transactions*, vol. 93, no. 1, pp. 341-367, 1987.
- [44] Shah, R., "Dynamic Modeling and Control of Single and Multi-Evaporator Subcritical Vapor Compression Systems," Dept. of Mechanical and Industrial Engineering, University of Illinois, Urbana, IL, Aug. 2003.

- [45] Wang, C., Chi, K., and Chang, C., "Heat Transfer and Friction Characteristics of Plain Fin-and-Tube Heat Exchangers, Part II: Correlation," *International Journal of Heat and Mass Transfer*, vol. 43, no. 15, pp. 2641-2823, Aug, 2000.
- [46] Wang, C., Lin, Y., Lee, C., and Chang, Y., "Investigation of Wavy Fin-and-Tube Heat Exchangers: A Contribution to Databank," *Experimental Heat Transfer*, vol. 12, no. 1, pp. 73-89, Jan-Mar, 1993.
- [47] Willatzen, M., Pettit, N.B.O.L., and Ploug-Sorensen, L., "General Dynamic Simulation Model for Evaporators and Condensers in Refrigeration. Part I: Moving-Boundary Formulation of Two-Phase Flows with Heat Exchange," *International Journal of Refrigeration*, vol. 21, no. 5, pp. 398-403, Aug, 1998.

Appendix A. Sample Code

H.1 Condenser / Factor Correlation

```
% This file generates the experimental system j factor information to be
% stored in the data structure HX. The information includes Reynolds
% number data points, j factor data points, the constriction ratio
% (sigma) and the air-side hydraulic diameter (Dh).

% The j factor correlation is from the following article:
% International Journal of Heat and Mass Transfer Volume 43, Issue 15,
% Pages 2641-2823 (1 August 2000)

% Create a Reynolds number vector (stored in HX structure)
Re = [100 200 300 400 500 600 700 800 900 1000 ...
      2000 3000 4000 5000 6000 7000 8000 9000 10000];

% Number of tube rows in the condenser
N = 3;

% Fin pitch (distance between fins) in inches
Fp = .1429;

% Tube outside diameter in inches
Do = .375;

% Fin thickness in inches
Ft = .0093;

% Fin collar outside diameter in inches (fin collar is defined as tube
% diameter plus twice the fin thickness)
Dc = Do + 2*Ft;

% Longitudinal tube pitch (distance between tube centers in direction of
% air flow) in inches
Pl = .956;

% Flow length in inches (flow length is explained in Chapter 3)
L = 3*.956;

% Flow cross-sectional area, also known as the minimum free flow area, in
% square inches
% Flow cross-sectional area = Frontal Area - Tube Diameter*Number of
% Tubes at cross section*Tube_Length - Fin thickness*Fin height*Number of
% Fins
Ac = (10.656*13.062) - .375*10*13.062 - .0093*10*89;

% Total heat transfer area in square inches, provided by manufacturer
A = 4328.64;

% Air-side hydraulic diameter in inches as defined by Kays and London
Dh = 4*L*Ac/A;

% Transverse tube pitch in inches (distance between tube centers in
% direction transverse to air flow)
Pt = 1;
```

```

% Powers used in the j factor correlation
P3 = -.361 - (.042*N./log(Re)) + .158*log(N*(Fp/Dc)^.41);
P4 = -1.224 - (.076*(Pl/Dh)^1.42)./(log(Re));
P5 = -.083 + (.058*N)./(log(Re));
P6 = -5.735 + 1.21*log(Re/N);

% Colburn j factor correlation (stored in HX structure)
j_cond = .086.*Re.^P3.*N.^P4.*(Fp/Dc).^P5.*(Fp/Dh).^P6*(Fp/Pt).^-.93;

% Calculate the frontal area in square inches
Afr = (10.656*13.062);

% Calculate the constriction ratio (stored in HX structure)
sigma = Ac/Afr;

% Convert Dh from inches to meters (stored in HX structure)
DhSI = Dh*0.0254;

```

H.2 Evaporator *j* Factor Correlation

```

% This file generates the experimental system j factor information to be
% stored in the data structure HX. The information includes Reynolds
% number data points, j factor data points, the constriction ratio
% (sigma) and the air-side hydraulic diameter (Dh).

% The j factor correlation is from the following article:
% International Journal of Heat and Mass Transfer Volume 43, Issue 15,
% Pages 2641-2823 (1 August 2000)

% Create a Reynolds number vector (stored in HX structure)
Re = [100 200 300 400 500 600 700 800 900 1000 ...
      2000 3000 4000 5000 6000 7000 8000 9000 10000];

% Number of tube rows in the condenser
N = 3;

% Fin pitch (distance between fins) in inches
Fp = .1429;

% Tube outside diameter in inches
Do = .375;

% Fin thickness in inches
Ft = .0093;

% Fin collar outside diameter in inches (fin collar is defined as tube
% diameter plus twice the fin thickness)
Dc = Do + 2.*Ft;

% Longitudinal tube pitch (distance between tube centers in direction of
% air flow) in inches
Pl = .956;

% Flow length in inches (flow length is explained in Chapter 3)
L = 3*.956;

% Flow cross-sectional area, also known as the minimum free flow area, in

```

```

% square inches
% Flow cross-sectional area = Frontal Area - Tube Diameter*Number of
% Tubes at cross section*Tube_Length - Fin thickness*Fin height*Number of
% Fins
Ac = (10.656*13.062) - .375*10*13.062 - .0093*10*89;

% Total heat transfer area in square inches, provided by manufacturer
A = 4328.64;

% Air-side hydraulic diameter in inches as defined by Kays and London
Dh = 4*L*Ac/A;

% Transverse tube pitch in inches (distance between tube centers in
% direction transverse to air flow)
Pt = 1;

% Powers used in the j factor correlation
P3 = -.361 - (.042*N./log(Re)) + .158*log(N*(Fp/Dc)^.41);
P4 = -1.224 - (.076*(Pl/Dh)^1.42)./(log(Re));
P5 = -.083 + (.058*N)./(log(Re));
P6 = -5.735 + 1.21*log(Re/N);

% Colburn j factor correlation (stored in HX structure)
j_cond = .086.*Re.^P3.*N.^P4.*(Fp/Dc).^P5.*(Fp/Dh).^P6*(Fp/Pt).^-.93;

% Calculate the frontal area in square inches
Afr = (10.656*13.062);

% Calculate the constriction ratio (stored in HX structure)
sigma = Ac/Afr;

% Convert Dh from inches to meters (stored in HX structure)
DhSI = Dh*0.0254;

```

H.3 EEV Performance Map

```

% This file creates a EEV flow coefficient performance map with inputs of
% inlet pressure, outlet pressure, and valve command signal. The
% experimental system data is stored in the workspace in a structure
% called Data.

% The start and finish variables are used to select the range of data
% that will be used to generate the map
start = 2500;
finish = 3800;

% Store the selected range of data in new variables
% MDOT = mass flow rate
% PI = valve inlet pressure
% PO = valve outlet pressure
% EEV = valve command signal
% TIME = time values
MDOT = Data.mdot(start:finish);
PI = Data.Pko(start:finish);
PO = Data.PeI_2(start:finish);
EEV = Data.EEV_ref(start:finish);
TIME = Data.Time(start:finish);

```



```

% Calculate the inlet fluid density, assuming the inlet fluid is
% saturated vapor
RHO_V = interp1(FluidProp.Psat,FluidProp.Rhof,PI);

% Calculate the flow coefficient (valve area * discharge coefficient)
CF = MDOT./((sqrt(RHO_V.*(PI-PO))));

% Form input matrix X, assuming a model structure
X = [ones(size(MDOT)) EEV PI.^5 PO.^5 PI.*PO];

% Find model coefficients using left matrix division (approximate matrix
% inverse)
a = X\CF

% Find the flow coefficient values predicted by the model
CF_model = X*a;

% Find the error (difference between data and model flow coefficient)
error = (CF_model-CF);

% Find the maximum error value, used to evaluate model structure
MaxErr = max(abs(error));

% Find the average error value, used to evaluate model structure
AveErr = mean(error);

% Find the RMS error, used to evaluate model structure
RMS = norm(error)/sqrt(length(MDOT))

% Plot the error as a function of time, used to evaluate model structure
plot(TIME,error)

% Clear the variables used for map generation
% Pi = inlet pressure
% Po = outlet pressure
% eev = valve command signal
% Cf_map = lookup table array
clear Pi
clear Po
clear eev
clear Cf_map

% Define input variable vectors
Pi = 700:20:1100;
Po = 100:25:500;
eev = 0:1:25;

% Generate the lookup table using a for loop for each input, equation
% should match the model structure chosen for the X matrix
for c1 = 1:length(eev)
    for c2 = 1:length(Pi)
        for c3 = 1:length(Po)
            Cf_map(c1,c2,c3) = a(1) + a(2).*eev(c1) + a(3).*Pi(c2).^5 ...
                + a(4).*Po(c3).^5 + a(5).*Pi(c2)*Po(c3);
        end
    end
end

```

```

    end
end

% Store the input vectors and lookup table array in a structure
ValveProp.Pi = Pi;
ValveProp.Po = Po;
ValveProp.u = eev;
ValveProp.Cf_v = Cf_map;

```

H.4 AEV Performance Map

```

% This file creates a AEV flow coefficient performance map with inputs of
% pressure differential and evaporator pressure. The experimental system
% data is stored in the workspace in a structure called Data.

```

```

% The start and finish variables are used to select the range of data
% that will be used to generate the map
start = 2500;
finish = 3800;

```

```

% Store the selected range of data in new variables
% MDOT = mass flow rate
% PI = valve inlet pressure
% PO = valve outlet pressure
% PDELTA = pressure differential
% TIME = time values
MDOT = Data.mdot(start:finish);
PI = Data.Pko(start:finish);
PO = Data.Pei_2(start:finish);
PDELTA = PI - PO;
TIME = Data.Time(start:finish);

```

```

% Calculate the inlet fluid density, assuming the inlet fluid is
% saturated vapor
RHO_V = interp1(FluidProp.Psat,FluidProp.Rhof,PI);

```

```

% Calculate the flow coefficient (valve area * discharge coefficient)
CF = MDOT./(sqrt(RHO_V.*(PI-PO)));

```

```

% Form input matrix X, assuming a model structure
X = [ones(size(MDOT)) PDELTA PO];

```

```

% Find model coefficients using left matrix division (approximate matrix
% inverse)
a = X\CF

```

```

% Find the flow coefficient values predicted by the model
CF_model = X*a;

```

```

% Find the error (difference between data and model flow coefficient)
error = (CF_model-CF);

```

```

% Find the maximum error value, used to evaluate model structure
MaxErr = max(abs(error));

```

```

% Find the average error value, used to evaluate model structure
AveErr = mean(error);

```

```

% Find the RMS error, used to evaluate model structure
RMS = norm(error)/sqrt(length(MDOT))

% Plot the error as a function of time, used to evaluate model structure
plot(TIME,error)

% Clear the variables used for map generation
% dP = pressure differential
% Po = outlet pressure
% Cf_map = lookup table array
clear dP
clear Po
clear Cf_map

% Define input variable vectors
dP = 300:5:700;
Po = 150:5:400;

% Generate the lookup table using a for loop for each input, equation
% should match the model structure chosen for the X matrix
for c1 = 1:length(dP)
    for c2 = 1:length(Po)
        Cf_map(c1,c2) = a(1) + a(2).*dP(c1) + a(3).*Po(c2);
    end
end

% Store the input vectors and lookup table array in a structure
ValveProp.dP = dP;
ValveProp.Po = Po;
ValveProp.Cf_v = Cf_map;

```

H.5 TEV Performance Map

```

% This file creates a TEV discharge coefficient performance map with
% inputs of valve stem turns and pressure drop. An area map with an
% input of the difference between sensing bulb pressure and evaporator
% pressure is also created. The experimental system data is stored in
% the workspace in multiple data structures. Each data structure
% corresponds to a different valve turn setting. Many of the physical
% parameters used in this file are estimates.

% Store the selected range of data in new variables. The data is divided
% based on the number of valve stem turns
% MDOT = mass flow rate
% PEI = valve inlet pressure
% PDELTA = valve pressure differential
% TERO = evaporator outlet temperature
% TURNS = number of valve stem turns
MDOT = [TEV_6_Data.mdot(1:3645); TEV_7_Data.mdot(1:3690);...
        TEV_8_Data.mdot(1:3755); TEV_9_Data.mdot(1:3925);...
        TEV_10_Data.mdot(1:3960); TEV_11_Data.mdot(1:4125);...
        TEV_12_Data.mdot(1:4100)];
PEI = [TEV_6_Data.Pei(1:3645); TEV_7_Data.Pei(1:3690);...
        TEV_8_Data.Pei(1:3755); TEV_9_Data.Pei(1:3925);...
        TEV_10_Data.Pei(1:3960); TEV_11_Data.Pei(1:4125);...
        TEV_12_Data.Pei(1:4100)];

```

```

PDELTA = [TEV_6_Data.Pdelta(1:3645); TEV_7_Data.Pdelta(1:3690);...
    TEV_8_Data.Pdelta(1:3755); TEV_9_Data.Pdelta(1:3925);...
    TEV_10_Data.Pdelta(1:3960); TEV_11_Data.Pdelta(1:4125);...
    TEV_12_Data.Pdelta(1:4100)];
TERO = [TEV_6_Data.Tero_im(1:3645); TEV_7_Data.Tero_im(1:3690);...
    TEV_8_Data.Tero_im(1:3755); TEV_9_Data.Tero_im(1:3925);...
    TEV_10_Data.Tero_im(1:3960); TEV_11_Data.Tero_im(1:4125);...
    TEV_12_Data.Tero_im(1:4100)];
TURNS = [6*ones(3645,1); 7*ones(3690,1); 8*ones(3755,1);...
    9*ones(3925,1); 10*ones(3960,1); 11*ones(4125,1);...
    12*ones(4100,1)];

% Calculate the pressure in the sensing bulb
PBULB = interp1(FluidProp.Tsat,FluidProp.Psat,TERO);

% Calculate the inlet fluid density, assuming the inlet fluid is
% saturated liquid
RHO_V = interp1(FluidProp.Psat,FluidProp.Rhof,PEI);

% Find the pressure applied by the spring, based on a force balance on
% the valve diaphragm
Spring = PBULB - PEI;

% Plot the pressure applied by the spring. This plot is used to
% determine the range over which the spring can be treated as a linear
% spring. In this case, the spring appears linear over the 7, 8, 9, and
% 10 turns data sets.
figure(1)
plot(Spring)

% Assume linear spring (use data from 7,8,9,10). This section finds the
% average spring pressure (P_spring) over the four valve turn data sets.
% The x# variables are indexes used when calculating P_spring.
turns_used = [7 8 9 10];
x0 = 3645;
x1 = 3645+3690;
x2 = 3645+3690+3755;
x3 = 3645+3690+3755+3925;
x4 = 3645+3690+3755+3925+3960;
P_spring = [mean(Spring(x0+1:x1)) mean(Spring(x1+1:x2))...
    mean(Spring(x2+1:x3)) mean(Spring(x3+1:x4))];

% Assume a valve diaphragm area in m^2, the actual value is unknown
Ad = 10e-6;

% Plot the spring force (diaphragm area * spring pressure) as a function
% of turns
figure(2)
plot(turns_used,Ad*P_spring);

% Applying a linear curve fit to the previous plot shows that the spring
% force = 0.000172 (turns) - 1.25*10^-6

% Assume that 1 turn corresponds to a specified travel length in meters,
% actual parameter is unknown
travel_length = 0.0001;

```

```

% The spring constant is found by dividing the spring force per turn by
% the travel length per turn
K = 0.000172/travel_length;

% Find the spring compression
X = (PBULB-PEI)*Ad/K;

% Assume an unobstructed valve opening area in m^2, the actual parameter
% value is unknown
A_out = 0.0001;

% Assume an obstructing pin tip angle in degrees, the actual parameter
% value is unknown
alpha = 50;

% assume an initial (valve closed) spring compression
X0 = 3e-6;

% Calculate delta, the difference between current and initial spring
% compression
delta = X - X0;

% Calculate AB, see Figure X
AB = delta*sin(.5*alpha*pi/180);

% Calculate the opening radius (also the large cone radius)
r_l = sqrt(A_out/pi);

% Calculate the large cone height
h_l = r_l*tan(.5*alpha*pi/180);

% Calculate the large cone area
area_l = pi*r_l*sqrt(r_l^2 + h_l^2);

% Calculate the small cone radius
r_s = r_l - cos(.5*alpha*pi/180).*AB;

% Calculate the small cone height
h_s = h_l - sin(.5*alpha*pi/180).*AB;

% Calculate small cone area
area_s = pi.*r_s.*sqrt(r_s.^2 + h_s.^2);

% Calculate the valve opening area
A = area_l - area_s;

% Plot the area to see if it is reasonable
figure(3)
plot(A)

% Calculate the discharge coefficient
CV = MDOT./(A.*(sqrt(RHO_V).*PDELTA.^0.5));

% Form input matrix X, assuming a model structure
B = [ones(size(MDOT)) PDELTA PDELTA.^2 TURNS];

```

```

% Find model coefficients using left matrix division (approximate matrix
% inverse)
a = B\CV

% Find the flow coefficient values predicted by the model
CV_model = B*a;

% Find the error (difference between data and model flow coefficient)
error = (CV_model-CV);

% Find the maximum error value, used to evaluate model structure
MaxErr = max(abs(error));

% Find the average error value, used to evaluate model structure
AveErr = mean(error);

% Find the RMS error, used to evaluate model structure
RMS = norm(error)/sqrt(length(MDOT));

% Clear the variables used for map generation
% dP = pressure differential
% turn = number of valve stem turns
% Pb_Pe = bulb pressure minus evaporator pressure
% Cd_map = lookup table array for discharge coefficient
% area = lookup vector for valve opening area
clear dP
clear turn
clear Pb_Pe
clear Cd_map
clear area

% Define input variable vectors
dP = 250:10:700;
turn = 6.5:0.25:10.5;
Pb_Pe = 60:1:190;

% Generate the valve opening area map. First find the spring compression
% values associated with the Pb - Pe values. Then find the valve
% displacement values associated with the spring compression values.
% Then find the valve opening area values associated with the valve
% displacement values. This process involves repeating the valve area
% calculations from above that are a function of displacement, delta.
X_map = (Pb_Pe)*Ad/K;
delta_map = X_map - X0;
AB_map = delta_map*sin(.5*alpha*pi/180);
r_s_map = r_l - cos(.5*alpha*pi/180).*AB_map;
h_s_map = h_l - sin(.5*alpha*pi/180).*AB_map;
area_s_map = pi.*r_s_map.*sqrt(r_s_map.^2 + h_s_map.^2);
area_map = area_l - area_s_map;

% Generate the lookup table using a for loop for each input, equation
% should match the model structure chosen for the X matrix
for c1 = 1:length(turn)
    for c2 = 1:length(dP)
        Cd_map(c1,c2) = a(1) + a(2).*dP(c2) + a(3).*dP(c2)^2 + a(4).*turn(c1);
    end
end

```

```

end
end

% Store the input vectors, lookup vector, and lookup table array in a
% structure
ValveProp.dP = dP;
ValveProp.turn = turn;
ValveProp.PbPe = Pb_Pe;
ValveProp.area = area_map;
ValveProp.Cd_v = Cd_map;

```

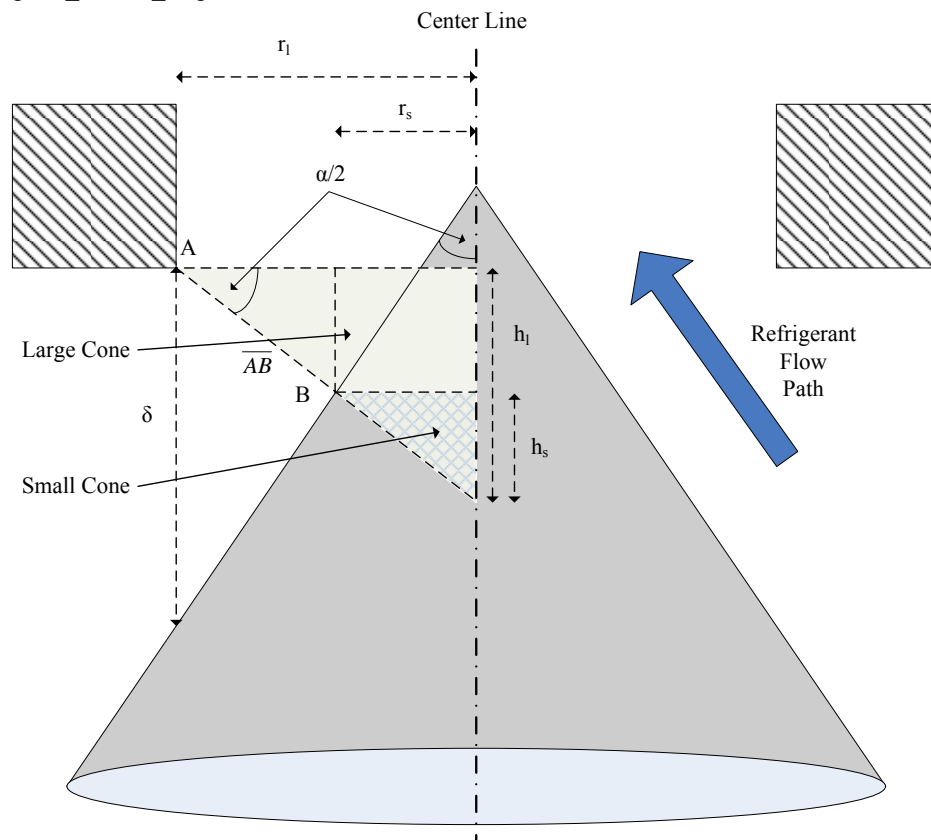


Figure A.1 Diagram of TEV geometry

H.6 Capillary Tube Performance Map

```

% This file creates a capillary tube flow coefficient performance map a
% pressure differential input. The experimental system data is stored in
% the workspace in a structure called Data.

```

```

% The start and finish variables are used to select the range of data
% that will be used to generate the map
start = 2500;
finish = 3800;

```

```

% Store the selected range of data in new variables
% MDOT = mass flow rate
% PI = valve inlet pressure
% PO = valve outlet pressure
% PDELTA = pressure differential
% TIME = time values

```

```

MDOT = Data.mdot(start:finish);
PI = Data.Pko(start:finish);
PO = Data.Pei_2(start:finish);
PDELTA = PI - PO;
TIME = Data.Time(start:finish);

% Calculate the inlet fluid density, assuming the inlet fluid is
% saturated vapor
RHO_V = interp1(FluidProp.Psat,FluidProp.Rhof,PI);

% Calculate the flow coefficient (valve area * discharge coefficient)
CF = MDOT./(sqrt(RHO_V.*(PI-PO)));

% Form input matrix X, assuming a model structure
X = [ones(size(MDOT)) PDELTA PDELTA.^2 PDELTA.^3];

% Find model coefficients using left matrix division (approximate matrix
% inverse)
a = X\CF

% Find the flow coefficient values predicted by the model
CF_model = X*a;

% Find the error (difference between data and model flow coefficient)
error = (CF_model-CF);

% Find the maximum error value, used to evaluate model structure
MaxErr = max(abs(error));

% Find the average error value, used to evaluate model structure
AveErr = mean(error);

% Find the RMS error, used to evaluate model structure
RMS = norm(error)/sqrt(length(MDOT))

% Plot the error as a function of time, used to evaluate model structure
plot(TIME,error)

% Clear the variables used for map generation
% dP = pressure differential
% Cf_map = lookup table vector
clear dP
clear Cf_map

% Define input variable vectors
dP = 450:5:700;

% Generate the lookup table using a for loop for each input, equation
% should match the model structure chosen for the X matrix
for c1 = 1:length(dP)
    Cf_map(c1) = a(1) + a(2).*dP(c1) + a(3).*dP(c1)^2 + a(4).*dP(c1)^3;
end

% Store the input vector and lookup table vector in a structure
ValveProp.dP = dP;
ValveProp.Cf_v = Cf_map;

```


H.7 Volumetric Efficiency Performance Map

```
% This file creates a compressor volumetric efficiency performance map
% with inputs of inlet pressure, outlet pressure, and compressor speed.
% The experimental system data is stored in the workspace in a structure
% called AllData.

% The start and finish variables are used to select the range of data
% that will be used to generate the map
start = 4000;
finish = 10000;

% Store the selected range of data in new variables
% MDOT = mass flow rate
% V = compressor displacement
% RPS = compressor speed in revolutions per second
% RPM = compressor speed in revolutions per minute
% TKRI = inlet temperature
% PKI = inlet pressure
% PKO = outlet pressure
% TIME = time values
MDOT = AllData.mdot(start:finish);
V = 3.0416e-5;
RPS = AllData.RPM(start:finish)/60;
RPM = AllData.RPM(start:finish);
TKRI = AllData.Tkri_im(start:finish);
PKI = AllData.Pki(start:finish);
PKO = AllData.Pko(start:finish);
TIME = AllData.Time(start:finish);

% Calculate the inlet fluid density
RHO_K = interp2(FluidProp.T,FluidProp.P,FluidProp.Rho_pt,TKRI,PKI);

% Calculate the volumetric efficiency
ETA_V = MDOT./(V.*RPS.*RHO_K);

% Form input matrix X, assuming a model structure
X = [ones(size(PKI)) RPM PKI PKO PKI.*RPM PKO.*RPM PKI.*PKO];

% Find model coefficients using left matrix division (approximate matrix
% inverse)
a = X\ETA_V;

% Find the volumetric efficiency values predicted by the model
ETA_V_model = X*a;

% Find the error (difference between data and model volumetric efficiency)
error = (ETA_V_model-ETA_V);

% Find the maximum error value, used to evaluate model structure
MaxErr = max(abs(error));

% Find the average error value, used to evaluate model structure
AveErr = mean(error);

% Find the RMS error, used to evaluate model structure
rms = norm(error)/sqrt(length(PKI))
```

```

% Plot the error as a function of time, used to evaluate model structure
plot(TIME,error)

% Clear the variables used for map generation
% Pi = inlet pressure
% Po = outlet pressure
% rpm = compressor speed
% eta_v_map = lookup table array
clear Pi
clear Po
clear rpm
clear eta_v_map

% Define input variable vectors
Po = 880:5:930;
Pi = 305:5:340;
rpm = 900:10:1100;

% Generate the lookup table using a for loop for each input, equation
% should match the model structure chosen for the X matrix
for c1 = 1:length(rpm)
    for c2 = 1:length(Pi)
        for c3 = 1:length(Po)
            eta_v_map(c1,c2,c3) = a(1) + a(2).*rpm(c1) + a(3)*Pi(c2)...
                + a(4).*Po(c3) + a(5).*Pi(c2)*rpm(c1)...
                + a(6).*Po(c3)*rpm(c1) + a(7).*Pi(c2)*Po(c3);
        end
    end
end

% Store the input vectors and lookup table array in a structure
CompProp.Pi = Pi;
CompProp.rpm = rpm;
CompProp.Po = Po;
CompProp.eta_v = eta_v_map;

```

H.8 Adiabatic Efficiency Performance Map

```

% This file creates a compressor adiabatic efficiency performance map
% with inputs of inlet pressure, outlet pressure, and compressor speed.
% The experimental system data is stored in the workspace in a structure
% called AllData.

% The start and finish variables are used to select the range of data
% that will be used to generate the map
start = 4000;
finish = 10000;

% Store the selected range of data in new variables
% RPS = compressor speed in revolutions per second
% RPM = compressor speed in revolutions per minute
% TKRI = inlet temperature
% TKRO = outlet temperature
% PKI = inlet pressure
% PKO = outlet pressure
% TIME = time values

```

```

RPS = AllData.RPM(start:finish)./60;
RPM = AllData.RPM(start:finish);
TKRI = AllData.Tkri_im(start:finish);
TKRO = AllData.Tkro_im(start:finish);
PKI = AllData.Pki(start:finish);
PKO = AllData.Pko(start:finish);
TIME = AllData.Time(start:finish);

% Calculate the inlet fluid enthalpy
HIN = interp2(FluidProp.T,FluidProp.P,FluidProp.H_pt,TKRI,PKI);

% Calculate the outlet fluid enthalpy
HOUT = interp2(FluidProp.T,FluidProp.P,FluidProp.H_pt,TKRO,PKO);

% Calculate the inlet fluid entropy
S = interp2(FluidProp.H,FluidProp.P,FluidProp.S_ph,HIN,PKI);

% Calculate the isentropic outlet fluid enthalpy
HOUTS = interp2(FluidProp.S,FluidProp.P,FluidProp.H_ps,S,PKO);

% Calculate the adiabatic efficiency
ETA_A = (HOUTS - HIN)./(HOUT-HIN);

% Form input matrix X, assuming a model structure
X = [ones(size(PKI)) PKI PKO RPM PKI.^2 PKO.^2 RPM.^2];

% Find model coefficients using left matrix division (approximate matrix
% inverse)
a = X\ETA_A;

% Find the volumetric efficiency values predicted by the model
ETA_A_model = X*a;

% Find the error (difference between data and model volumetric efficiency)
error = (ETA_A_model-ETA_A);

% Find the maximum error value, used to evaluate model structure
MaxErr = max(abs(error));

% Find the average error value, used to evaluate model structure
AveErr = mean(error);

% Find the RMS error, used to evaluate model structure
rms = norm(error)/sqrt(length(PKI))

% Plot the error as a function of time, used to evaluate model structure
plot(TIME,error)

% Clear the variables used for map generation
% Pi = inlet pressure
% Po = outlet pressure
% rpm = compressor speed
% eta_a_map = lookup table array
clear Pi
clear Po
clear rpm

```

```

clear eta_a_map

% Define input variable vectors
Po = 880:.5:930;
Pi = 305:.5:340;
rpm = 900:10:1100;

% Generate the lookup table using a for loop for each input, equation
% should match the model structure chosen for the X matrix
for c1 = 1:length(rpm)
    for c2 = 1:length(Pi)
        for c3 = 1:length(Po)
            eta_a_map(c1,c2,c3) = a(1) + a(2).*Pi(c2) + a(3).*Po(c3)...
                + a(4).*rpm(c1) + a(5).*Pi(c2).*Pi(c2)...
                + a(6).*Po(c3).*Po(c3) + a(7).*rpm(c1).*rpm(c1);
        end
    end
end

% Store the input vectors and lookup table array in a structure
CompProp.Pi = Pi;
CompProp.rpm = rpm;
CompProp.Po = Po;
CompProp.eta_a = eta_a_map;

```

Appendix B. Operating Conditions

Table B.1 Model validation scenario operating conditions

	Units	Validation Scenario			
		Single Steps	Single Steps with System ID	Drive Cycle	Humidity
Evaporator					
Pressure	[kPa]	270.4	273.128823	354	273.2356
Inlet Enthalpy	[kJ/kg]	105.92509	105.92509	102.48	104.1116
Outlet Refrigerant Temperature	[C]	18.25	18.25	17.1	15.7
Refrigerant Mass Flow Rate	[kg/s]	0.00713	0.00713	0.00594637	0.0065
Slip Ratio		4.6	4.6	4.2	4.39
Inlet Air Temperature	[C]	23.9819834	23.9819835	23.7227308	23.1194
Outlet Air Temperature	[C]	17.04	17.04	17.38	17.908
Air Mass Flow Rate	[kg/s]	0.15685995	0.15685995	0.15685995	0.1569
Two-phase HTC	[kW/m^2-K]	2	2	2	1
Superheat HTC	[kW/m^2-K]	0.04	0.04	0.04	0.3
Air-side HTC 1 (From Data)	[kW/m^2-K]	0.139622	0.141077	0.068438	0.0195
Air-side HTC 2 (From j factor)	[kW/m^2-K]	0.058341	NA	0.083905	NA
Inlet Relative Humidity	[%]	NA	NA	NA	0.4216
Outlet Relative Humidity	[%]	NA	NA	NA	0.515
Air Pressure	[kPa]	NA	NA	NA	101.325
Condenser with Receiver					
Pressure	[kPa]	970	970	925	NA
Inlet Refrigerant Temperature	[C]	59.65	59.65	49.5	NA
Refrigerant Mass Flow Rate	[kg/s]	0.00713	0.00713	0.00594637	NA
Slip Ratio		2.9	2.9	2.9	NA
Inlet Air Temperature	[C]	25.669659	25.669659	25.54463148	NA
Outlet Air Temperature	[C]	30.44	30.44	29.93	NA
Air Mass Flow Rate	[kg/s]	0.29382712	0.29382712	0.2529559	NA
Superheat HTC	[kW/m^2-K]	0.38791	0.38791	0.1	NA
Two-phase HTC	[kW/m^2-K]	1	1	2	NA
Air-side HTC 1 (From Data)	[kW/m^2-K]	0.086822	0.086822	0.112912	NA
Air-side HTC 2 (From j factor)	[kW/m^2-K]	0.12583	NA	0.071374	NA
Receiver Refrigerant Mass	[kg]	0.8	0.8	0.4	NA
Receiver Ambient Temperature	[C]	27	27	25	NA
Electronic Expansion Valve					
Inlet Pressure	[kPa]	975	975	925	NA
Outlet Pressure	[kPa]	296.5	296.5	365.77	NA
Inlet Temperature	[C]	37.13	37.13	35.77	NA
Refrigerant Mass Flow Rate	[kg/s]	0.00713	0.00713	0.00594637	NA
Input Signal	[%]	13	13	11.714527	NA
Compressor					
Inlet Pressure	[kPa]	263.5	263.5	347.24	273.2356
Outlet Pressure	[kPa]	975	975	914.93	944.1639
Inlet Temperature	[C]	21.91	21.91	21.44	20.45
Outlet Temperature	[C]	64.42	64.42	54.16	64.8
Refrigerant Mass Flow Rate	[kg/s]	0.00713	0.00713	0.00594637	0.0065
Compressor Speed	[RPM]	1600	1600	1000	1600